# ISOTOPE AND ELASTICITY STUDIES OF OXIDE SUPERCONDUCTORS AND OTHER LOW DIMENSIONAL SOLIDS



**Storrs Townsend Hoen**

Isotope and Elasticity Studies of Oxide Superconductors
and Other Low Dimensional Solids

By

Storrs Townsend Hoen

B.E. (Vanderbilt University) 1984
B.A. (Oxford University) 1986

DISSERTATION

Submitted in partial satisfaction of the requirements for the degree of

DOCTOR OF PHILOSOPHY

in

PHYSICS

in the

GRADUATE DIVISION

of the

UNIVERSITY OF CALIFORNIA at BERKELEY

Approved:

Chair: Alex Zaaat 11/22/92
Date
Marvin L. Cohen 8/18/92
Didier de Fontaine 11/18/92

* * * * * * * * * * * * * * * * * * * *

# Isotope and Elasticity Studies of Oxide Superconductors and Other Low Dimensional Solids

Storrs Townsend Hoen

Department of Physics
University of California, Berkeley

## Abstract

The superconducting condensate-lattice and charge density wave (CDW)-lattice interactions have been investigated using isotopic substitution, elasticity studies, and electrical transport.

In the oxide superconductor, $YBa_2Cu_3O_7$, an extremely small, but finite, transition temperature ($T_c$) shift was found with $^{18}O$ substitution. $\alpha = 0.019 \pm 0.004$ where $T_c \sim M^{-\alpha}$ and M is the isotopic mass. The small $\alpha$ indicates that superconductivity in $YBa_2Cu_3O_7$ cannot be explained within a standard three-dimensional phonon-mediated pairing model.

A variety of single crystal high-temperature superconductors (HTSC's) have been explored with vibrating reed techniques to investigate the possibility of a structural instability underlying the superconducting transition. For $YBa_2Cu_3O_7$, a small softening of the Young's modulus (Y) is detected at $T_c$. An associated slope anomaly in Y suggests a structural instability similar to that found for the A-15 materials. No softening at $T_c$

was detected for $Bi_2Sr_2CaCu_2O_8$ or Tl-Ba-Ca-Cu-O, and, though the Tl-Ba-Ca-Cu-O also showed a large slope anomaly, no such effects were seen for $Bi_2Sr_2CaCu_2O_8$. In addition, the elastic properties of Al-doped $YBa_2Cu_3O_7$ and oxygen deficient $Bi_2Sr_2CaCu_2O_{8-y}$ were also investigated.

In the CDW material, $NbSe_3$, elasticity studies indicate some carrier conversion in the lower CDW state with applied magnetic field (H). The data show no evidence for any additional H-induced phase transition. The sample length (L) of a second CDW material, $TaS_3$, demonstrates a remarkable dependence on applied bias field (E) and time. Bias field effects are orders of magnitude larger than that for comparably sized commercial piezo-electrics. These length changes are interpreted as being directly caused by changes in the CDW metastable state.

Elastic CDW models used to account for many CDW properties, such as those described above, fail to explain the broadband (BBN) associated with CDW conduction. The role of phase slip in producing BBN was studied by inducing macroscopic phase slip centers (PSC's) with applied temperature gradients. The thermally induced PSC's do not generate appreciable BBN. The data indicate some independence of the noise sources distributed in the sample; however, particular CDW metastable states may also generate substantial BBN.

For Gaga, my grandmother,
whose cheerfulness and indomitable spirit
are an inspiration to me.

# Table of Contents

# List of Figures

# List of Tables

# Acknowledgments

I am indebted to the expert guidance of my research advisor Alex Zettl. He fostered a scientific playfulness and a willingness to imagine many experimental paths and outcomes. Most importantly, he is an advisor whose respect for each graduate student is clear and who has a flexible vision of what constitutes a good scientist.

Marvin Cohen has been instrumental in offering a kind ear and thoughtful advice at branchings in my graduate career. His clear descriptions in my first solid state physics course were a fantastic introduction to the field. Peter Yu welcomed me into the department and guided my first investigations into possible research directions. John Clarke, Bill Bialek, and Dan Rokhsar have significantly influenced my image of the physicist and were consistently interested in my research. I am also grateful to Didier de Fontaine for his comments on oxygen deficient $YBa_2Cu_3O_{7-\delta}$ and for his careful reading of this thesis.

One of the strengths of the Berkeley Physics Department is certainly its staff. My time here has been greatly enhanced by the warmth of Anne Takizawa, Ken Miller, Donna Sakima, Dana Greenberg, and Toni Granger. Lynn Pelosi and Ivo Micheli have been marvelous buffers from the large university bureaucracy. Al Daft and Joseph Kant have patiently overseen my many forays into the machine shop. My nights in LeConte and Birge would have seemed much longer without the pleasant interruptions of Mike Howard, Nuan Khabanh, and Michael Prevost, the Jamaican man.

Many graduate students have guided me and made me proud to be a member of this community. The incredible members of the Zettl group

have created a laboratory environments which is friendly and exciting, with additions of levity and support. Lincoln Bourne guided my first tentative steps into vibrating reed and isotope effect measurements. Through two years of late night shifts at the LBL magnetometer, Bill Creager was an excellent companion and friend. Brian Burk made our office a welcoming place and somehow maintained his sanity through four years of questions and apparently aimless musings. Over a hectic two months of countless London Times crossword puzzles, Ian Parker taught me how to drain as much as possible from an experiment and when to move on. On the trail, in the lab, and everywhere in his life, he appreciates the art which surrounds us. Much of this thesis, and, in particular the metastable length state chapter, would have been impossible without the patience, cheerfulness, and intelligence of Xiao-Dong Xiang.

During my last year I had the pleasure to collaborate with Nasreen Chopra at whose laughter, intelligence, and eidetic memory I continue to marvel. Mike Crommie, with his gifts of fruit, literature, and his indomitable sense of fun, always enlivened the Zettl lab. Our resident computer deity, Bill Vareka, has been generous both in teaching software and in discussing English style. My graduation might have been stalled indefinitely without his timely healing of an ailing gas flow system. I am grateful that my graduate career intersected with that of Gabriel Briceno, with his children and his inventive means both inside and outside the lab. Phil Parilla and Mike Hundley apparently never fatigued of teaching me the intricacies of the lab, and I especially thank Phil for agreeing that it was indeed the beginning of an earthquake on an October day. On his visit from Japan, Hiroshi Bando brought a cheerfulness which helped me

realize the importance of the more mundane experimental tasks. I still don't understand how he was able to pack a complete physics lab into one suitcase. Several others who I have not worked with directly but have added considerably to the atmosphere of the lab are Mark Sherwin, Anita Barnes, and Jian-Guo Huo.

Two graduate students outside of the Zettl group deserve particular mention because their companionship greeted me when I first arrived in Berkeley and our friendships have grown during my stay. Fred Kral single-handedly dispelled any delusions I had of physicists being unwilling to explore areas outside of physics. Our weekly forays into stir-fry and late night San Francisco were great additions to that first year. Whether dancing until 3 AM, cooking dinner, road tripping, hiking, producing furry dice performances, or just warming my house, I am grateful for his friendship. Dave Miller was a fellow adventurer in the world of collegiate ultimate and an honorary housemate at each of my Berkeley residences. He has shown me ways of binding friends into a community.

Marc Bensadoun, Nathan Hunt, and Paul Selvin, three physicists who share my addiction for chess seasoned with conversation, were delightful additions to some of my Tuesday nights. Their ideas and thoughts have been incorporated in many areas of my life. I am also thankful to their partners who were considerate as some of our evenings drifted into mornings.

During my last year as a graduate student, I had the pleasure of being involved in a wonderful experiment, the Physics Graduate Student Topic Group. This diverse group met every two weeks to discuss issues affecting our lives and the scientific community at large. Discussions of

sexism, racism, and stereotypes of scientists intermingled with thoughts on our present research directions and memories of how science had touched us in the past. One of the joys of this group was the friendships it fostered. Ruth Ellen Thomson and Bruce Birkett were crucial in supporting my leadership as the group emerged. After the meeting, dinners with R.E. would find us developing topics in more depth. Bruce's insistent support and willingness to think deeply on all topics were a gift. Cynthia Hess continues to teach me new methods of leading and her strong presence allowed me to hazard some of the more difficult topics. Through the last half year, Nasreen Chopra and Karen Tang have been crucial in keeping my head looking forward and helping me through the harder places. Warren Holmes and Steve Weiss have both added insight and a careful attention to detail. These people, and the several others who have nurtured the topic group, make me tremendously proud to be a scientist.

My life in Berkeley has been touched by many people outside of physics. My friendship with Kathy Kaufman has spanned two shared homes. We would marvel at the strange sociology of Californians, a sociology of which I am now part. With Lisa Brill, I shared adventures, friends, theater, and dance. Helen Karamallakis has made the distance between England and California seem insignificant and during my toughest times would somehow find a way to appear. Eve Weiss and Ruth Hufbauer transformed 3125 Lewiston from a cold house into a warm home.

Throughout my graduate career, my family has been incredibly supportive. They have been a solid foundation for all I have done. I have

yet to meet a set of men that I enjoy as much as my brothers. Our laughter is a remarkable remedy to apparently serious times. I particularly thank Weber for deciding to move to my region and helping me through all the transitions of this last year. My Mom and Dennis have been inspirations to me and have helped me understand the importance of following my visions. My Dad and Maxie have been avid supporters of all aspects of my life and their understanding of who I am has made a huge difference to me.

Four years ago, on a blustery Halloween, I had the opportunity to take a walk through the Castro Street Fair with Beth Grossman. Since the awakening of my love for her on that night, I have seen our feelings grow through laughter, exploring new places, and learning about each other's strengths and weaknesses. She has been an incredible ally in all my graduate work.

I am also grateful for the generous support of the Fannie and John Hertz Foundation. This research was also supported in part by NSF Grants No. DMR 84-00041 and DMR 83-51678, and by the Director, Office of Energy Research, Office of Basic Energy Science, Materials Sciences Division of the U.S. Department of Energy under Contract No. DE-AC03-76SF00098.

## Vita

| | |
|---|---|
| January 21, 1962 | Born in Baltimore, Maryland |
| May, 1984 | B. E. in Electrical Engineering, Materials Science, Physics, and Mathematics, Vanderbilt University |
| July, 1986 | B. A. in Physics and Philosophy, Keble College, Oxford University |
| September, 1986 to June, 1992 | Research Assistant, Department of Physics, University of California at Berkeley |

## Publications


1. Tanya A. Faltens, William K. Ham, Steven W. Keller, Kevin J. Leary, James N. Michaels, Angelika M. Stacy, Hans-Conrad zur Loye, Donald E. Morris, T.W. Barbee III, L.C. Bourne, Marvin L. Cohen, S. Hoen, and A. Zettl, "Observation of an oxygen isotope shift in the superconducting transition temperature of $L_{1.85}Sr_{0.15}CuO_4$," Phys. Rev. Lett. **59** 915 (1987).

2. L.C. Bourne, S. Hoen, M.F. Crommie, W.N. Creager, A. Zettl, Marvin L. Cohen, Luis Bernardez, John Kinney, and Donald E. Morris, "Magnetic and resistive determination of the oxygen isotope effect in $La_{1.85}Sr_{0.15}CuO_4$," Solid State Comm. **67**, 707 (1988).

3. A. Zettl, L.C. Bourne, W.N. Creager, M.F. Crommie, and S. Hoen, "Electron-phonon interactions in High-temperature oxide superconductors: isotope effects and elasticity studies," Syn. Met. **29**, F273 (1988).

4. S. Hoen, L.C. Bourne, Choon M. Kim, and A. Zettl, "Elastic response of polycrystalline and single-crystal $YBa_2Cu_3O_7$," Phys. Rev. **B38** 11949 (1988).

5. S. Hoen, W.N. Creager, L.C. Bourne, M.F. Crommie, T.W. Barbee III, Marvin L. Cohen, A. Zettl, Luis Bernardez, and John Kinney, "Oxygen isotope study of $YBa_2Cu_3O_7$," Phys. Rev. **B39**, 2269 (1989).

6. M.F. Crommie, Amy Y. Liu, A. Zettl, Marvin L. Cohen, P. Parilla, M.F. Hundley, W.N. Creager, S.Hoen, and M.S. Sherwin, "c-axis stress dependence of normal and superconducting state properties of $YBa_2Cu_3O_7$," Phys. Rev. **B39**, 4231 (1989).

7. A. Zettl, A. Behrooz, G. Briceño, W. N. Creager, M. F. Crommie, S. Hoen, and P. Pinsukanjana, "Anisotropic Transport in Y-Ba-Cu-O and Bi-Sr-Ca-Cu-O," in *Mechanisms of High Temperature Superconductivity*, edited by H. Kamimura and A. Oshiyama (Springer-Verlag, New York, 1989), p. 249.

8. X.D. Xiang, M. Chung, J.W. Brill, S. Hoen, P. Pinsukanjana, and A. Zettl, "Elastic properties of $Bi_2Sr_2CaCu_2O_8$," Solid. State. Comm. **69**, 833 (1989).

9. S. Hoen, I.D. Parker, W.N. Creager, and A. Zettl, "Magneto-elastic properties of $NbSe_3$," Proceedings of the International Conference on Synthetic Metals, Tübingen (1990).

10. S. Hoen and A. Zettl, "Is Charge Density Wave Broadband Noise due to Phase Slip?" (to be published).

11. S. Hoen, B. Burk, A. Zettl and M. Inui, "Metastable Length States of a Random System: $TaS_3$," Phys. Rev. **B46**, 1874 (1992).

12. S. Hoen, N. G. Chopra, X.-D. Xiang, R. Mostovoy, Jianguo Hou, W. A. Vareka, and A. Zettl, "Elastic Properties of a van der Waals Solid: $C_{60}$," submitted to Physical Review **B**.

# Chapter 1: Introduction

Low-dimensional electronic systems are presently the center of tremendous experimental and theoretical research. With the discovery of charge-density wave (CDW) materials[1, 2] and high-temperature superconductors (HTSC's),[3-6] as well as the advent of clean quantum confined systems, new highly-correlated electronic states can now be investigated. In each of these systems, a high temperature state exists in which the charge carriers are well described by a nearly free electron model. Below a particular transition temperature ($T_c$), the electrons condense and the system evinces startingly different properties.

In CDW materials, charge carriers on either side of the Fermi surface hybridize, producing a spatial modulation of the carrier density concomitant with a modulation of the underlying lattice. For this phase transition to occur, there is a trade-off between the energy lost by the conduction electrons and the energy gained by the distorted lattice. The reduced dimensionality ensures that there are nearly planar sections of the Fermi surface and that many electronic states have their energies reduced by the modulation. For most models of the HTSC's, the conduction edge charge carriers also hybridize for temperatures, $T < T_c$. The resulting condensate is well described by paired conduction edge states. While theorists have suggested many possible pairing mechanisms, the proper description has yet to be determined. Indeed, the role that reduced dimensionality, arising from the 2-dimensional Cu-O planes endemic to all HTSC's, plays in pairing the electrons is still poorly understood.

For both HTSC's and CDW materials, the properties of the electronic condensate and underlying lattice are intimately linked and the lattice provides an excellent tool to determine the characteristics of the condensate. Altering the lattice, by applying strains,[7] introducing interstitials,[8] or exchanging one isotope for another,[9] directly affects the condensate as evidenced by changes in its transition temperature, conducting properties, and magnetic characteristics. Conversely, the formation of the CDW[10] or superconducting state[11] affects the interionic potentials and elastic properties of the underlying lattice.

This thesis describes a diverse set of experiments which probe the CDW and superconducting condensates using the static and dynamic properties of the lattice. These experiments fall into two general categories: isotope effects in HTSC's and elastic properties of both HTSC's and CDW materials.

The effect that changes in the isotopic mass have on $T_c$ has had tremendous importance in demonstrating phonon-mediated pairing in the conventional superconductors. Chapter 2 provides an overview of the isotope effect in conventional superconductors and HTSC's. Several experiments on the HTSC $YBa_2Cu_3O_7$ (YBCO) have yielded disparate results; the variation between their measured isotope shifts hampers the discrimination between the various proposed pairing mechanisms in these compounds. Chapter 3 describes our experiment which resolves some of the previous ambiquities and yields the most accurate determination to date of the isotope effect in YBCO. The small measured shift demonstrates that superconductivity in YBCO cannot be explained within a standard 3-dimensional phonon-mediated pairing model.

Elastic measurements further probe the interplay between the superconducting state and the underlying lattice. For the A-15 compounds, elastic measurements have been essential in demonstrating the importance of structural instability for superconductivity.[12] Chapter 4 summarizes the variety of experimental techniques used to study the HTSC's and CDW materials. A vibrating reed apparatus designed to give the best compromise between sensitivity and experimental ease is particularly considered. Chapter 5 describes an investigation of the elastic properties of $YBa_2Cu_3O_7$, $Bi_2Sr_2CaCu_2O_8$, and Tl-Ba-Sr-Cu-O. Using an extremely sensitive vibrating reed apparatus, we confirm the second order nature of the superconducting phase transition in YBCO. The lattice softening, predicted to occur at $T_c$, is resolved for the first time. There is some evidence for incipient structural phase transitions in the Young's modulus of these materials.

The remaining three chapters describe measurements on the elastic and electrical properties of CDW materials. Chapter 6 details an investigation of the effect of magnetic fields on the elastic properties of the CDW material $NbSe_3$. Magnetoresistance studies have indicated substantial magnetic conversion of conduction electrons into the CDW state and the possibility of an additional phase transition.[13] The Young's modulus anomalies associated with the upper ($T_{c1}$ = 144K) and lower ($T_{c2}$ = 59K) CDW transitions are clearly evident. The critical exponents at these transitions are not adequately described by existing theories of CDW elasticity. While the Young's modulus is extremely sensitive to applied magnetic field, it evinces no evidence for carrier conversion or additional phase transitions.

Chapter 7 describes a more direct measurement of the elastic properties of the CDW condensate. The sample lengths of $TaS_3$ crystals demonstrate a remarkable dependence on applied bias field and time. The bias field effect is orders of magnitude larger than that for comparably sized commercial piezo-electrics. These length changes are interpreted as being directly caused by changes in the CDW metastable state. A simple model describes many qualitative features of the experiment; however, changes in existing theories of CDW elasticity are required to explain the large magnitude of the effect.

The elastic nature of the CDW condensate affects not only the sample Young's modulus but also the electrical conduction properties. The existence of a finite depinning field is immediate evidence that the CDW can be stretched and deformed. The sliding CDW, because of its deformability, produces both sharply peaked high frequency noise (narrow band noise or NBN) and broader, 1/f-like, low frequency noise (broadband noise or BBN). Numeric and analytic simulations have demonstrated that NBN should exist for any elastic system with many degrees of freedom. However, the cause of BBN remains an open question. One model suggests the BBN arises from microscopic 'tears' or phase slip centers in the CDW condensate.[14] Chapter 8 describes an experimental test of this hypothesis in which a temperature gradient is placed across $NbSe_3$ crystals, inducing the formation of phase slip centers. These macroscopic phase slip centers appear soft in that they convert phase without generating appreciable BBN.

## References


1. G. Grüner and A. Zettl, Phys. Rep. **119**, 117 (1985) and references therein.

2. L. Gor'kov and G. Grüner. *Charge Density Waves in Solids* (North Holland, Amsterdam, 1989) and references therein.

3. J. G. Bednorz and K. A. Müller, Z. Phys. B **64**, 189 (1986).

4. M. K. Wu, J. R. Ashburn, C. J. Torng, P. H. Hor, R. L. Meng, L. Gao, Z. J. Huang, Y. Q. Wang and C. W. Chu, Phys. Rev. Lett. **58**, 908 (1987).

5. H. Maeda, Y. Tanaka, M. Fukuton and T. Asano, Appl. Phys. Lett. **27**, L209 (1988).

6. Z. Z. Sheng and A. M. Hermann, Nature **332**, 55 (1988).

7. J. E. Schirber, D. S. Ginley, E. L. Venturini and B. Morosin, Phys. Rev. **B35**, 8709 (1987).

8. X.-D. Xiang, S. Mckernan, W. A. Vareka, A. Zettl, J. L. Corkill, T. W. Barbee III and Marvin L. Cohen, Nature **348**, 145 (1990).

9. S. Hoen, W. N. Creager, L. C. Bourne, M. F. Crommie, T. W. Barbee III, Marvin L. Cohen, A. Zettl, Luis Bernardez and John Kinney, Phys. Rev. **B39**, 2269 (1989).

10. S. Hoen, I. D. Parker, W. N. Creager and A. Zettl, Synth. Met. **41-43**, 3863 (1991).

11. S. Hoen, L. C. Bourne, Choon M. Kim and A. Zettl, Phys. Rev. **B38**, 11 (1988).

12. L. R. Testardi, in *Physical Acoustics*, W. P. Mason and R. N. Thurston ed., (Academic, New York, 1973), p. 193.

13. I. D. Parker, W. N. Creager, A. Chen, P. Y. Yu and A. Zettl, Synth. Met. **41-43**, 3859 (1991).

14. S. N. Coppersmith, Phys. Rev. Lett. **65**, 1044 (1990).

# Chapter 2: Overview of the Isotope Effect

## 2.1 Introduction

The spectacularly high transition temperatures of the newly discovered classes of oxide superconductors[1-4] have resulted in suggestions that the superconductivity in these materials may be fundamentally very different from that of "conventional" superconductors. The Bardeen-Cooper-Schrieffer (BCS)[5] theory of phonon-mediated electron pairing may not be adequate to explain superconductivity within these new materials. Shapiro step experiments[6] on $La_{1.85}Sr_{0.15}CuO_4$ and $YBa_2Cu_3O_7$ (YBCO), which exploit intrinsic ac Josephson effects within polycrystalline specimens, have clearly indicated that a fundamental charge q=2e is associated with the superconducting state. Although most researchers believe that this result demonstrates that electron pairing does occur, the specific pairing mechanism (phonon or non-phonon) is generally considered to be an open question. The remainder of this chapter is organized as follows: Sect. 2.2 reviews the basic theory of the isotope effect in conventional superconductors. Sects. 2.3 and 2.4 give the historical background of isotope effect measurements in YBCO and other high-temperature superconductors (HTSC's), respectively. Sect. 2.5 summarizes what requirements must be met to accurately determine the isotope effect.

## 2.2 Isotope effect in conventional superconductors

The dependence of the superconducting transition temperature $T_c$ on isotopic mass M in the host lattice has been one of the most revealing tests for phonon-mediated pairing. The original isotope effect experiments[7] in

elemental mercury showed that $T_c \sim M^{-\alpha}$, with $\alpha=0.5$. This discovery provided one of the important clues which resulted in the BCS theory of superconductivity. According to the simple BCS model,

$$T_c = 1.13\, \hbar\omega_D \exp(-1 / \lambda) \tag{2.1}$$

where $\omega_D$ is the Debye frequency and $\lambda$ is the electron-phonon coupling constant. In a harmonic solid $\lambda$ does not depend on M, but $\omega_D \sim M^{-1/2}$ which implies $T_c \sim M^{-1/2}$. When Coulomb repulsion is included with the attractive electron-phonon interaction in a two-square well model,[8, 9]

$$T_c = 1.13\, \hbar\omega_D \exp(-1 / (\lambda - \mu^*)) \tag{2.2}$$

and $$\alpha = (1/2)(1 - (\mu^* / (\lambda - \mu^*))^2) \tag{2.3}$$

where $\mu^*$ is the renormalized Coulomb repulsion. The analytic expressions reflect the assumption that $\lambda < 1$, the weak-coupling limit. From (2.3), $\alpha$ may be reduced from 0.5 and assume negative values. In the strong-coupling limit ($\lambda \geq 1$) of BCS isotropic phonon-mediated pairing, the simple analytic expression (2.2) for $T_c$ is no longer accurate and $T_c$ must be calculated from an integral equation. Even in this case, however, $\alpha$ can be no greater than +1/2.

Indeed, isotope studies in conventional superconductors find $\alpha$ ranging from 0.5 (mercury) to -2.2 ($\alpha$-uranium).[10] Interestingly, for zirconium and ruthenium, $\alpha = 0$, which can be shown to be consistent with phonon-mediated electron pairing if one assumes a two square well model and takes into account specific normal state and superconducting properties of the individual materials. For the strong coupled elemental superconductors (Hg, Pb), $\alpha$ is found to approach 0.5.

**2.3 Previous isotope effect measurements in $YBa_2Cu_3O_7$**

The first isotope studies on high-$T_c$ oxide superconductors were oxygen isotope substitution experiments performed on the $YBa_2Cu_3O_7$ structure. Batlogg *et al.*[11] substituted $^{18}O$ isotopes in $YBa_2Cu_3O_7$ and in $EuBa_2Cu_3O_7$ by heating samples to 550° C in vacuum, removing approximately 10% of the oxygen, and heating again in an $^{18}O_2$ atmosphere. After 3 cycles, 74%±7% of the $^{16}O$ had been substituted with $^{18}O$, as determined by Rutherford backscattering spectroscopy. They observed resistive shifts of -0.3K to -0.4K in $T_c$, but observed no shifts in the magnetization data and therefore set a limit on the isotope shift of $\alpha$=0.0±.02. A Raman line at 500 $cm^{-1}$ that was assigned[12] to the O(1) site which bridges the inequivalent Cu atoms gave isotope shifts of about 4% demonstrating that at least some of the phonon modes were isotope shifted. Bourne *et al.*[13] substituted $^{18}O$ for $^{16}O$ in $YBa_2Cu_3O_7$ by heating a sample at 950°C in an $^{18}O$ atmosphere. An identical heat treatment was performed in $^{16}O$ on another sample derived from the same parent pellet. The oxygen isotope content was measured with temperature-programmed-desorption and with 50% (random) removal of the total oxygen content, 90% of the desorbed oxygen was found to be $^{18}O$. Within an experimental uncertainty of ±0.3K, no isotope effect was observed in both magnetization and resistivity measurements, yielding $\alpha = 0.0 \pm 0.027$.

Leary *et al.*[14] reported a finite oxygen isotope shift in $YBa_2Cu_3O_7$. Using a gas exchange technique similar to that of Bourne *et al.*, they obtained $^{18}O$ enrichments of 73% to 90% (determined by thermally programmed desorption), and identified shifts in $T_c$ of -0.3K to -0.5K from

magnetization data. The shifts in $T_c$ were reversed in one sample and partially reversed in a second sample by re-substituting $^{16}O$ for the $^{18}O$. The same group later reported magnetization data[15] suggestive of $^{18}O$ isotope shifts of -0.5K to -0.9K for 67% $^{18}O$ enrichment, yielding $\alpha$=0.07 to 0.12. The isotope shifts determined by this group lie outside the original error limits set by Batlogg *et al.*[11] and Bourne *et al.*[13]

Morris *et al.*[16] attempted to reduce the error limits of the oxygen isotope effect in $YBa_2Cu_3O_7$. Since an applied magnetic field was found to substantially increase the measured transition width, they used applied field values of only 3 Oe during the magnetization measurement. A high temperature gas exchange technique was again used to substitute $^{18}O$ for $^{16}O$. After measuring the $T_c$'s, the isotope species of the two samples were reversed with another high temperature gas exchange treatment and the $T_c$'s were again determined. With $^{18}O$ isotope enrichments of approximately 88% (estimated from sample weight changes), $\alpha$ was found to be 0.019±.005. The error limits were estimated from variations in $\Delta T_c$ at different points in the susceptibility vs. temperature curves and from variations between the two annealing runs.

Lopdrup *et al.*[17] also performed gas phase oxygen isotope exchange studies on $YBa_2Cu_3O_7$. Samples containing up to 95% $^{18}O$ enrichment (determined by thermally programmed desorption measurements) were initially reported[17] to have $T_c$'s as much as 1K lower than the corresponding $^{16}O$ samples, but subsequent work[18, 19] revised these shifts to about -0.2K, again giving $\alpha$=0.02. One sample prepared with 98% enriched $^{18}O_2$ gas was found to have 97% $^{18}O$ enrichment.

Reports have also emerged of extremely large oxygen isotope shifts in $YBa_2Cu_3O_7$. Ott *et al.*[20] prepared oxygen isotope enriched $YBa_2Cu_3O_7$ samples by dissolving Y, Cu, and $BaC^{16}O_3$ in $^{18}O$ or $^{17}O$ enriched $HNO_3$. The resistive midpoint transition temperatures were 93K for the $^{16}O$ samples, 77K for samples with $^{17}O$, and 59K for samples with 95% $^{18}O$. The sample quality decreased dramatically with decreasing $T_c$'s, with magnetic susceptibility measurements showing transition widths of 40K or more for the lower $T_c$'s. A brief heat treatment in $^{16}O$ increased $T_c$ from 59K to 77K for an $^{18}O$ sample and from 77K to 90K for an $^{17}O$ sample. The large $T_c$ shifts reported by Ott *et al.* correspond to $\alpha \approx 3.5$, and it was suggested that the large shifts in $T_c$ arose because this process did not rely on gas exchange to populate the various oxygen sites.

Garcia *et al.*,[21] in an experiment which also circumvented some of the concerns with gas exchange, prepared oxygen enriched $YBa_2Cu_3O_7$ by first burning Y, Ba, and Cu in an $^{18}O$ atmosphere. The enriched oxides were then combined and sintered in an $^{18}O$ atmosphere. The magnetic transitions were reasonably sharp (~10K) and showed no isotope shift to ± 0.2K.

Morris *et al.* have performed site selective oxygen substitution on the plane sites and find an isotope shift $\Delta T_c \sim +0.3K$ with $O^{18}$ substitution.[22] They suggest this result indicates that the apical site is particular important in electron pairing. Crespi and Cohen[23] have advanced an alternative explanation.

In $YBa_2Cu_3O_7$, isotope experiments have also been performed on the other atomic sites. In general these experiments are less easily controlled since it is not possible to reversibly exchange isotopes on the Y, Ba, or Cu

sites for a given sample. A new sample must be prepared for each isotopic species. Bourne *et al.*[24] prepared $YBa_2Cu_3O_7$ with different Ba and Cu isotopes through a solid-state reaction process using $Y_2O_3$, $BaCO_3$, and CuO. $HNO_3$ was used to dissolve and mix the precalcined powder to yield sharp transitions. CuO with 99.6% $^{65}Cu$ and CuO with 99.7% $^{63}Cu$ were used for one pair of samples; $BaCO_3$ with 78.8% $^{135}Ba$ and $BaCO_3$ with 99.7% $^{138}Ba$ were used for another pair of samples. Through resistivity measurements the isotope shift was determined to be less than 0.2K for Cu ($\alpha = 0.0 \pm .07$) and less than 0.1K for Ba ($\alpha = 0.0 \pm .1$). Quan *et al.*[25] placed similar bounds on the isotope shift for Cu ($\Delta T_c = 0.0 \pm 0.2K$) using both a.c. susceptibility and resistivity to characterize the transition. Hidaka *et al.*[26] studied the effects of $^{134}Ba$ (85% pure) substitution for naturally occurring Ba (70% $^{138}Ba$). With an inductive technique, they determined that there was no isotope shift within 0.15K.

Although no experiments have been reported for different Y isotopes in $YBa_2Cu_3O_7$, the Y site has been substituted by a host of other rare earth elements with very different masses.[27] Some $T_c$ dependence on rare earth species is observed, but there is no correlation between $T_c$ and the ion mass. Hence no obvious isotope effect is observed.

### 2.4 Isotope effect in other high-$T_c$ superconductors

Oxygen isotope studies have also been performed on several high-$T_c$ oxides distinct from the $YBa_2Cu_3O_7$ structure. For $La_{1.85}Sr_{0.15}CuO_4$, Cohen *et al.*,[28] Batlogg *et al.*,[29] Faltens *et al.*,[30] zur Loye *et al.*,[15] and Bourne *et al.*[31] have reported significant shifts for 70%-80% $^{18}O$ enrichment corresponding to $\alpha$ between 0.1 and 0.2. For $La_{1.85}Sr_{0.15}CuO_4$, zur Loye *et*

*al.* report shifts of -1.3K to -1.6K with 75% $^{18}O$ enrichment, yielding $\alpha$=0.73 to 0.90; the same group has reported oxygen isotope shifts corresponding to similar large values of $\alpha$ for $BaPb_{0.75}Bi_{0.25}O_3$. Values of $\alpha$ greater than 0.5 have never before been observed for any superconductor, and such values are inexplicable within conventional BCS theory, regardless of the value of $T_c$. Batlogg *et al.*,[32] on the other hand, report $\alpha$=0.22±.03 for oxygen isotope substitution in $BaPb_{0.75}Bi_{0.25}O_3$.

In the related material, $Ba_{0.625}K_{0.375}BiO_3$ with a $T_c$ of 30K and cubic crystal structure, oxygen isotope experiments have found significant shifts in $T_c$. Hinks *et al.*[33] found reversible shifts of ~1.4K with an oxygen exchange of 96% yielding $\alpha$ = 0.41. Batlogg *et al.*,[34] however, found shifts of only ~0.3K for 65% substitution and calculated an $\alpha$ ~ 0.2. Both of these shifts can be explained within a phonon-mediated BCS model.

Recent studies of oxygen isotope substitution in Bi-Sr-Ca-Cu-O indicate $\alpha$=0.026 and 0.048 for the $T_c$=110K and $T_c$=85K phases, respectively.[35] Oxygen isotope substitution in Tl-Ba-Ca-Cu-O is especially difficult because the thallium readily leaves the compound at the same temperatures that the oxygen diffusion coefficients are low enough to provide good isotopic enrichment. One study[36] found no isotope shift in the 2223 phase ($T_c$ ~ 120K) to ± 0.9K.

It seems reasonable that the underlying pairing mechanism may be similar for each of the layered cuprates. Using a three-square well model which includes Coulomb repulsion, phonon-mediated attraction, and an additional pairing mechanism, Cohen *et al.*[37] predict that $\alpha$ may simply related to $T_c$ independent of material. Indeed, a plot of $\alpha$ vs $T_c$ for a variety of HTSC's, as shown in Fig. 2-1, roughly supports a scaling relation.

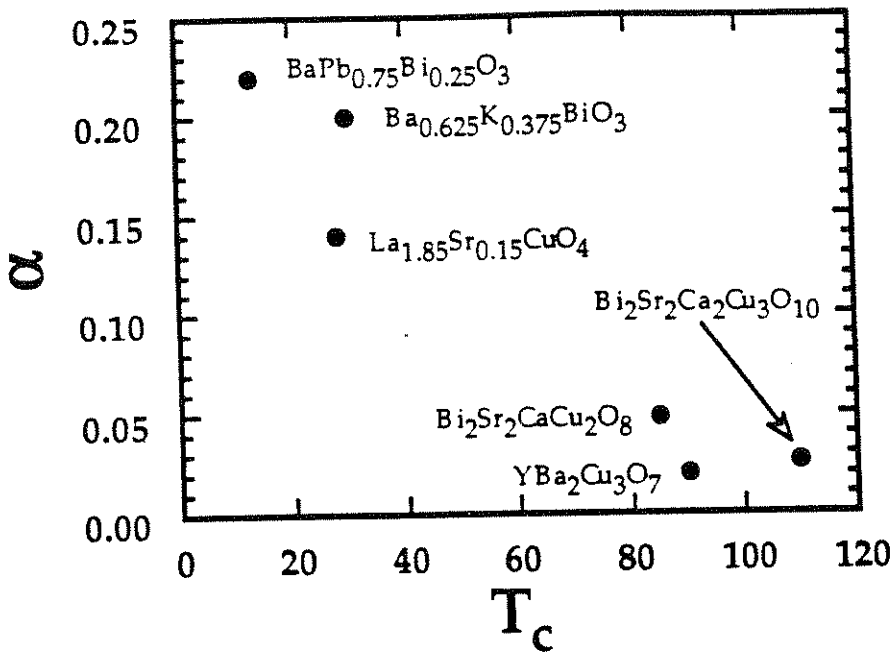


Fig. 2-1. Isotope effect exponent, $\alpha$, versus $T_c$ for several oxide superconductors. The values of $\alpha$ are based on oxygen substitution by the following groups: $BaPb_{0.75}Bi_{0.25}O_3$ ↔ Batlogg *et al.* (Ref. 32), $Ba_{0.625}K_{0.375}BiO_3$ ↔ Batlogg *et al.* (Ref. 34), $La_{1.85}Sr_{0.15}CuO_4$ ↔ Faltens *et al.* (Ref. 30), $Bi_2Sr_2CaCu_2O_8$ and $Bi_2Sr_2Ca_2Cu_3O_{10}$ ↔ Katayama-Yoshida *et al.* (Ref. 35), and $YBa_2Cu_3O_7$ ↔ Hoen *et al.* (Ref. 48).

This question of the relationship between $\alpha$ and $T_c$ can also be addressed with particular compounds. In the YBCO system, $T_c$ can be varied by adjusting the oxygen content or by substituting Pr for Y. Unfortunately, though there have been significant improvements,[38] it remains difficult to form materials with reproducible oxygen deficiencies. Moreover, $T_c$ is dependent not only on the oxygen content but also on the ordering of the oxygen vacancies in the chain sites.[38, 39] Isotope effect exchanges which may produce only subtle changes in $T_c$ are not at present feasible. In the (Y,Pr)$Ba_2Cu_3O_7$ compounds, Franck *et al.*[40] have detected a significant increase in $\alpha$ when $T_c$ is depressed as depicted in Fig. 2-2a. In the $La_{2-x}Sr_xCuO_4$ compounds $T_c$ varies with x reaching a maximum of 28K at x = 0.15. Initial results of Crawford *et al.*[41] show a large peak — with $\alpha$ exceeding 0.5 — in $\alpha$ vs $T_c$ at x = 0.125 shown in Fig. 2-2b. This experiment requires extremely careful sample preparation since, in this same region of x, $T_c$ depends sensitively of Sr content and the superconducting transitions become broader. The anomaly is suggestive of anharmonic phonon modes or incipient phase transition. Indeed, a low temperature (~60K) structural phase transition has been detected in the related compound La-Ba-Cu-O.[42] A number of theories based on lattice anharmonicity[43-45] or sharp singularities in the electronic density of states[46] have been advanced to explain the peculiar dependence of $\alpha$ on $T_c$. A more recent experiment by Ronay *et al.*[47] demonstrates the possibility that substitution of $^{18}O$ enhances growth of $La_{1.67}Sr_{0.33}Cu_2O_5$, a non-superconducting compound, at the expense of $La_{2-x}Sr_xCuO_4$. The growth of this additional compound reduces x in the superconducting compound and the measured isotope

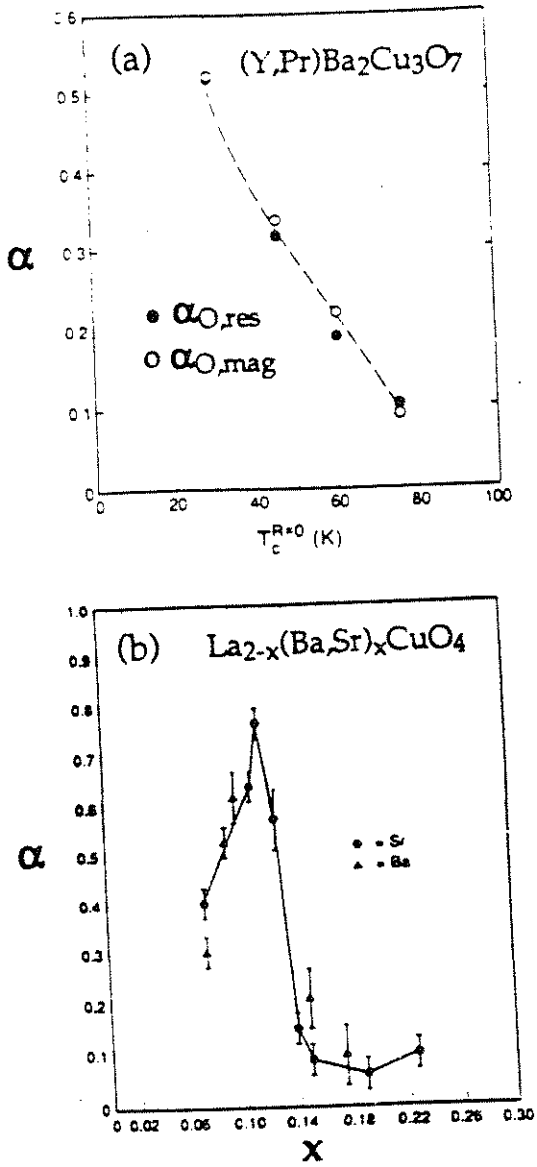


Fig. 2-2. (a) The oxygen isotope effect exponent, $\alpha$, versus $T_c^{R=0}$, the temperature at which the resistance of $(Y,Pr)Ba_2Cu_3O_7$ falls to zero. $\alpha$ is defined as $T_c \sim M^{-\alpha}$, where M is the average oxygen mass. The dotted line is only a guide to the eye. The change in $T_c$ is caused by substitution of Pr for Y. From J. P. Franck *et al.* (Ref. 40). (b) Oxygen isotope effect exponent, $\alpha$, versus x for $La_{2-x}Sr_xCuO_4$ and $La_{2-x}Ba_xCuO_4$. From Crawford *et al.* (Ref. 41).

shift reflects the effects both of reducing x and of exchanging $^{18}O$ for $^{16}O$. They suggest that this additional effect is the cause of the previous anomalously large shifts.

**2.5 Requirements for an accurate isotope effect measurement**

Thus, despite much work, the determination of more precise estimates of the magnitude of the isotope effect in most high-$T_c$ oxide superconductors is still an important area of research. Part of the difficulty in achieving this goal is in producing sufficiently well-characterized samples with sharp and reproducible transitions. Some ambiguity may even arise from data interpretation. For example, in deducing the finite oxygen isotope shift of -0.5K in $YBa_2Cu_3O_7$, Leary *et al.*[14] compare magnetization curves which differ by the quoted amount near the transition onset, but cross near the transition midpoint (suggestive of a zero isotope effect with large error bars).

Reliable determination of $\alpha$ with small error limits necessitates careful control of sample preparation, measurement, and data interpretation. In the study described in Chapter 3, we have attempted to lower the error limits for each of these contributions.

## References


1. J. G. Bednorz and K. A. Müller, Z. Phys. B **64**, 189 (1986).

2. M. K. Wu, J. R. Ashburn, C. J. Torng, P. H. Hor, R. L. Meng, L. Gao, Z. J. Huang, Y. Q. Wang and C. W. Chu, Phys. Rev. Lett. **58**, 908 (1987).

3. H. Maeda, Y. Tanaka, M. Fukuton and T. Asano, Appl. Phys. Lett. **27**, L209 (1988).

4. Z. Z. Sheng and A. M. Hermann, Nature **332**, 55 (1988).

5. J. Bardeen, L. N. Cooper and J. R. Schrieffer, Phys. Rev. **106**, 162 (1957); **108**, 1157 (1957); .

6. D. Estève, J. M. Martinis, C. Urbina, M. H. Devoret, G. Collin, P. Monod and A. Revcolevschi, Europhys. Lett. **3**, 1237 (1987).

7. E. Maxwell, Phys. Rev. **78**, 477 (1950); C. A. Reynolds, B. Serin, W. H. Wright and L. B. Nesbitt, Phys. Rev. **78**, 487 (1950); .

8. N. N. Bogoliubov, V. V. Tolmachev and D. V. Shirkov, *A New Method in the Theory of Superconductivity* (Consultants Bureau, Inc, New York, 1959).

9. J. C. Swihart, Phys. Rev. **116**, 45 (1959).

10. R. Meservey and B. B. Schwartz, in *Superconductivity*, R. D. Parks ed., (Marcel Dekker, New York, 1969), p. 126.

11. B. Batlogg, R. J. Cava, A. Jayaraman, R. B. van Dover, G. A. Koruouklis, S. Sunshine, D. W. Murphy, L. W. Rupp, H. S. Chen, A. White, K. T. Short, A. M. Mujsce and E. A. Rietman, Phys. Rev. Lett. **58**, 2333 (1987); **60**, 754 (1988); .

12. G. A. Kourouklis, A. Jayaraman, B. Batlogg, R. J. Cava, D. M. Stavola, D. M. Krol, E. A. Rietman and L. F. Schneemeyer, Phys. Rev. **B36**, 8320 (1987).

13. L. C. Bourne, M. F. Crommie, A. Zettl, Hans-Conrad zur Loye, S. W. Keller, K. L. Leary, Angelica M. Stacy and Don Morris, Phys. Rev. Lett. **58**, 2337 (1987).

14. Kevin J. Leary, Hans-Conrad zur Loye, Steven W. Keller, Tanya A. Faltens, William K. Ham, James N. Michaels and Angelica M. Stacy, Phys. Rev. Lett. **59**, 1236 (1987).

15. Hans-Conrad zur Loye, Kevin J. Leary, Steven W. Keller, William K. Ham, Tanya A. Faltens, James N. Michaels and Angelica M. Stacy, Science **238**, 1558 (1987).

16. Donald E. Morris, Randy M. Kuroda, Andrea G. Markelz, Janice H. Nickel and John Y. T. Wei, Phys. Rev. **B37**, 5936 (1988).

17. E. Lopdrup, M. Crawford, W. E. Farneth, R. K. Bordia, E. M. McCarron and S.J. Poon, Bull. Am. Phys. Soc. **33**, 558 (1988).

18. E. L. Benitez, J. J. Lin, S. J. Poon, W. E. Farneth, M. K. Crawford and E. M. McCaron, Phys. Rev. **B38**, 5025 (1988).

19. E. Lopdrup, (private communication).

20. Kevin C. Ott, Robert M. Aikin, Luis Bernardez, Allison Connor, Michael J. Fluss, Eduardo Garcia, Max Goldblatt, William B. Hutchinson, George H. Dwei, Carl J. Maggiore, Joe A. Martin, Robert Meisenheimer, Michael Nastasi, Eric J. Peterson, Eugene J. Peterson, Joseph R. Tesmer, Thomas E. Walker, Jeffrey O. Willis and Pascal J. Yvon, Phys. Rev. **B39**, 4285 (1989).

21. E. Garcia, R. R. Ryan, N. N. Sauer, Z. Fisk, B. Pierce, M. Fluss and L. Bernardez, Phys. Rev. **B38**, 2900 (1988).

22. Donald E. Morris, Andrea G. Markelz, John Y. T. Wei, Charles T. Hultgren and Janice H. Nickel, Phys. Rev. **B44**, 9556 (1991).

23. M. L. Cohen, private communication.

24. L. C. Bourne, A. Zettl, T. W. Barbee III and Marvin L. Cohen, Phys. Rev. **B36**, 3990 (1987).

25. Lin Quan (C. Lin), Wei Yu-nian, Yan Qi-wei, Chen Geng-hua, Zhang-zin, Ning Tai-gang, Ni Yong-ming, Yang Qian-sheng, Liu Chao-xin, Ning Tai-shang, Zaho Jin-Kue, Shao You-yu, Han Shun-hui and Li Jing-yuan, Solid State Commun. **65**, 869 (1988).

26. Takehiko Hidaka, Toshimi Matsui and Yoshihiko Nakagawa, Jpn. J. Appl. Phys. **27**, L553 (1988).

27. Z. Fisk, J. D. Thompson, E. Zirngiebl, J. L. Smith and S.-W. Cheong, Solid State Commun. **62**, 743 (1987).

28. M. L. Cohen, D. E. Morris, A. Stacy and A. Zettl, in *Novel Superconductivity*, V. Kresin and S. Wolf ed., (Plenum, New York, 1987), p. 733.

29. B. Batlogg, G. Kourouklis, W. Wever, R. J. Cava, A. Jayaraman, A. E. White, K. T. Short, L. W. Rupp and E. A. Rietman, Phys. Rev. Lett. **59**, 912 (1987).

30. Tanya A. Faltens, William K. Ham, Steven W. Keller, Kevin J. Leary, James N. Michaels, Angelica M. Stacy, Hans-Conrad zur Loye, Donald E. Morris, T. W. Barbee III, L. C. Bourne, Marvin L. Cohen, S. Hoen and A. Zettl, Phys. Rev. Lett. **59**, 915 (1987).

31. L. C. Bourne, S. Hoen, M. F. Crommie, W. N. Creager, A. Zettl, M. L. Cohen, L. Bernardez, J. Kinney and D. E. Morris, Solid State Commun. **67**, 707 (1988).

32. B. Batlogg, R. J. Cava and M. Stavalo, Phys. Rev. **B60**, 754 (1988).

33. D. G. Hinks, D. R. Richards, B. Dabrowski, D. T. Marx and A. W. Mitchell, Nature **335**, 419 (1988).

34. B. Batlogg, R. J. Cava, Jr. L. W. Rupp, A. M. Mujsce, J. J. Krajewski, J. P. Remeika, Jr. W. F. Peck, A. S. Cooper and G. P. Espinosa, Phys. Rev. Lett. **61**, 1670 (1988).

35. H. Katayama-Yoshida, T. Hirooka, A. Oyamada, Y. Odabe, T. Takahashi, T. Sasaki, A. Ochiai, T. Suzuki, A. J. Mascarenhas, J. I Pankove, T. F. Ciszek, S. K. Deb, R. B. Goldfarb and Youngkang Li, (unpublished).

36. N. A. Babushkina, A. V. Inyushkin, I. Yu. Kalnova, I. K. Kobrin, A. K. Kuzakov, A. B. Myasoedov, V. I. Ozhogin, L. L . Shustov, A. N. Taldenkov, N. S. Tolmacheva and S. E. Voinova, Physica **C162-164**, 877 (1989).

37. M. L. Cohen, private communication

38. R. Beyers, B. T. Ahn, G. Gorman, V. Y. Lee, S. S. P. Parkin, M. L. Ramirez, K. P. Roche, J. E. Vazquez, T. M. Gür and R. A. Huggins, Nature **340**, 619 (1989); B. T. Ahn, T. M. Gür, R. A. Huggins, R. Beyers, E. M. Engler, P. M. Grant, S. S. P. Parkin, G. Lim, M. L. Ramirez, K. P.

Roch, J. E. Vazquez, V. Y. Lee and R. D. Jacowitz, Physica **C153-155**, 590 (1988).

39. G. Ceder, R. McCormack and D. de Fontaine, Phys. Rev. **B44**, 2377 (1991).

40. J. P. Franck, J. Jung, M. A.-K. Mohamed, S. Gygax and G. I. Sproule, Physica **B169**, 697 (1991).

41. M. K. Crawford, W. E. Farneth, E. M. McCarron, R. L. Harlow and A. H. Moudden, Science **250**, 1390 (1990).

42. J. D. Axe, A. H. Moudden, D. Hohlwein, D. E. Cox, K. M. Mohanty, A. R. Moodenbaugh and Youwen Xu, Phys. Rev. Lett. **62**, 2751 (1989).

43. Vincent H. Crespi and Marvin L. Cohen, Phys. Rev. **B44**, 4712 (1991).

44. S. Flach, P. Härtwich and J. Schreiber, Solid State Comm. **75**, 647 (1990).

45. J. C. Phillips, Phys. Rev. **B43**, 6257 (1991).

46. C. C. Tsuei, D. M. Newns, C. C. Chi and P. C. Pattnaik, Phys. Rev. Lett. **65**, 2724 (1990); however, a recent paper (D. R. Penn and Marvin L. Cohen, Phys. Rev. **B46**, 5466 (1992) ) suggests that $\alpha$ vs $T_c$ cannot be explained solely by singularities in the electronic density of states.

47. Maria Ronay, M. A. Frisch and T. R. McGuire, Phys. Rev. **B45**, 355 (1992).

48. S. Hoen, W. N. Creager, L. C. Bourne, M. F. Crommie, T. W. Barbee III, Marvin L. Cohen, A. Zettl, Luis Bernardez and John Kinney, Phys. Rev. **B39**, 2269 (1989).

# Chapter 3: Oxygen Isotope Study of $YBa_2Cu_3O_7$

## 3.1 Overview

We report here on a detailed study of the oxygen isotope effect in $YBa_2Cu_3O_7$, where up to 94% of the $^{16}O$ in the sample was replaced by $^{18}O$. Multiple cross-exchanges of oxygen isotopes were performed in high quality sample/control pairs to eliminate $T_c$ shifts not associated with isotopic mass. Time dependent effects were also studied by monitoring transition temperatures for various isotopically substituted samples over a period of 5 months.

As discussed in Chapter 2, several studies have been performed to examine isotope effects in oxide superconductors. The first experiments[1, 2] involved oxygen isotope substitution in $YBa_2Cu_3O_7$, and found no or very little shift, with $\alpha \cong 0.0 \pm .03$. This small value of $\alpha$ is not easily explained within the standard two square well model if $T_c$~90K, and is thus suggestive of a non-phonon pairing mechanism. Later studies,[3-5] on the other hand, indicated that for oxygen isotope substitution in $YBa_2Cu_3O_7$, $\alpha$ might be as large as 0.12, or even greater than 3.5. Hence, the findings to date are contradictory. Since different pairing mechanisms yield different values of $\alpha$, it is important to establish the magnitude of the isotope shift.

We find that a small but finite oxygen isotope effect occurs in $YBa_2Cu_3O_7$. Magnetic measurements indicate that for the bulk material $\alpha_{bulk} = 0.019 \pm .004$. Resistivity measurements in freshly prepared samples show evidence for filamentary superconductivity occurring one to two Kelvin above the bulk superconducting transition temperature. The isotope shift associated with the filamentary superconductivity is similar

to but slightly larger than the bulk shift: $\alpha_{fil}$= 0.028±.003. The transition temperature for filamentary superconductivity is not stable, but decays smoothly toward the bulk transition temperature over a period of several months. Our observed values of $\alpha$ are within the error limits of several previous $YBa_2Cu_3O_7$ oxygen isotope studies,[1, 2, 6, 7] but are inconsistent with other findings.[3-5] We show that our values of $\alpha$ cannot be explained within a standard three dimensional phonon-mediated pairing model, and we examine other possible mechanisms.

The remainder of this paper is organized as follows: Sec. 3.2 describes the experimental configuration including sample preparation, isotopic exchange, and measurement techniques. Sec. 3.3 presents our isotope shift results which are discussed in Sec. 3.4. A conclusion follows in Sec. 3.5.

## 3.2 Experimental method

### 3.21 Sample preparation

Polycrystalline samples of $YBa_2Cu_3O_7$ were produced by the solid state reaction of high purity (99.999%) powders of $Y_2O_3$, $BaCO_3$, and CuO. Polycrystalline, rather than single-crystal, samples allow larger sample sizes necessary for dc magnetic characterization, the best determination of $T_c$ over the entire sample volume. Moreover, the small crystallite volume with the polycrystalline sample ensures that uniform oxygen diffusion through the crystallite volume occurs on reasonable time scales. Thin-film samples represent an alternative approach for reasonable diffusion times and dc magnetic characterization (if the film is mounted perpendicular to the applied magnetic field).

All grinding was done in an agate mortar in a nitrogen filled glove box to maintain high purity and to reduce the deleterious effects of water vapor. The precalcining and subsequent sintering heat treatments used gold foil as a substrate to minimize contamination. The mixed powders were heated to 850°C, held for 15 hours, then cooled over 8 hours to room temperature. The resulting blackened powder was reground and calcined at 930°C for 15 hours then cooled to room temperature over 9 hours. This powder was reground, pelletized, and sintered at 930°C for 15 hours then cooled over 9 hours. After the final heat cycle the pellets were stored with a desiccant, $P_2O_5$, in vials and the vials were kept in an evacuated desiccator.

Samples of $YBa_2Cu_3O_7$ produced by the above procedure were characterized by magnetic susceptibility and dc resistivity measurements. $T_c$'s were typically near 92K with sharp transitions. Full magnetic transition widths were 2-3K, with 50% Meissner signals.

**3.22 Isotope exchange and measurement technique**

The isotope exchange was achieved with a high-temperature gas diffusion technique and after each exchange the samples were characterized magnetically and resistively. To reduce the effects of any existing sample inhomogeneities in the initial samples or differences (unrelated to isotopic species) introduced during the high temperature exchange process, we designed an experimental procedure which averaged out such deviations. As outlined in Fig. 3-1, four $YBa_2Cu_3O_7$ pellets (two pairs) of near identical weights were chosen and each pellet underwent several oxygen isotope exchanges. Within each pair, one sample was

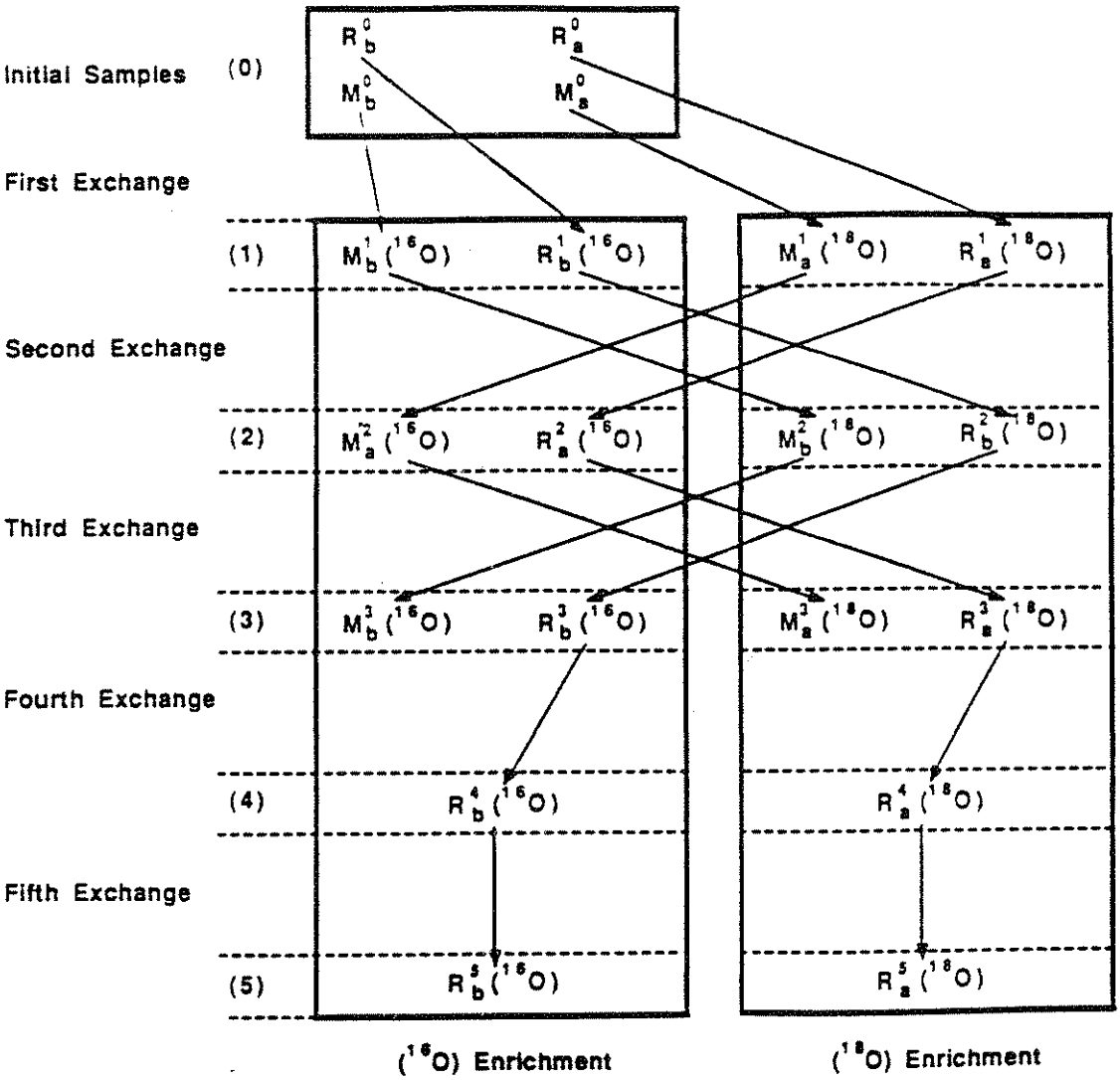


Fig. 3-1. Schematic of $^{16}O$ and $^{18}O$ isotope exchange. R and M refer to samples used for resistive and magnetic tests, respectively. Subscripts differentiate between different samples and superscripts refer to the last exchange that the sample has undergone. The number in parenthesis refer to the associated curves in Figs. 3-4 and 3-5.

designated primarily for resistive tests ($R_a$ or $R_b$) and one sample was designated primarily for magnetic tests ($M_a$ or $M_b$).

To accomplish isotopic exchange, the samples were placed on platinum boats in identical quartz tubes. The quartz tubes were placed side-by-side and equidistant from the coils of a small tube furnace as depicted in Fig. 3-2. The quartz tubes were coupled to similar static gas reservoirs containing 99.99% pure $^{16}O$ and 95% (occasionally 99%) enriched $^{18}O$, respectively. At room temperature the pressures in the two reservoirs were 740 torr and during the exchange, they would rise to 750 torr. In each of the first three exchanges, the samples were heated to 950°C over 2 hours, held for 10 hours, cooled to 300°C over 9 hours, then cooled in the oven to room temperature. In one test, the $^{16}O$ and $^{18}O$ gases were switched between reservoirs to ensure that no asymmetries existed in the isotope exchange apparatus; none were found.

After each exchange, a small chip was removed from each of the two samples designated for resistance measurements ($R_a$ and $R_b$). The chips were mounted in the standard four probe resistance measurement configuration with silver paint contacts, and placed side-by-side on a solid copper probe in close proximity to a calibrated diode thermometer. The samples were cooled with a helium gas flow system. The resistance versus temperature curve for each sample did not change when the sample positions on the copper probe were interchanged, indicating negligible thermal gradients across the copper probe. Each resistance measurement at a given temperature was performed with forward and then reversed dc current (typically 1mA) to ensure freedom from thermal EMF's.

# OXYGEN ISOTOPE SUBSTITUTION

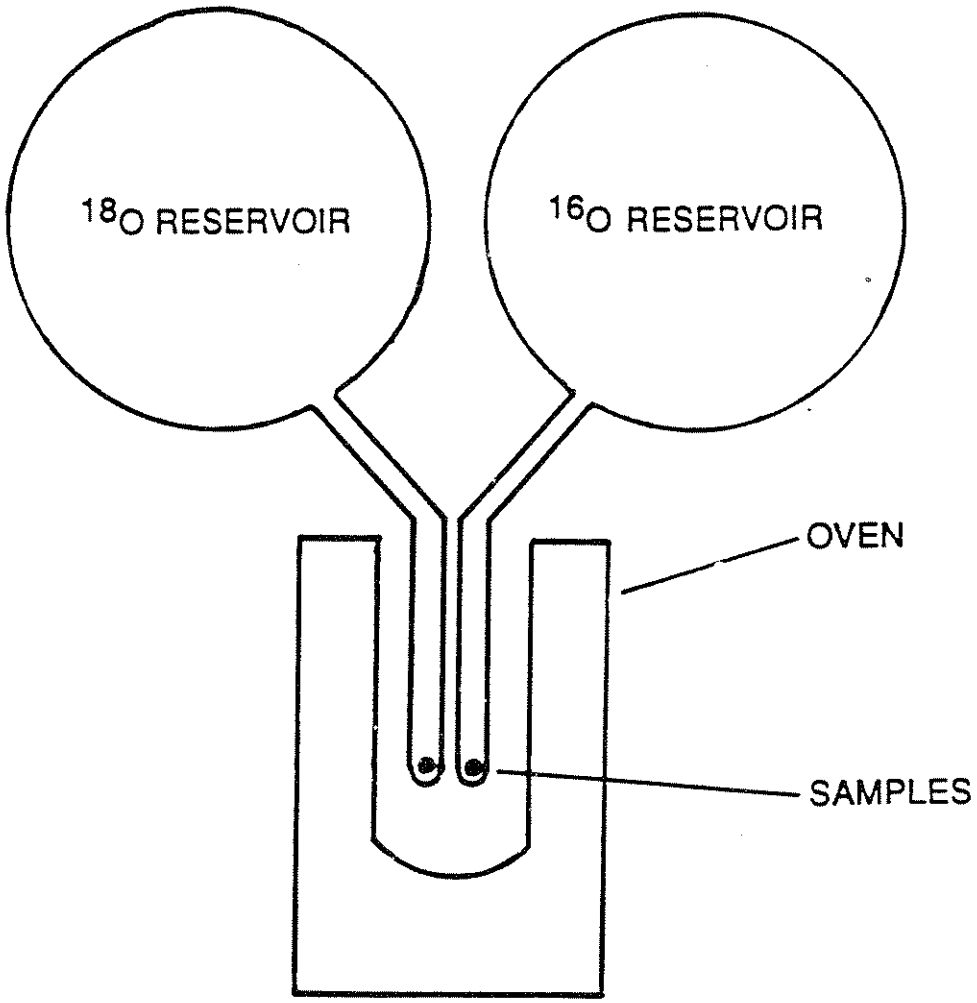


Fig. 3-2. Schematic diagram of apparatus to perform high temperature oxygen exchange. The $^{16}O$ and $^{18}O$ reservoirs contain ~1 liter of gas and represent ~95% of the enclosed volume. The samples sit side by side (~1cm apart) in quartz tubes within the high temperature oven.

We measured the magnetic susceptibility (usually of samples $M_a$ and $M_b$) using a S.H.E. model VTS-805 SQUID magnetometer which we modified to allow the sample temperature to be regulated with greater precision and determined with greater accuracy than possible with the standard magnetometer configuration. The sample was hung in a copper container in close thermal contact to a diode. Samples $M_a$ and $M_b$ were kept geometrically intact throughout the series of isotopic exchanges and magnetic measurements to avoid errors from changing the geometrical demagnetization factors for the samples. To remove temperature gradients within the sample tube, we stabilized the system at a temperature slightly above the transition for thirty minutes. A computer controlled the slow downward temperature drift (0.01K/min.) for the samples in the magnetometer and recorded their magnetization typically 12 times per .1 degree. Subsequent tests have verified that the temperature of the samples was accurate to 0.05K and repeatable between runs to 0.03K. The magnetic field was typically 2-3 Oe and was calibrated before each run by measuring the magnetization of a small superconducting tin sphere. The susceptibility of a given sample at T=40K, well below the transition, varied by as much as 10% between repeated magnetization measurements due to flux-trapping effects, but the susceptibility curves for any given sample at higher temperatures near $T_c$ were found to be repeatable.

Isotopic determination was done both by weighing the samples before and after the exchange and by the more accurate method of Laser-Assisted Ion Mass Analysis (LIMA) depicted in Fig. 3-3. In the LIMA technique, a 4eV laser vaporizes and ionizes a small portion of the sample. Constituents of the resulting plasma are driven through a time of flight

# LASER-INDUCED ION MASS ANALYSIS (LIMA)

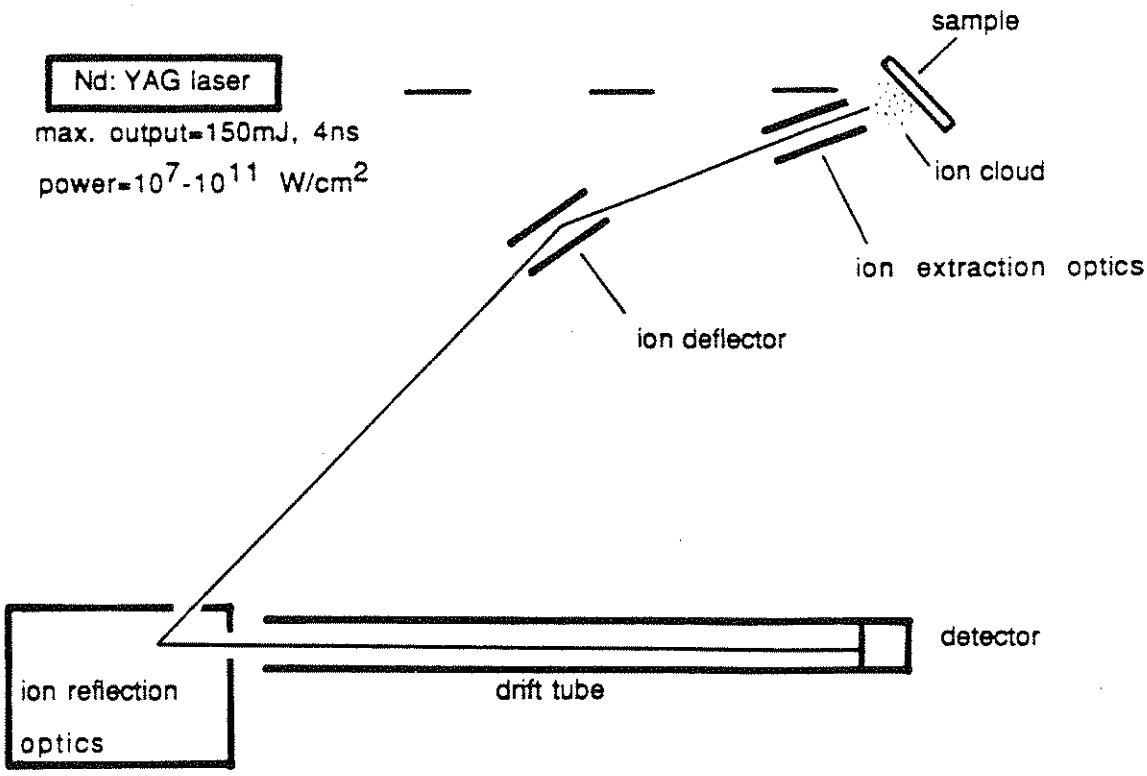


Luis Bernardez
John Kinney
Lawrence Livermore National Laboratory

Fig. 3-3. Schematic diagram of laser-induced ion mass analysis (LIMA) apparatus used to determine the isotopic contents of the samples.

spectrometer, thus determining (within approximately 1 or 2% accuracy) relative isotopic content of the sample. The samples were examined at different locations across their surface, and as a function of depth into the bulk. No evidence for inhomogeneous isotopic enhancement was found. For analysis purposes, we shall use the LIMA results for the isotopic enrichment, which agree to within ~10% of those determined by sample weight changes.

### 3.3 Results

Fig. 3-4 shows the results of resistive and magnetic measurements for the pure and isotopically exchanged $YBa_2Cu_3O_7$ samples. Graphs (0) show R(T) and $\chi$(T) for the samples as initially prepared. Graphs (1)-(3) show resistive and magnetic data for the sample sets following the first, second, and third exchanges, respectively (see Fig. 1). Ideally, the sample data plotted together should be identical in (0), and the curves for $^{16}O$ and $^{18}O$ enriched pellets in (1) should reflect directly any oxygen isotope shift. The curve for a given sample would then be expected to switch between the $^{16}O$ and $^{18}O$ positions in subsequent frames after each isotope exchange step. This ideal situation is not realized in Fig. 3-4 because the initial samples already show slightly different $T_c$'s. Nevertheless, for each sample, both resistive and magnetic measurements exhibit a clear pattern of oscillation between a higher value of $T_c$ for $^{16}O$ enrichment and a lower value of $T_c$ for $^{18}O$ enrichment as one progresses from graphs (0) to (3).

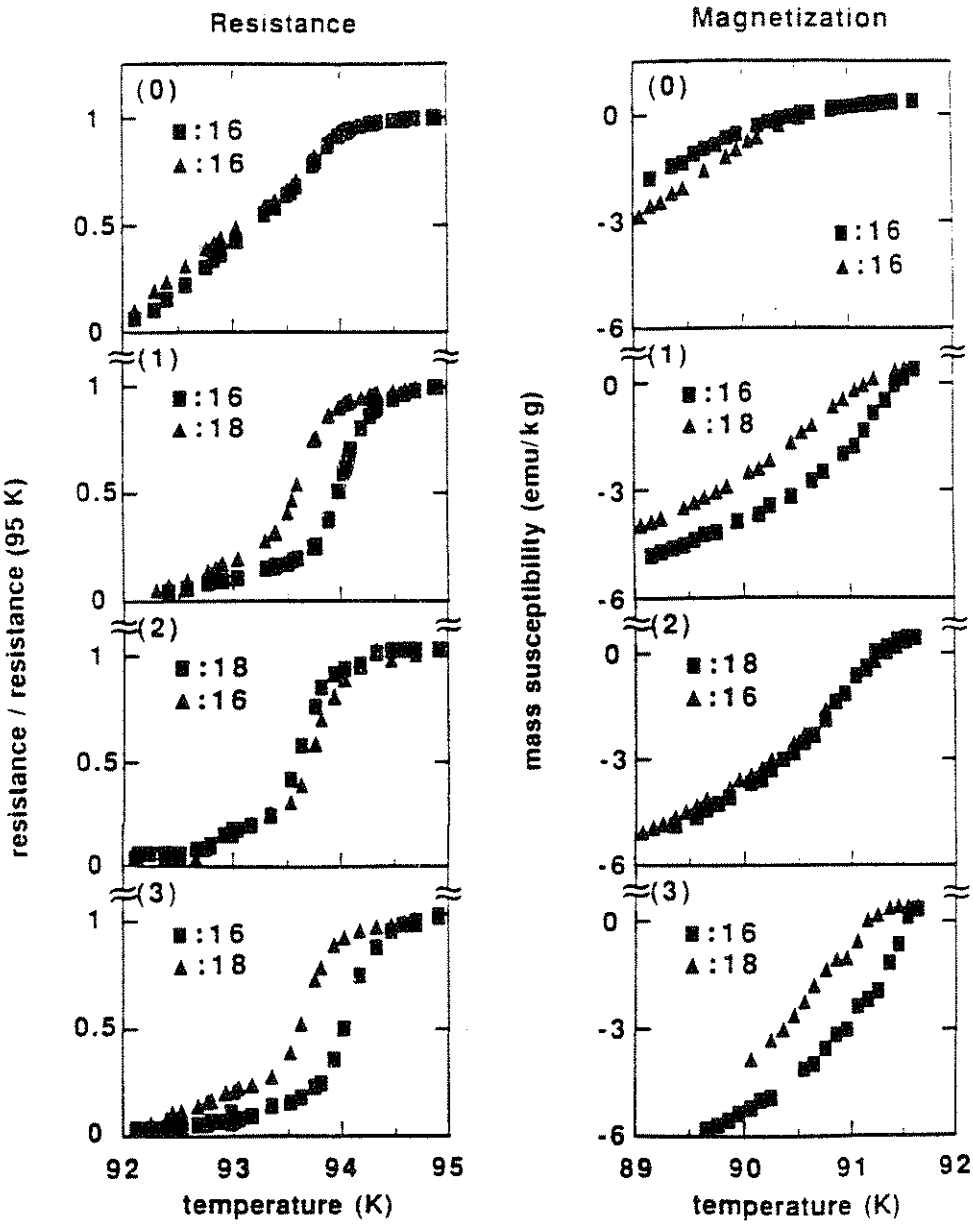


Fig. 3-4. Resistance vs temperature for samples $R_a$ and $R_b$, and magnetization vs temperature for samples $M_a$ and $M_b$: (0) immediately after initial preparation of the samples; (1) after the first isotopic exchange; (2) after the second exchange; (3) after the third exchange.

Table 3.1 summarizes the isotope shift information drawn from the data illustrated in Fig. 3-4. For resistance samples $R_a$ and $R_b$, the transition temperature was taken to be the temperature midway between the temperatures where the sample resistance was 90% and 50% of the normal state resistance at 95.05K. For magnetization samples $M_a$ and $M_b$ measured after the second or third exchange, the transition temperature was taken to be the temperature midway between the temperatures where the sample magnetization was 10% and 50% of the superconducting state magnetization at 89.55K. The onset temperature of the transition for the magnetization samples after only one exchange is about a degree lower than the onset after the samples had further exchanges; the transition temperatures after the first exchange were accordingly normalized to 88.45K for the magnetization samples. We chose not to normalize the magnetization measurements to the values of the magnetic moment at lower temperatures because flux trapping was found to contaminate the measurements well below the transition temperature. Using these definitions of $T_c$, Table 3.1 gives the change in transition temperature for each sample after each isotopic exchange relative to its transition temperature before the exchange. The change in transition temperature could in principle be due to both an isotope effect and the annealing cycle; by subtracting the change in transition temperature for the $^{18}O$ sample from the change for the $^{16}O$ sample the effects of the annealing cycle are canceled. The relative $T_c$ shift must be divided by two for the second and third exchanges to obtain the net shift since these are cross exchanges. The spread is the variation of the relative $T_c$ shift over half the transition

**Resistance Samples**

| | $R_a$ | | | $R_b$ | | | Relative $T_c$ Shift (K) |
|---|---|---|---|---|---|---|---|
| | $\Delta T_c$ (K) | Spread (K) | % Isotope Enrichment | $\Delta T_c$ (K) | Spread (K) | % Isotope Enrichment | |
| After first exchange | +.303 | .205 | 75.3 ($^{18}O$) | +.601 | .183 | 100 ($^{16}O$) | +.298 |
| After second exchange | +.150 | .003 | 84.6 ($^{16}O$) | -.379 | .007 | 73.3 ($^{18}O$) | +.265 |
| After third exchange | -.017 | .084 | 84.3 ($^{18}O$) | +.440 | .010 | 88.9 ($^{16}O$) | +.229 |

**Magnetization Samples**

| | $M_a$ | | $M_b$ | | Relative $T_c$ Shift (K) |
|---|---|---|---|---|---|
| | $\Delta T_c$ (K) | Spread (K) | $\Delta T_c$ (K) | Spread (K) | |
| After first exchange | +.285 | .065 | +.640 | .210 | +.355 |
| After second exchange | +.030 | .010 | -.255 | .015 | +.143 |
| After third exchange | -.095 | .045 | +.295 | .005 | +.195 |

Table 3.1. Isotope shift information for resistance and magnetization samples.

width according to the above definitions. The results of the LIMA measurements of isotopic enrichment are also shown in the table.

The resistive and magnetic data taken after the second and third exchanges are most appropriate for extracting a net isotope shift. The exchanges are both cross-exchanges, and the data reveal sharp transitions and consistent $^{18}O$ isotope enrichments of approximately 80%. From Table 3.1 we determine from resistance measurements a net oxygen isotope shift in $YBa_2Cu_3O_7$ of -0.25±.02K, and from magnetization measurements a net shift of -0.17±.03K. In the discussion section below, we extrapolate these shifts to full oxygen isotope substitution and determine corresponding values of $\alpha$.

After the three isotope exchanges discussed above, two additional exchanges were performed to increase the relative $^{18}O$ content of a particular specimen (sample $R_a$) as much as possible. The additional exchange sequences are also shown in Fig. 3-1. In the fourth exchange, the ~95% enriched $^{18}O$ from the third exchange experiment was reused in the $^{18}O$ arm of the exchange apparatus, and the samples were held at 950°C for 25 hours and cooled to 300°C over 9 hours. In the fifth exchange, the samples were held at 950°C for 40 hours before cooling to 300°C over 9 hours, and the purity of the $^{18}O$ exchange gas was increased to 99% enrichment.

The results of the fourth and fifth exchanges are shown in Fig. 3-5, together with the results of the third exchange. The third exchange data, Fig. 3-5, graph (3), correspond to 84% enrichment of the $^{18}O$ sample. The isotopic enrichment for the $^{18}O$ sample after the fourth exchange was increased to 91%, and to 94% after the fifth exchange. Fig. 3-5 shows a

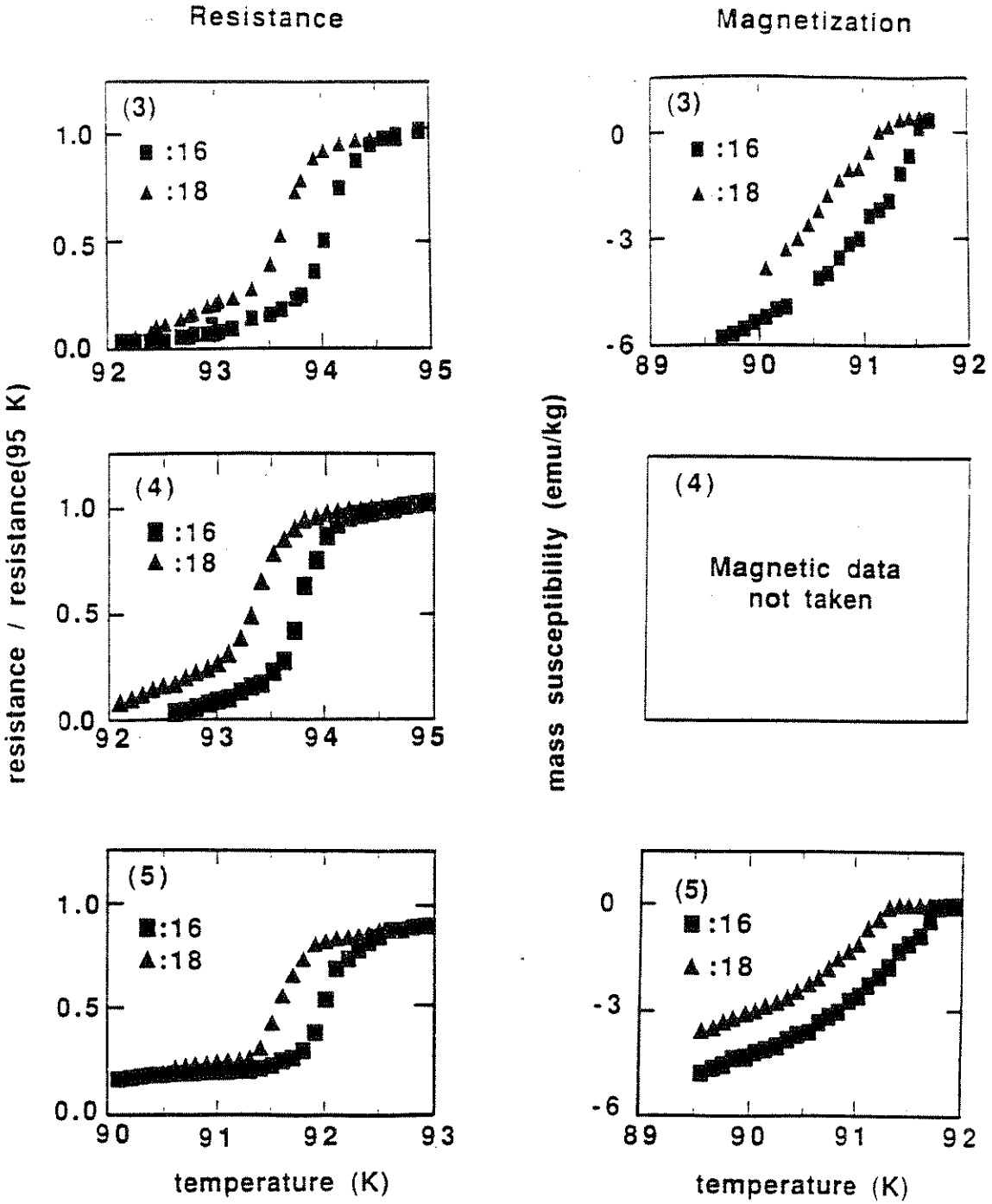


Fig. 3-5. Resistive and magnetic transitions of oxygen exchanged samples: (3) after third exchange, one week after initial production of the samples; (4) after fourth exchange, one month later; (5) after fifth exchange, five months after initial production. The magnetization measurement (3) was performed on samples $M_a^3$ and $M_b^3$ while (5) was performed on samples $R_a^5$ and $R_b^5$.

similar isotope shift between $^{16}O$ and $^{18}O$ samples following the fourth and fifth exchanges as was observed following the third exchange. This suggests that the few $^{16}O$ atoms which remain in the $YBa_2Cu_3O_7$ lattice in a typical $^{18}O$ substitution experiment do not by some unusual mechanism mask a large intrinsic isotope shift.

The data of Figs. 3-4 and 3-5 also illustrate interesting time dependent phenomena. Although the isotope exchanges and measurements of Fig. 3-4 were all performed within several weeks of the initial sample synthesis, the measurements described in Fig. 3-5 span a period of five months. In Fig. 3-5, the data in graph (3) were recorded on fresh samples, two weeks after initial synthesis. The data of graphs (4) and (5) were recorded 1 1/2 and five months after initial synthesis, respectively.

Fig. 3-4 shows that the superconducting transition temperature determined resistively is consistently between one and two Kelvin higher than that determined magnetically for the corresponding sample. We identify the magnetic transition temperature as representing $T_c$ for the bulk material. The higher resistive transitions are taken as evidence for filamentary superconductivity above $T_c$(bulk). Fig. 3-5 shows that the bulk superconducting transition temperature is relatively time independent: the magnetization graphs (3) and (5) have nearly identical onset temperatures for a given isotope, even though the measurements were taken 5 months apart. On the other hand, the resistance data of Fig. 3-5 show a steady decrease in $T_c$ with time. For example, the $^{16}O$ sample has a $T_c$ near 94K in graph (3), and a $T_c$ near 92K in graph (5). The later $T_c$ corresponds to that determined magnetically for the same specimen. This indicates that the filamentary superconductivity is time dependent and

disappears after several months. The resistive and magnetic transition temperatures coincide thereafter.

Apparently resistive measurements near $T_c$ test a small portion of the material (estimated from our magnetic data to be less than 0.3% volume fraction of the specimen) which is compositionally different from the bulk and undergoes "degradation" faster than the bulk. Over the span of 5 months, the bulk properties remained constant while the resistive transition shifted steadily downward. It seems likely that the filamentary superconductivity is restricted to regions of high oxygen or impurity mobility such as those between grains or within a small distance of the grain boundaries. Figs. 3-4 and 3-5 and Table 3.1 show, however, that the filamentary superconductivity experiences an oxygen isotope shift similar to that of the bulk $YBa_2Cu_3O_7$ and that the relative shift remains constant in time.

### 3.4 Discussion

#### 3.41 Discussion of $\alpha$

The results of our oxygen isotope cross-exchange experiments described in Fig. 3-4 and Table 3.1 unequivocally demonstrate a small but finite superconducting transition temperature shift between $^{16}O$ and $^{18}O$ samples of $YBa_2Cu_3O_7$. The calculation of the appropriate $\alpha$ for full oxygen substitution from the observed $T_c$ shifts is not immediately obvious for two reasons. First, our experiments did not achieve 100% $^{18}O$ replacement for $^{16}O$, and second, oxygen constitutes only 54% of the total number of atomic sites in $YBa_2Cu_3O_7$. The first problem can be corrected by extrapolating our measured $T_c$ shifts to 100% oxygen isotope

replacement. The second complication must be addressed when comparison is made between our measured $\alpha$ and that predicted by various models.

Of the four inequivalent oxygen sites within the $YBa_2Cu_3O_7$ unit cell, one (O1) is singly occupied and three (O2,O3,O4) are doubly occupied. It is desired to extrapolate the measured $T_c$ shift to an effective shift (and $\alpha$) which would occur with complete substitution at each of the four sites. For each site, there will be a different shift of the transition temperature with complete $^{16}O$ to $^{18}O$ exchange. If there were non-uniform substitution of oxygen atoms, then a site on which $T_c$ were particularly dependent could be left unsubstituted. For the chain site(O1) to be left unsubstituted, the sample must contain less than 86% $^{18}O$, and for any other site, no more than 72% could be exchanged. With our 91% and 94% exchange achieved in the fourth and fifth exchanges, at least half of any particular site must have been substituted. From the constancy of the relative shifts, we deduce that incomplete substitution is not a serious concern in our isotope shift determination.

At least two methods can be used to extrapolate the measured $T_c$ shifts to 100% isotopic substitution. In one method, one assumes that the mass that enters into $T_c \propto M^{-\alpha}$ is in fact an average over all similar sites; thus, for 75% $^{18}O$ substitution, a mass of 17.5 is used. Alternatively, one can divide the shift by the isotopic ratio, (# of $^{18}O$ atoms)/(Total # of oxygen atoms), to normalize the shift to 100% substitution. In practice, these two methods differ in the calculated value of $\alpha$ by only a few percent, less than the typical experimental error. Here, we use the latter method.

To determine $\alpha$ for the bulk material, we use the averaged shift obtained from magnetic measurements at approximately 80% $^{18}O$ enrichment: $\Delta T_c$= -0.17±.03K, with $T_c$=92K. This leads to an effective $YBa_2Cu_3O_7$ oxygen isotope exponent of $\alpha_{bulk}$ = 0.019±.004. The resistive data for similar $^{18}O$ enrichment yield an oxygen isotope effect relevant to the filamentary superconductivity in $YBa_2Cu_3O_7$. From $\Delta T_c$= -0.25±.02K and $T_c$=94K, we find $\alpha_{fil}$ = 0.028±.003. Hence the isotope effect for the bulk material and that for the filamentary regions are very similar, and this suggests that the bulk and filamentary regions are structurally similar. Our value of $\alpha_{bulk}$ lies within the original error limits set by Bourne *et al.*[1] and Batlogg *et al.*[2] for oxygen isotope substitution in bulk $YBa_2Cu_3O_7$. Fig. 3-6 gives a graphic summary of oxygen isotope effects reported to date for $YBa_2Cu_3O_7$.

Interpretation of the isotope shift is less straightforward in compounds than in elemental solids. Anharmonic and zero point motion effects can cause anomalous changes in $T_c$ upon isotopic substitution. In PdH, for example, substitution of D or T for H results in a substantial increase in $T_c$ and a large negative value for $\alpha$.[8] Even in the absence of these effects, the meaning of $\alpha$ in the relationship $T_c \propto M^{-\alpha}$ is not obvious. In superconducting compounds, $\alpha$ is conventionally expressed as $\alpha = \Sigma\alpha_i$ and $T_c \propto \Pi M_i^{-\alpha_i}$ where $M_i$ is the mass of the atom in the $i^{th}$ position within the unit cell. Since different lattice positions contribute to the phonon spectrum in different ways, the various $\alpha_i$ are unlikely to be equal. To perform a theoretical calculation of $\alpha_i$, it would be necessary to know how each lattice site affects each portion of the phonon spectrum and which phonons were active in binding the electrons. More

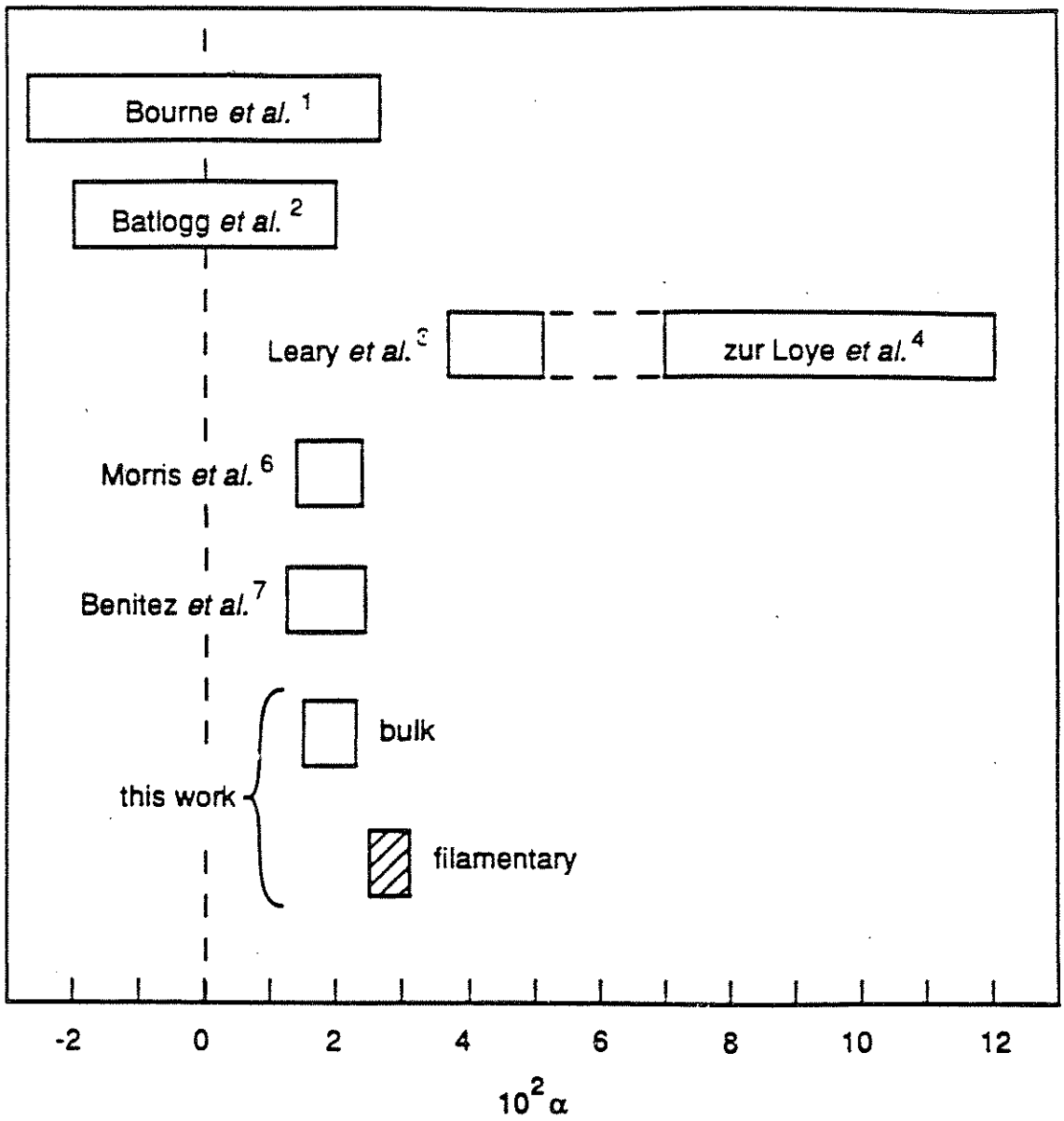


Fig. 3-6. Graphical plot of the reported values of the oxygen isotope exponent $\alpha$ in $YBa_2Cu_3O_7$. The appropriate reference is noted alongside the first author of a particular experiment.

simply, an effective $\alpha'$ can be calculated by assuming an equal scaling of all atomic masses $M_i$ by a factor $\gamma$: $M_i' = \gamma M_i$. The phonon spectrum will then scale in frequency as $\omega' = \omega/\gamma^{1/2}$, and the resulting shift in $T_c$ can be used to define $\alpha' = -\Delta \ln T_c/\Delta \ln M = -\Delta \ln T_c/\ln\gamma$. The above definition of $\alpha_i$ ensures that in the limit of infinitesimal mass changes, $\alpha' = \Sigma\alpha_i$.

In the particular case of oxygen substitution at the four inequivalent sites in $YBa_2Cu_3O_7$, we expect the resulting oxygen isotope exponent $\alpha_O = \alpha_{O1} + \alpha_{O2} + \alpha_{O3} + \alpha_{O4}$ to be nearly equal to the theoretically derived $\alpha'$. Oxygen is much lighter than the other elements so most of the significant features in the phonon spectrum are dependent on oxygen mass.[9] Moreover, band structure calculations[10] indicate that the Fermi surface electrons are an admixture of Cu d-orbital and O p-orbital states. Oxygen vibrations should thus be coupled strongly to those states which condense into the superconducting state. A one-square-well BCS model will not describe this compound since experiments with Ba,[11, 12] Cu[11, 13] and rare earths[14] have shown that $\alpha' = \alpha_Y + \alpha_{Ba} + \alpha_{Cu} + \alpha_O < 0.5$.

**3.42 Other experiments**

Several isotope shift measurements have occurred after the completion of our experiment and deserve mention. Kobiela *et al.*[15] found a small shift (~ 0.3K ± 0.2K) when Cu, Ba, and Y metal particles were used as precursors. Yvon *et al.*,[16] by burning the intermetallic $YBa_2Cu_3$ in the appropriate oxygen environment, found shifts of 0.4K ± 0.1K. Franck *et al.*,[17] using oxides of Cu and Ba which already contained $^{18}O$, determined shifts of 0.4K to 1.7K.

These experiments respond to the general concern that in gas exchange the varying diffusion rates between the different oxygen lattice

sites may cause inhomogeneous enrichment. In particular, Grimsditch *et al.*[18] have suggested that the O4 or apical oxygen site may have been poorly enriched. However, more recent Raman work[19] has demonstrated that, though oxygen diffusion is slower into the apical sites than the chain sites, it is still much more rapid than diffusion into the plane sites (O2, O3). Even though our and other experiments have large enough isotope exchanges (>91%) to assure that every lattice site is at least 50% enriched, it has been suggested that a non-linear relationship between isotopic enrichment and $T_c$ for certain lattice sites may mask the "true" isotope effect.[18]

By starting with materials that already contain $^{18}O$, the above experiments[15-17] ensure a more uniform isotopic distribution. That none of them demonstrate large isotope shifts reconfirms the small value of $\alpha$ for this material. Moreover, each of these experiments suffers from poor sample quality as evidenced by large magnetic transitions widths (14K - 30K) and incomplete resistive transitions. In our experience, the transition temperature is extremely sensitive to small compositional changes. An example of this sensitivity is shown in Fig. 3-4 (0) where the magnetic transitions of 2 'identically' prepared samples still show shifts of ~ 0.2K. In fact, if a single pellet with a 3K - 4K magnetic transition width is broken in half, two pieces would still show relative $T_c$ shifts of ~ 0.2K. It is only by doing simultaneous cross-exchanges that it is possible to cancel out the effects of compositional and processing differences.

**3.43 BCS theory**

The small observed value of $\alpha$ and the high $T_c$~90K suggest the possibility that the electron pairing mechanism in $YBa_2Cu_3O_7$ differs from

that of low transition temperature superconductors. We first examine the consequences of the observed isotope shift of three dimensional BCS phonon-mediated pairing. We then discuss alternative models in Sect. 3.44.

To test the applicability of the standard isotropic three-dimensional phonon-mediated model of superconductivity to $YBa_2Cu_3O_7$, we calculate transition temperatures and isotope shifts from the electron-phonon interaction spectrum $\alpha^2F(\omega)$ and the Coulomb repulsion parameter $\mu^*$ using the Matsubara representation[20] of the Eliashberg theory.[21] The isotope effect exponent $\alpha$ is not related to the electron-phonon matrix element which is also represented by an $\alpha$ in $\alpha^2F(\omega)$. We consider several different models of the electron-phonon interaction spectrum $\alpha^2F(\omega)$ to test the dependence of the isotope shift $\alpha$ on $\alpha^2F(\omega)$.

We consider a simple model of oxygen isotope substitution in which only the high-frequency peaks in $\alpha^2F(\omega)$ are shifted, and assume that the repulsive Coulomb interaction $\mu$ is independent of isotopic mass. Hence, the calculated isotope effects are obtained by simulating the change in the frequency of the phonons arising from the substitution of one isotope for another.

Since shifting the entire $\alpha^2F(\omega)$ spectrum would be appropriate only for calculating the isotope effect in the case of an elemental superconductor, we have also calculated the shifts resulting from shifting only the high-frequency half of $\alpha^2F(\omega)$ as a simple approximation for oxygen substitution. Figure 3-7 shows the calculated isotope effects for shifting the entire $\alpha^2F(\omega)$ spectrum. We find that the calculated values of the isotope effect are independent of the shape of $\alpha^2F(\omega)$ for small values

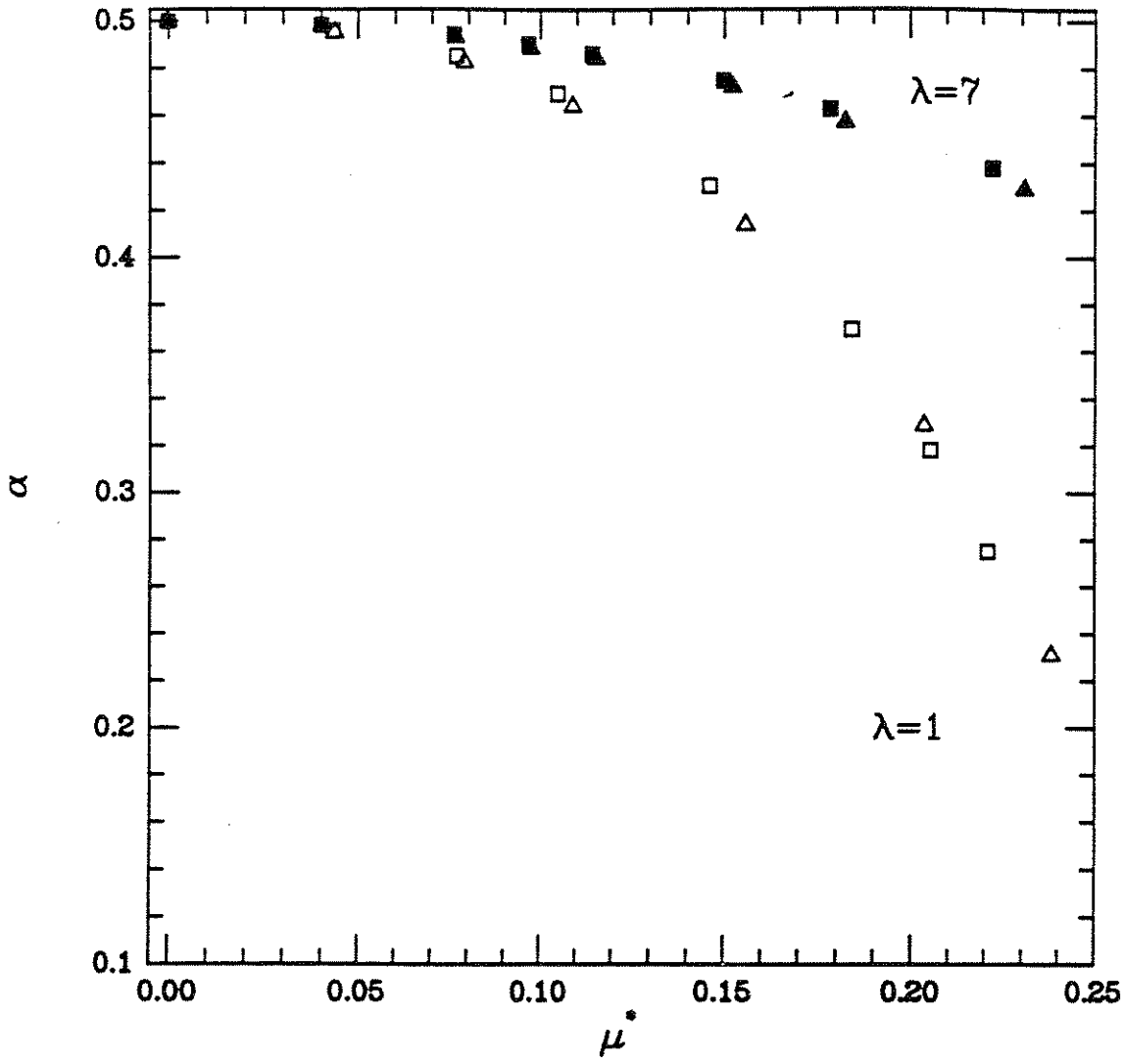


Fig. 3-7. Values of α calculated for λ = 1 (open symbols) and λ = 7 (filled symbols) using an Einstein phonon spectrum (squares) and a model $La_{1.85}Sr_{0.15}CuO_4$ spectrum (triangles). At constant λ, the values of α are nearly independent of the shape of the phonon spectrum.

of $\mu^*$ and exhibit only a small amount of scatter for extremely large values of $\mu^*$, where $\mu^*$ is the renormalized Coulomb interaction evaluated at the root-mean-square phonon frequency. Therefore, we expect that small differences between our model spectra and the actual $\alpha^2F(\omega)$ in $YBa_2Cu_3O_7$ will not affect the calculated values of the isotope shifts significantly.

Using electron-phonon spectra similar to those presented in experimental data, we have calculated the isotope effect in $YBa_2Cu_3O_7$ with the goal of determining whether a standard phonon-mediated pairing in three dimensions can be responsible for superconductivity in the ceramic oxides. From the results presented above, we assume the following values for $YBa_2Cu_3O_7$: $\alpha = 0.023 \pm 0.008$ and $T_c \approx 93K$.

For $YBa_2Cu_3O_7$, the experimental results appear to exclude a solely harmonic phonon-mediated isotropic three-dimensional model. Fig. 3-8 shows the results for $YBa_2Cu_3O_7$, with the $T_c = 93K$ isotherm and the lines of constant $\alpha \approx 0.023 \pm 0.008$. When the entire spectrum is shifted, no values of the parameters $\lambda$ and $\mu^*$ will yield the necessary values of $\alpha$ and $T_c$. When we consider a simulated oxygen substitution by shifting only the high-frequency phonon modes, we find that the intersection of the $T_c$ isotherm and the constant-$\alpha$ line occurs for unphysically large $\lambda > 30$. We therefore conclude that our standard three-dimensional harmonic phonon-mediated model is incapable of describing superconductivity in $YBa_2Cu_3O_7$.

### 3.44 Variations on electron-phonon coupling

Several attempts have been made to explain the experimental results by changing features of the standard isotropic three-dimensional model. The idea of reduced dimensionality, based on the one-dimensional chains

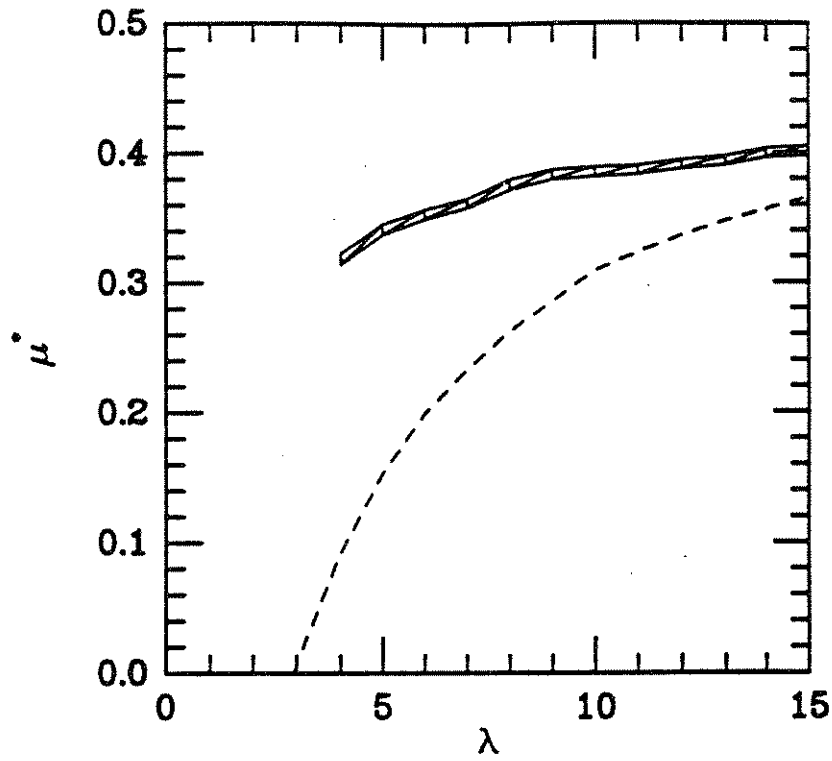


Fig. 3-8. Values of $\lambda$ and $\mu^*$ for which $T_c$ = 93K from numerical calculations (dashed curve). The shaded area represents solutions with $\alpha = 0.023 \pm 0.008$ found numerically by shifting only the phonon spectrum peaks corresponding to oxygen vibrations. An intersection of the solid curve with the shaded area would indicate values of $\lambda$ and $\mu^*$ consistent with phonon-mediated superconductivity in $YBa_2Cu_3O_7$.

or two-dimensional planes occurring in high-$T_c$ superconductors, could possibly explain both the high $T_c$ and small $\alpha$ seen. Labbe and Bok[22] have proposed a two-dimensional model where the Fermi energy occurs near a logarithmic divergence (van Hove singularity) in the electronic density of states, resulting in a large $\lambda$ and a small $\alpha$, since the relevant energy scale is the width of the peak in the density of states rather than $\omega_D$. Tsuei[23] and Newns[24] have recently revived this theory to explain the surprising effects of doping in $La_{2-x}Sr_xCuO_4$ and correlations between the temperature dependence of the resistivity and sample quality. However, photoemission studies have yet to find any peak in the electronic density of states and its believed that the structural disorder endemic to these materials would smear out any peak.[10]

A second variation on the standard model is the consideration of anharmonic effects, perhaps due to defects or zero-point motion. Hardy and Flocken[25] calculate that $\lambda$ may be increased dramatically if the oxygen atoms vibrate within a double well potential, but such a mechanism will not necessarily suppress the isotope shift $\alpha$. More recent results[26-28] suggest that if the oxygen atoms sit in the appropriate anharmonic potentials, then it is possible to explain both the high $T_c$ and low $\alpha$. Interestingly, in the A-15 materials, the proximity of a structural phase transition appears intimately linked with the relatively high $T_c$'s found in these compounds.[29] Phillips[30] considers a model based on ordered oxygen defects where the defects move so as to optimize $T_c$. Near a maximum of $T_c$, the isotope shift should be nearly zero as seen in $YBa_2Cu_3O_7$. In an additional paper,[31] he has asserted that the small isotope effect arises for the different affinity of as yet undiscovered microdomain walls for $^{16}O$

and $^{18}O$. The existence of the microdomain walls is posited only to occur in $YBa_2Cu_3O_7$. Fisher[32] has commented that the effect of the change in zero point motion on the Cu-O hopping parameter due to isotopic substitution could itself account for the observed shift in $T_c$ in the oxide superconductors.

### 3.45 Non-phonon mechanisms

Many proposed explanations of high-$T_c$ superconductivity[33, 34] explain the experimental results by considering an additional non-phonon-mediated coupling between electrons. These new coupling mechanisms are mediated by electronic excitations (such as plasmons, excitons, magnons etc.) which are independent of isotopic mass and of much higher energy than phonons; therefore, the combination of high $T_c$ and small $\alpha$ can be satisfied easily within these models. The predicted isotope effect has been explicitly calculated for hole-hole interactions,[35] the resonating valence bond model,[36] and charge fluctuation models.[37] However, if one includes the values of the electron-phonon coupling constant determined from infra-red measurements,[38] strict limitations can be made on characteristic energies of these additional mechanisms.[39]

## 3.5 Conclusions

Our results conclusively show that there exists a small but finite oxygen isotope shift in $YBa_2Cu_3O_7$. In samples with $^{18}O$ substituted for $^{16}O$ at approximately 80% of the atomic sites, magnetic measurements indicate a shift $\Delta T_c(\text{bulk}) = -0.17 \pm 0.03K$. dc resistance measurements on similar samples show a transition temperature 1-2K higher than the bulk transition temperature, suggesting that filaments of a distinct material are

present in the samples. The isotope shift for these filaments is $\Delta T_c$ = -0.24 ± 0.02K. After adjusting these values for full oxygen substitution, we find respectively for the bulk and filamentary superconductivity $\alpha_{bulk} = 0.019 \pm 0.004$ and $\alpha_{fil} = 0.028 \pm 0.003$, where $T_c \propto M^{-\alpha}$. These results are within the error limits of several previous $YBa_2Cu_3O_7$ oxygen isotope studies,[1, 2, 6, 7, 40] but are inconsistent with other reports.[3-5]

We find that the small values of $\alpha$ and high $T_c$ reported here can only be explained within the standard three-dimensional phonon-mediated BCS theory if an unphysically large electron-phonon coupling constant $\lambda$ is used. It appears that additional features (such as anisotropy, anharmonicity, or an additional non-phonon interaction) will be necessary to explain superconductivity in $YBa_2Cu_3O_7$.

References

1. L. C. Bourne, M. F. Crommie, A. Zettl, Hans-Conrad zur Loye, S. W. Keller, K. L. Leary, Angelica M. Stacy and Don Morris, Phys. Rev. Lett. **58**, 2337 (1987).

2. B. Batlogg, R. J. Cava, A. Jayaraman, R. B. van Dover, G. A. Koruouklis, S. Sunshine, D. W. Murphy, L. W. Rupp, H. S. Chen, A. White, K. T. Short, A. M. Mujsce and E. A. Rietman, Phys. Rev. Lett. **58**, 2333 (1987); **60**, 754 (1988).

3. Kevin J. Leary, Hans-Conrad zur Loye, Steven W. Keller, Tanya A. Faltens, William K. Ham, James N. Michaels and Angelica M. Stacy, Phys. Rev. Lett. **59**, 1236 (1987).

4. Hans-Conrad zur Loye, Kevin J. Leary, Steven W. Keller, William K. Ham, Tanya A. Faltens, James N. Michaels and Angelica M. Stacy, Science **238**, 1558 (1987).

5. Kevin C. Ott, Robert M. Aikin, Luis Bernardez, Allison Connor, Michael J. Fluss, Eduardo Garcia, Max Goldblatt, William B. Hutchinson, George H. Dwei, Carl J. Maggiore, Joe A. Martin, Robert Meisenheimer, Michael Nastasi, Eric J. Peterson, Eugene J. Peterson, Joseph R. Tesmer, Thomas E. Walker, Jeffrey O. Willis and Pascal J. Yvon, Phys. Rev. **B39**, 4285 (1989).

6. Donald E. Morris, Randy M. Kuroda, Andrea G. Markelz, Janice H. Nickel and John Y. T. Wei, Phys. Rev. **B37**, 5936 (1988).

7. E. L. Benitez, J. J. Lin, S. J. Poon, W. E. Farneth, M. K. Crawford and E. M. McCaron, Phys. Rev. **B38**, 5025 (1988).

8. T. Stoskiewisc, Phys. Status Solidi **A11**, K123 (1972); B. Stratzker and W. Buckel, Z. Phys. **257**, 1 (1972); J. E. Schirber, J. M. Mintz, W. Wall, Solid State Commun. **52**, 832 (1984).

9. M. Cardona, R. Liu, C. Thomsen, W. Kress, E. Schönherr, M. Bauer, L. Genzel and W. König, Solid State Comm. **67**, 789 (1988).

10. W. E. Pickett, H. Krakauer, R. E. Cohen and D. J. Singh, Science **255**, 46 (1992).

11. L. C. Bourne, A. Zettl, T. W. Barbee III and Marvin L. Cohen, Phys. Rev. **B36**, 3990 (1987).

12. Takehiko Hidaka, Toshimi Matsui and Yoshihiko Nakagawa, Jpn. J. Appl. Phys. **27**, L553 (1988).

13. Lin Quan (C. Lin), Wei Yu-nian, Yan Qi-wei, Chen Geng-hua, Zhang-zin, Ning Tai-gang, Ni Yong-ming, Yang Qian-sheng, Liu Chao-xin, Ning Tai-shang, Zaho Jin-Kue, Shao You-yu, Han Shun-hui and Li Jing-yuan, Solid State Commun. **65**, 869 (1988).

14. Z. Fisk, J. D. Thompson, E. Zirngiebl, J. L. Smith and S.-W. Cheong, Solid State Commun. **62**, 743 (1987).

15. P. S. Kobiela, D. Sun, C. B. Prater, W. P. Kirk and D. G. Naugle, in *High Temperature Superconducting Compounds: Processing and Related Properties*, S. H. Whang and A. DasGupta ed., (The Minerals, Metals & Materials Society, 1989), p. 571.

16. Pascal J. Yvon, R. B. Schwartz, C. B. Pierce, L. Bernardez, A. Conners and R. Meisenheimer, Phys. Rev. **B39**, 6690 (1989).

17. J. P. Franck, J. Jung, G. Salomons, W. A. Miner, M. A.-K. Mohamed, J. Chrzanowski, S. Gygax, J. C. Irwin, D. R. Mitchell and G. I. Sproule, Physica **C172**, 90 (1990).

18. M. Grimsditch, T. O Brun, R. Bhadra, B. Dabrowski, D. G. Hinks, J. D. Jorgensen, M. a. Beno, J. Z. Liu, H. B. Schüttler, C. U. Segre, L. Soderholm, B. W. Veal and Ivan K. Schuller, Phys. Rev. Lett. **60**, 752 (1988).

19. Donald E. Morris, Andrea G. Markelz, John Y. T. Wei, Charles T. Hultgren and Janice H. Nickel, Phys. Rev. **B44**, 9556 (1991).

20. G. Bergmann and D. Rainer, Z. Phys. **263**, 59 (1973).

21. G. M. Eliashberg, Zh. Eksp. Teor. Fiz. **38**, 966 (1960).

22. J. Labbe and J. Bok, Europhys. Lett. **3**, 1225 (1987); J. Labbe and J. Friedel, J. Phys (Paris) **27**, 303 (1966); .

23. C. C. Tsuei, D. M. Newns, C. C. Chi and P. C. Pattnaik, Phys. Rev. Lett. **65**, 2724 (1990); however, a recent paper (D. R. Penn and Marvin L. Cohen, Phys. Rev. **B46**, 5466 (1992) ) suggests that $\alpha$ vs $T_c$ cannot be explained solely by singularities in the electronic density of states.

24. D. M. Newns, P. C. Pattnaik and C. C. Tsuei, Phys. Rev. **B43**, 3075 (1991).

25. J. R. Hardy and J. W. Flocken, Phys. Rev. Lett. **60**, 2191 (1988).

26. N. M. Plakida, Europhys. Lett. **4**, 1309 (1987).

27. K. Alex Müller, Z. Phys. **B80**, 193 (1990).

28. Vincent H. Crespi and Marvin L. Cohen, (submitted to Phys. Rev. B).

29. L. R. Testardi, in *Physical Acoustics*, W. P. Mason and R. N. Thurston ed., (Academic, New York, 1973), p. 193.

30. J. C. Phillips, Phys. Rev. Lett. **59**, 1856 (1987).

31. J. C. Phillips, Phys. Rev. Lett. **64**, 1605 (1990).

32. Daniel S. Fisher, A. J. Millis, B. Shraiman and R. N. Bhatt, Phys. Rev. Lett. **61**, 482 (1988).

33. B. Ashauer, W. Lee, D. Rainer and J. Rammer, Physica **B148**, 243 (1987).

34. F. Marsiglio, R. Akis and J. P. carbotte, Solid State Commun. **64**, 905 (1987).

35. J. Kasperczyk and H. Büttner, Solid State Comm. **75**, 105 (1990).

36. D. V. Fil', D. O. Livdan and O. I. Tokar', Physica **C162-164**, 201 (1989).

37. M. Tachiki and S. Takahashi, Phys. Rev. **B39**, 293 (1989).

38. W. Weber and L. F. Mattheiss, Phys. Rev. **B37**, 599 (1988); P. B. Allen, W. E. Pickett and H. Krakauer, Phys. Rev. **B37**, 7482 (1988); .

39. Marvin L. Cohen, David R. Penn and T. W. Barbee III, Solid State Comm. **75**, 971 (1990).

40. E. Garcia, R. R. Ryan, N. N. Sauer, Z. Fisk, B. Pierce, M. Fluss and L. Bernardez, Phys. Rev. **B38**, 2900 (1988).

# Chapter 4: Elastic Properties and Measurement Methods

## 4.1 Introduction

The response of a material to applied stress is quantified by its elastic properties. For isotropic materials — either polycrystalline or single crystal — the response is completely described by any two of the following parameters: Young's modulus (Y), shear modulus (G), bulk modulus (K), or Poisson's ratio (v).[1] For single crystals, the response is described either by the stiffness matrix ($c_{ij}$) or by its inverse, the compliance matrix ($s_{ij}$). A reduced notation, well described in Ref. 1, for stress ($\sigma_i$) and strain ($\varepsilon_i$) allow the reduction of the stiffness and compliance to second rank tensors. The individual elements of the stiffness matrix arise straightforwardly from thermodynamics, i.e.

$$c_{ij} = ( \partial^2 U / \partial\varepsilon_i \partial\varepsilon_j )_T \qquad (4.1)$$

where U is the total energy density of the material and T is the temperature. Obviously, the $c_{ij}$ bear important information about the microscopic interactions between the constituent atoms in the material. Simmons and Wang have compiled and extensive set of elastic constants for crystalline solids.[2] Anomalies in the temperature dependence of $c_{ij}$ can be used to detect phase transitions and relaxation phenomena.[3] The low temperature form of $c_{ij}$ yields important information about the Debye temperature and anharmonicity (non-quadratic terms) in the interatomic potential.[1] Additionally, the $c_{ij}$ may be affected by electric and magnetic fields (electro- and magneto-striction, respectively).[4-6] Because of the variety of energies subsumed in U, complete interpretation of the values and dependencies of the $c_{ij}$ usually requires additional experiments.

Because U arises from the summation of the constituent interatomic potentials, phase changes which alter the microstructure are expected to significantly affect the $c_{ij}$. The symmetry change associated with the phase transition determines which $c_{ij}$ may change.[3] At a first order phase transition, large discontinuities may occur in both $c_{ij}$ and $\partial c_{ij}/\partial T$.[7] At a second order phase transition, a large discontinuity may again occur in $\partial c_{ij}/\partial T$, but a smaller anomaly occurs in $c_{ij}$.[8] From the Maxwell relations, these anomalies are related to the dependence of the transition temperature on stress and to the discontinuities in the specific heat and thermal expansion.[9] For example, second order phase transitions at the Peierls temperature in charge-density wave systems and those associated with the superconducting transition have been investigated by a variety of elastic measurements.[10-12]

U, and its dependence on strain, is substantially affected by the presence of defects within the material.[3] In general, any material at finite temperature contains defects (vacancies, interstitials, dislocations, impurity phases, grain boundaries, etc ). The movement of these defects will affect U and thus $c_{ij}$; the magnitude of the effects depend sensitively on the growth conditions and handling of the sample. These processes, known collectively as relaxation phenomena, cause significant anomalies in the temperature dependence of the $c_{ij}$. Fortunately, it is often possible to distinguish these anomalies from those associated with phase transitions because they should depend on the frequency of the applied stress. (For a good overview of the effect of relaxation phenomena on $c_{ij}$, see Ref. 3.)

The interpretation of changes in elastic constants is simplified by simultaneous measurement of the absorption of strain energy in the sample (attenuation for ultrasonic experiments or damping for vibrating reed experiments). At phase transitions which are coupled to the appropriate strains, both $c_{ij}$ and the damping show critical behavior.[13] Moreover, when the frequency of the applied stress equals the characteristic frequency of a particular relaxation phenomena, a maximum occurs in the damping.[3]

The remainder of this chapter describes various experimental techniques for measuring the elastic properties. Sect. 4.2 provides an overview of experimental techniques. Sect. 4.3 examines vibrating reed techniques in more detail and Sect. 4.4 describes the particular experimental configuration chosen to provide the best trade-off between precision and experimental ease. Sect. 4.5 catalogues a variety of experimental 'tricks.'

## 4.2 Methods of measuring elastic properties

### 4.21 Overview

Because of the importance of elastic properties, many experimental methods have been developed for their investigation. A list of methods compiled from published results on the high-temperature superconductors (HTSC's) and charge-density wave (CDW) materials follows: (i) *uniaxial tensile test* in which the sample strain and thus the Young's modulus are determined directly from the elongation under an applied stress;[14, 15] (ii) *vibrating reed technique* in which the elastic properties are inferred from the resonant frequencies for various

macroscopic modes of oscillation;[16, 17] (iii) *acoustic or ultrasonic techniques* in which the sound wave velocity is determined for a variety of different polarizations and propagation directions;[18-20] (iv) *electron diffraction studies* in which changes in the unit cell dimensions are measured as functions of applied stress;[21] (v) *Brillouin scattering* in which the energy (E) of acoustic phonons as a function of wavevector (k) is found by determining the Raman shift caused by these phonons;[22] and (vi) *inelastic neutron scattering* in which the complete E vs k diagrams can be determined for both acoustic and optical phonons.[23] There are also a variety of methods which have been developed to measure the elastic properties of thin-films; examples are surface acoustic waves[24] and ultrasonic oscillators.[25]

These methods vary widely as to complexity, cost, accuracy, required sample dimensions and sensitivity to changes in the elastic constants. Ultrasonic techniques have been used most extensively in studying the HTSC's and Sect. 4.22 describes them more fully. For the experiments discussed in this thesis, the vibrating reed technique, described fully in Sect. 4.3, provides the best sensitivity for the available samples.

**4.22 Ultrasonic techniques**

In the most straightforward ultrasonic techniques, sound waves with a particular polarization (i.e longitudinal or transverse) are produced by a piezo-electric and introduced into the sample. The wave velocity, $v_{ij}$, is directly related to $c_{ij}$, ($v_{ij} = \sqrt{c_{ij}/\rho}$ where $\rho$ is the density and i and j refer to the direction of propagation and polarization relative to the crystal axes).[18] $v_{ij}$ is determined by detecting the sound pulse with an additional piezo-electric and measuring the transit time across the sample or for any

numbers of reflections. The damping for that mode of vibration is determined by measuring the signal decay with number of reflections. Additional sensitivity to small changes in the elastic constant (to ~ 10 ppm) can be gained by operating in a resonant condition in which integral number of wavelengths occur within the sample. Recently, Migliori *et al.*[26, 27] have introduced a method in which the complete elastic constants for a particular material are determined from a large set of sample resonant frequencies for nearly free vibration; this method, however, requires extensive computer time and particular sample geometry.

The sensitivity and the relatively low cost of the required equipment make ultrasonic methods attractive. The drawbacks arise from the requirements for sample geometry and for coupling of the sound wave into the sample (usually achieved with vacuum grease). In general, for satisfactory results, the sample must be cylindrical with faces perpendicular to the cylinder axis and large enough ( ~ 1 $mm^2$ on a face) for good coupling of the crystal to the transducers. Though $YBa_2Cu_3O_7$ and $La_{2-x}Sr_xCuO_4$ crystals can be grown with the appropriate shape, proper crystals of other HTSC's do not yet exist. The CDW compounds have one or two dimensional crystal morphologies which make ultrasonic measurements difficult. In one experiment, Jericho and Simpson[28] coupled ultrasonic longitudinal waves into thin $TaS_3$ crystals by mounting one of the transducers on a crossed wire suspension.

## 4.3 Vibrating reed method

### 4.31 Background

There are several measurement techniques subsumed under the heading "vibrating reed." Each uses macroscopic movements of the sample to determine the material's elastic properties; these movements are often either simple bending or twisting of the whole sample. Bending a beamlike sample, parallel to the sample width, t, as shown in Fig. 4-1, produces stresses parallel to the sample length L, with one side of the sample in compression and the other in tension. The resonant frequencies ($f_n$) for bending when one sample end is rigidly clamped and the other is free to vibrate, "clamped-free" configuration,(see Fig. 4-1) are directly related to the Young's modulus (Y) for uniaxial stress applied parallel to L, i.e.

$$f_n = (\alpha_n t/L^2)\,(Y/\rho)^{1/2} \tag{4.2}$$

where $\alpha_n$ is a constant dependent on the particular flexural mode ($\alpha_n$ = 0.1615, 1.0123, 2.8346, and 5.5622 for the fundamental and first three harmonics, respectively), t is the thickness parallel to the direction of vibration, and $\rho$ is the density.[29] If a load of mass M is attached to the free end of the reed, then

$$f_0 \equiv (1/2\pi)\,[Ywt^3 / 4L^3(M + 0.2357m_s)]^{1/2} \tag{4.3}$$

where w is the sample width perpendicular to the direction of vibration, $m_s$ is the weight of the sample, and $M \geq m_s$.[3]

For measurements of the shear modulus (G), a large mass (flag) is usually attached to the sample to excite and detect twisting deformations.

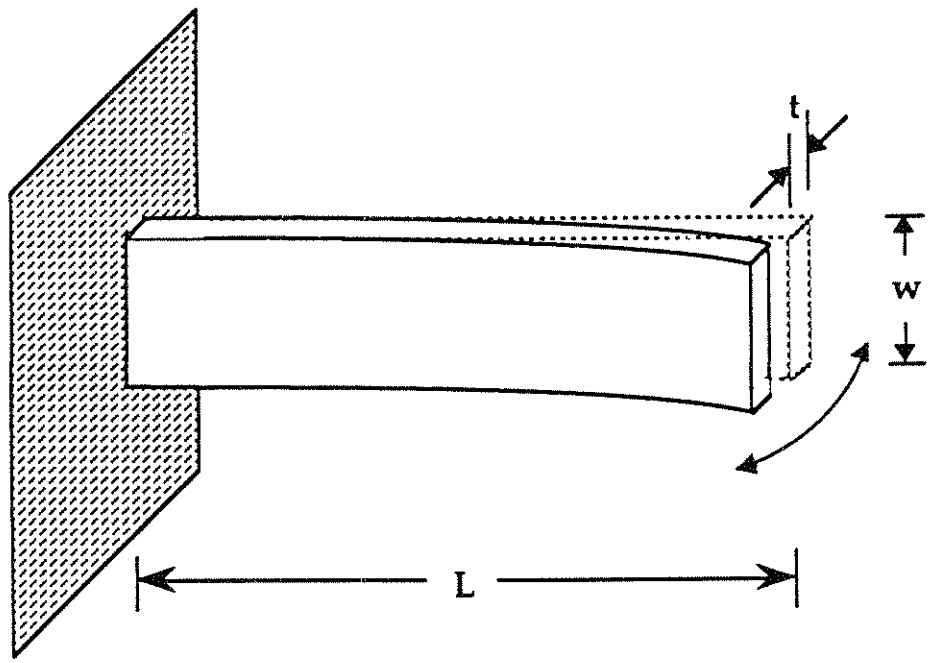


Fig. 4-1. Clamped-free oscillations of a rectangular beam

Similar to bending experiments,

$$f_o = k\sqrt{G} \tag{4.4}$$

where $k_g$ depends on sample and flag geometry.[30]

Y and G are directly related to the $c_{ij}$ and depend on the direction of the crystal axes within the sample. The above relationships assume that the sample is thin, i.e. t<<L. In general, this condition on sample geometry must obtain for vibrating reed to be practical. The resonant frequencies often occur at kHz frequencies for which there are a variety of inexpensive excitation, detection, and signal processing techniques. The particular strength of the vibrating reed method is its sensitivity to small changes in the appropriate elastic constant (~ppm). Indeed, it has been especially important in determining the effects of temperature, magnetic and electric fields on the elastic constants. Because the resonant frequency depends sensitively on sample dimensions, this method yields only an estimate of the absolute magnitude of Y and G. The frequency dependence of the vibration amplitude of the reed is that of a harmonic oscillator and the displacement of any portion of the reed has components both in phase ($X_i$) and out of phase ($X_o$) with the driving force.

$$X_i = \frac{(f_o^2 - f^2)\,A}{(f_o^2 - f^2)^2 + (\delta f_o^2)^2}. \tag{4.5}$$

$$X_o = \frac{\delta f_o^2\,A}{(f_o^2 - f^2)^2 + (\delta f_o^2)^2}. \tag{4.6}$$

$\delta$ is the damping of the resonance ($\delta = 1/Q$) and A depends on the position along the reed and the magnitude of the driving force. Fig. 4-2 plots both $X_i$ and $X_o$ as functions of frequency.

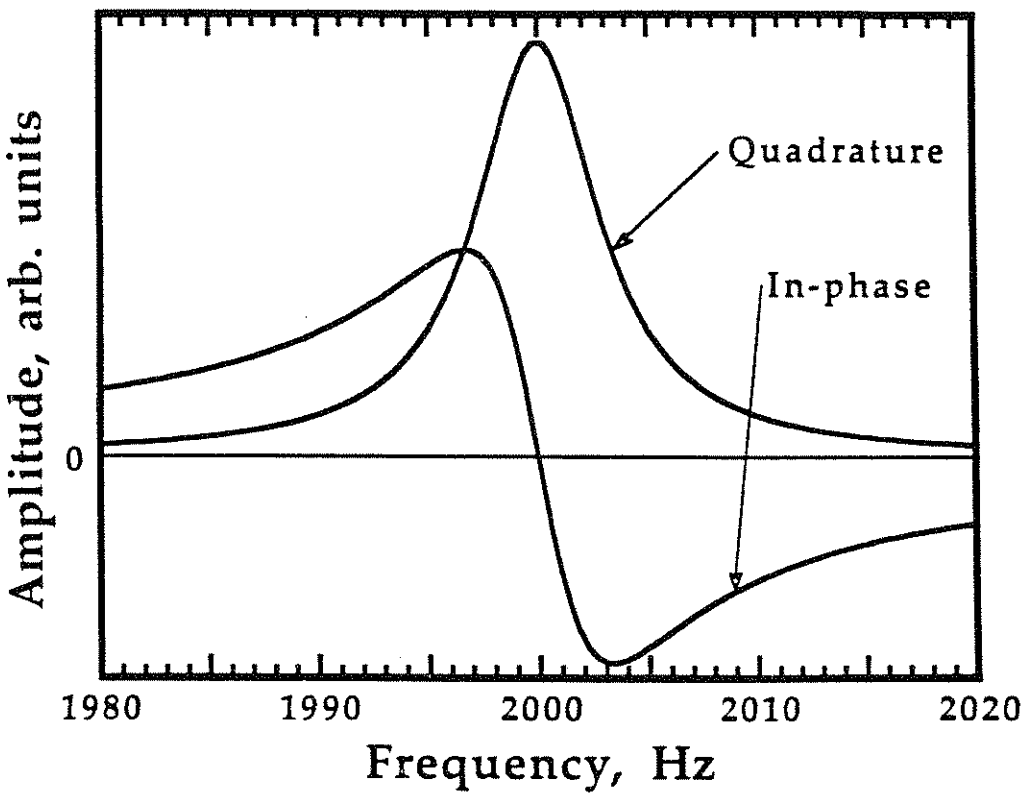


Fig. 4-2. Quadrature and in-phase response, relative to the driving excitation, as functions of frequency for a vibrating reed (resonant frequency, $f_o$ = 2000 Hz and $\delta = 1/Q = 3.3 \times 10^{-3}$).

### 4.32 Clamping conditions

For vibrating reed, the various techniques can be subdivided by methods for clamping, excitation and detection. The appropriate choice for each of these depends on the properties to be investigated, the available electronics, and the sensitivity desired. When working with the HTSC's or CDW materials, the chosen clamping conditions are usually either fixed-free (as shown in Fig. 4-1), fixed-fixed, or fixed-inertially clamped. Inertial clamping refers to the use of a large load mass at one end of the sample which induces a node but does not rigidly clamp this end.[31] The latter two are used when current is passed through the sample and for both, unfortunately, changes in the clamping apparatus can significantly affect the resonant frequency. Fixed-fixed is especially difficult to use when temperature varies because even small differences in thermal expansion can cause large sample stresses. A temperature compensated apparatus with a bimorph as one of the clamps mitigates some of these effects.[32]

### 4.33 Excitation methods

The excitation technique must apply forces or torques in such a way to excite the desired mode of vibration. The two most common methods are (i) electrostatic attraction and (ii) piezo-electric movement. For (i), a drive lead is positioned close to the sample (~25μm) and charged.[16] If the sample is an effective ground plane, then it collects the opposite charge and experiences and attractive force to the lead. The benefits of this method are that it is compact and the force on the sample is at twice the drive frequency so crosstalk on ground planes and pick-ups is reduced. The drawbacks are the following: the need to position the lead close to the

sample, which for fragile samples is a perilous task; the mechanical resonances of the drive lead may be confused with those of the sample; and large voltages (>100V) needed to produce significant sample movements require special handling. For (ii), piezo-electric movement, the "fixed" end of the sample is affixed to a piezo-electric mount (either a simple piezo-electric[33] or a bimorph[32]). When voltages are applied across the piezo-electric, small displacements (~Å) are induced at the sample. The benefits of this method are that the effective force occurs at the sample boundary so many flexural modes can be excited and that no delicate positioning is required. The drawbacks are that the piezo-electric has an extremely large dielectric constant (~$10^4$) and can interfere with nearby rf signals and that it draws substantial current even at low drive voltages (10V) and frequencies (kHz) which may produce spurious signals on adjacent leads. In general, the benefits of the piezo-electric make it the appropriate excitation method for most circumstances.

**4.34 Detection techniques**

A detection technique must be sensitive to small displacements (≤100Å) of one portion of the sample. There are many methods for detecting small movements, yet not all have been incorporated into vibrating reed. For example, optical deflection[34] or interference[35, 36] methods provide excellent sensitivity; however, this method has not found widespread use because of the difficulties of coupling light onto the sample and of canceling out extraneous optical path variations. Three detection techniques are commonly used; (i) dc capacitance,[16] (ii) rf capacitance,[17] and (iii) helical resonator.[32] For (i), the sample acts a one plate of a capacitor as shown in Fig. 4-3a. Movements of the sample

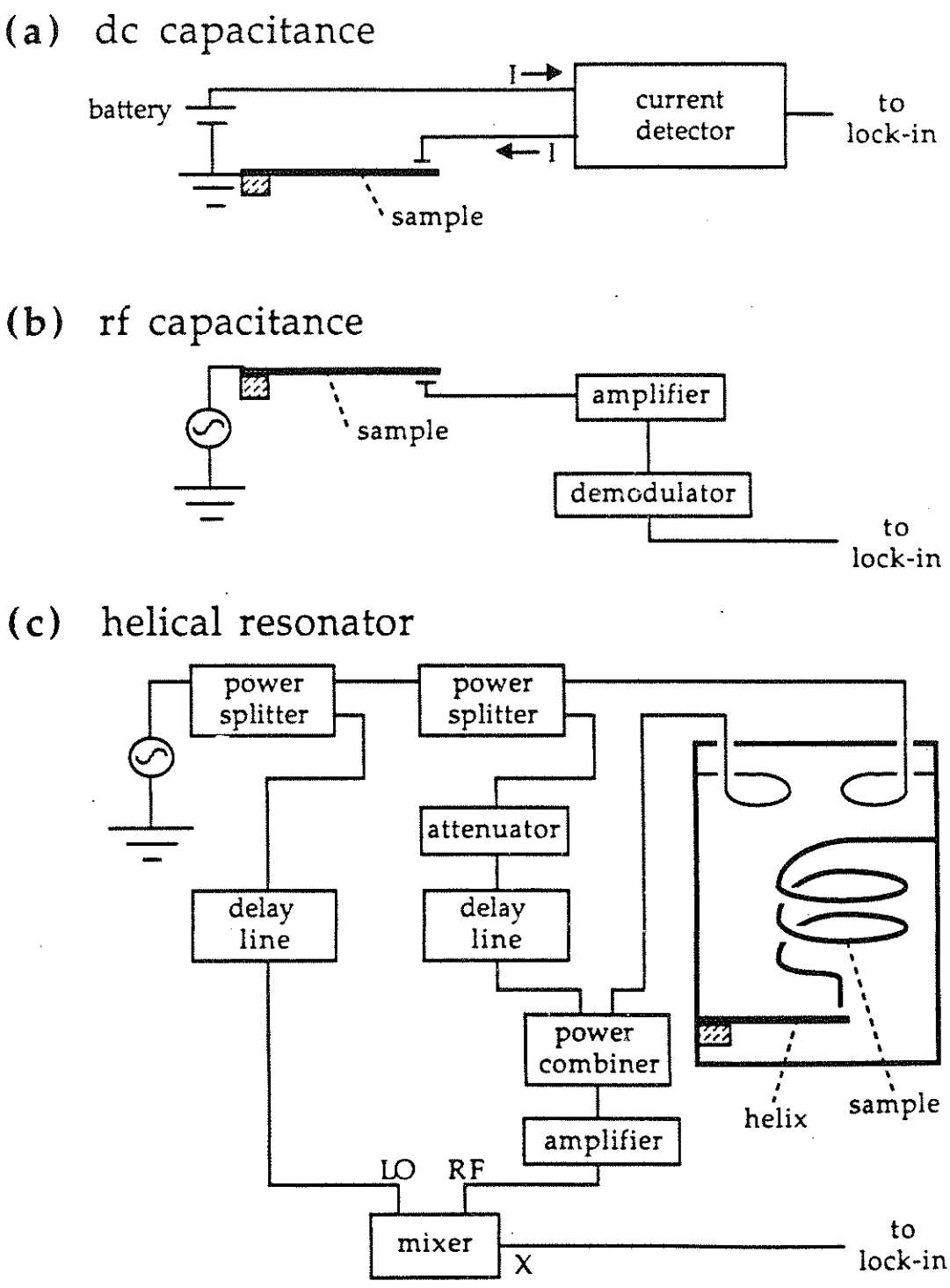


Fig. 4-3. Electrical schematics for three methods of detecting sample deflections in the vibrating reed technique.

change the plate spacing and the effective capacitance. A large voltage (~150V) is maintained between the sample, which acts as an effective ground, and the pick-up lead. Movements of the sample cause current to flow into the pick-up which is detected by a sensitive ammeter in series with the applied voltage. For (ii), rf capacitance, an rf signal (~300MHz) is fed into the clamped end of the sample, as shown in Fig. 4-3b. A pick-up electrode is positioned ~50μm from the desired portion of the sample. Movements of the sample change the coupling to the pick-up and produce an envelope on the rf signal (see Fig. 4-5a). This signal is then amplified and demodulated with either a diode detector (power meter) or a mixer. The diode detector, being a two terminal device is easier to use; however, most diode detectors lose sensitivity at high frequencies (>20 kHz). For (iii), helical resonator, rf signal modulation is again used to detect sample movement, but in this case, the sample acts as a ground plane in an rf cavity, as depicted in Fig. 4-3c. The helix in the center of the cavity reduces the cavity resonance ($f_o$) from ~10GHz to ~400 MHz but maintains a high Q ($\equiv f_o$/FWHM where FWHM = full-width at half maximum). The cavity and helix parameters may be chosen to yield an unloaded Q of ~ 1000 without expensive plating techniques. $f_o$ is extremely sensitive to the termination conditions at the free end of the helix. Movements of the sample are capacitively coupled to the helix and alter $f_o$. Changes in $f_o$ can be detected with a variety of mixing techniques. Fig. 4-3c depicts a schematic diagram both of the helical resonator and an example of one such mixing technique.

### 4.35 Sensitivity analysis

The sensitivity of each of these methods can be increased by using a dummy in parallel to the actual sample. By subtracting the dummy signal from the actual signal, spurious effects arising from variations in the external circuitry may be minimized.

Many factors determine which detector technique is appropriate for a particular experiment; a significant concern is the sensitivity to sample displacements. Careful construction of the vibrating reed apparatus is needed to ensure that the movements of the stray leads are not the dominant noise source. As carefully described by X. D. Xiang,[13, 32] the sensitivity is ultimately limited by the Johnson noise of the detection apparatus. The minimum detectable displacement ($\Delta d_{min}$) is then written as

$$\Delta d_{min} = (C/C_o)\,(4k_BTBR_d)^{1/2} / (V_{max}/d_o) \qquad (4.7)$$

where C is the capacitance between sample and pick-up lead, $C_o$ is the stray capacitance in the detection circuit, $k_B$ is Boltzmann's constant, B and $R_d$ are the bandwidth and input impedance, respectively, of the detection apparatus, $d_o$ is the distance between the sample and pick-up lead, and $V_{max}$ is the maximum voltage which may be applied. $V_{max}$ must be less than the vacuum breakdown voltage between the sample and pick-up leads ($V_{max}/d_o < 10^5 V/cm$), but a more restrictive bound arises because it is undesirable for $V_{max}$ to affect the sample vibration. This bound depends on the sample dimensions and Young's modulus, but for small thin samples (~ 1.00 x 0.02 x 0.02 $mm^3$), $V_{max} \sim 10^3$ V/cm.[13] For dc and rf capacitance methods, only $R_d$ varies with $R_d(dc) \sim 10^{10}\Omega$ and $R_d(rf) \sim 10^4\Omega$.

$C/C_o \sim 10 - 100$. Therefore, for the rf capacitance method, $\Delta d_{min} \sim 10^{-2}$ Å $\sqrt{B}/Hz$.[13]

The analysis for the helical resonator is more subtle.[32] The effective Johnson noise is decreased from that for the dc and rf capacitance methods and there is a net signal to noise gain proportional to $Q_u$, the unloaded Q of the cavity. Xiang *et al.* have achieved sensitivities of $1.4 \times 10^{-4}$ Å $\sqrt{B}/Hz$.[32]

For many vibrating reed experiments, that extreme sensitivity is unneeded and other concerns — such as ease in handling the sample, experimental turn-around time, and availability of computer interfacing — must be considered. At present, it is difficult to connect the helical resonator to the computer for temperature dependent studies. As temperature changes the phase change along the resonator arm of the circuit changes and delay lines must be adjusted mechanically. An electronic phase shifter may ameliorate this difficulty.

### 4.4 Particular vibrating reed design

This section describes in detail the vibrating reed apparatus and external circuitry found to be the best trade-off between sensitivity and experimental ease. This particular apparatus uses a piezo-electric drive and rf detection and can be attached to a variety of proves for submersion in liquid helium or positioning in a superconducting magnet. The remainder of this section is divided as follows: 4.41 Description of apparatus and design considerations; 4.42 Signal processing electronics; and 4.43 Automated data acquisition.

### 4.41 Description of apparatus and design considerations

The apparatus, shown as an exploded schematic in Fig. 4-4, is designed to be attached to a multipurpose probe which has a coax center conductor connected to the central pin. This design can be readily modified to allow different connections to the rf input signal. This rf signal is routed with #28 gauge wire to a gold plate the piezo-electric assembly and then to the gold plate on which the sample is affixed with silver paint (Dupont Conductor composition 4929N). The signal is capacitively coupled through the sample and a small gap to #30 gauge copper pick-up lead which is connected to the center pin of a second semi-rigid coax cable. The $Al_2O_3$ spacer plays the crucial role of decoupling the rf signal from the piezo-electric. For frequencies less than several GHz, the dielectric constant of the piezo-electric is huge (>2000) and the spacer ensures that it does not shunt the rf signal coming to the sample.

The insulated pick-up lead is affixed to the aluminum leaf spring which is rigidly attached to pickup-mount (a) and the fine adjust screw in pick-up mount (b) allows the pick-up wire to be accurately positioned close to the sample (5-25 μm). This design accommodates many different sample lengths and reduces the chance of damaging the sample when positioning the pick-up. Because "coarse" adjustments are made by bending the pick-up, some delicate handling is still required. The need for flexibility in the pick-up also precludes the possibility of shielding it from extraneous rf signals.

The piezo-electric used in this apparatus (0.10" x 0.10" x 0.40"; Stavely-EBL Division, lead zirconate Navy Channel 5a) provides ~10Å/V movement at its free end. To reduce extraneous vibrations and

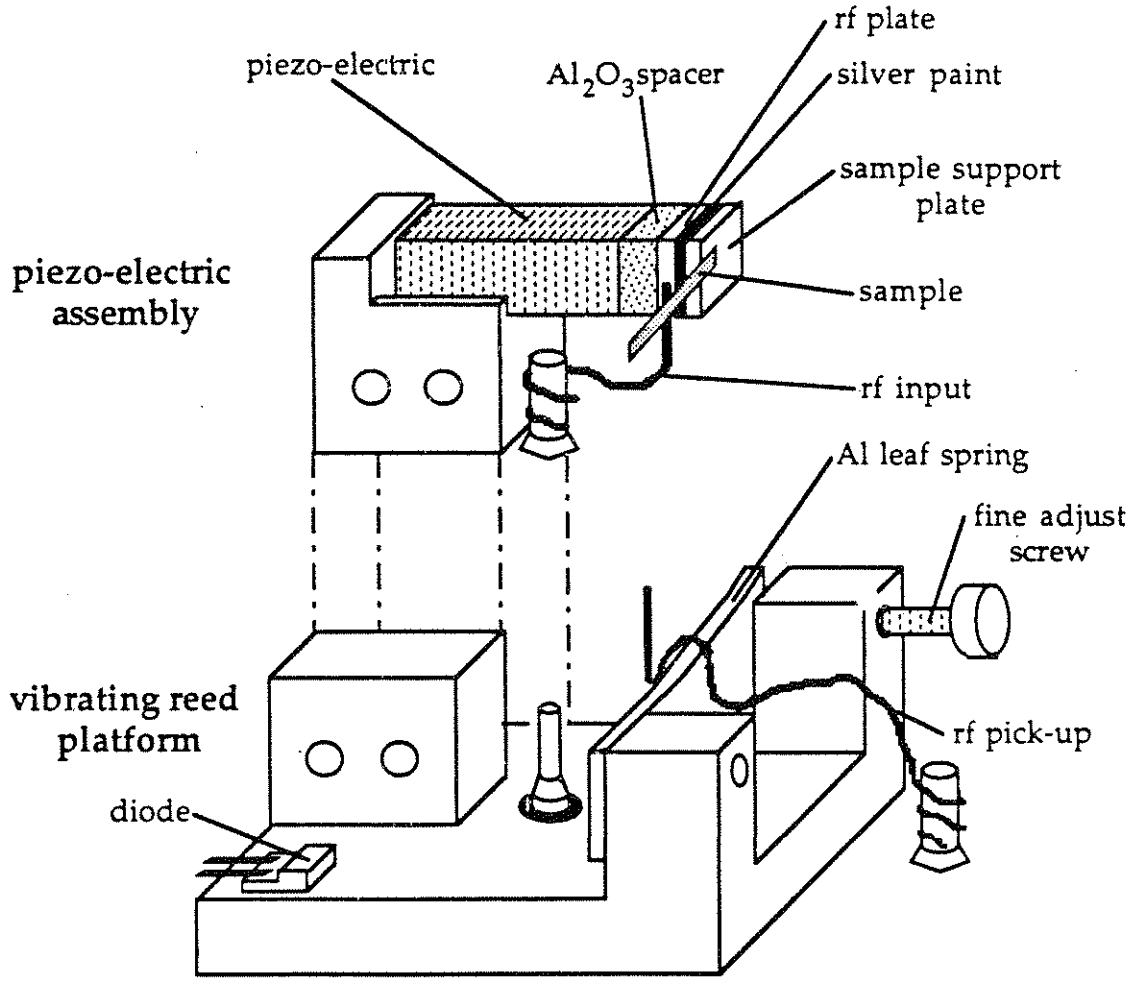


Fig. 4-4. Exploded schematic of vibrating reed apparatus. The scale is approximately 4"=1" and the dashed lines show where the piezo-electric assembly inserts on the vibrating reed platform.

resonances, it is crucial that the piezo-electric be rigidly clamped. As shown in Fig. 4-3, the piezo-electric sits in a 0.075" slot in the copper holder and is firmly affixed with stycast. (The nickel electrode has been removed from this portion of the piezo-electric.) The copper support is then clamped to the base with two 0-80 screws. Even at low frequencies and voltages, the piezo-electric draws substantial currents (~100 mA) and a shielded twisted pair is needed to minimize inductive crosstalk with other leads (especially the diode leads). In general, piezo-electrics show marked temperature dependence in their constrictive and dielectric constants. Fortunately, the vibrating reed method does not require an absolute calibration of the forcing vibration. The sample damping, though roughly inversely proportional to the amplitude of the resonance, can be more accurately determined from Q. Using both optical and capacitive means, the bimorph motion was found to be reduced from its room temperature value by ~60% at 77K.

The temperature sensor (Lakeshore 471-SD) provides good sensitivity over the temperature range (4.2-300K). In two studies, one using a second diode and another with a differential thermocouple, the sample and diode temperature were confirmed to be within 2K with no helium exchange gas and under rapid heating and cooling conditions. With an exchange gas (~1 torr of helium) and slow temperature changes, their respective temperatures agreed to ±0.25K. A clamping capacitor (~2μfd) between the two diode leads removes stray signals induced by the bimorph and rf drives.

### 4.42 Analog detection electronics

Sample movements cause the rf signal at the pick-up to be amplitude modulated as shown in Fig. 4-5a. The simplest method for detecting this modulation, shown schematically in Fig. 4-5b, uses a diode (HP11096) to detect the signal power. Unfortunately, such diode detectors usually have a limited bandwidth and will not detect envelope modulations at frequencies greater than 20kHz. A frequency mixer provides the easiest means of detecting modulations for higher frequencies. Shown schematically in Fig. 4-5c, the original drive signal is mixed with the detected signal to determine the additional sidebands present in the detected signal. The choice of the appropriate mixer can be difficult. Some useful comments are contained in Ref. 37. For this circuit, the appropriate mixer is roughly determined by the maximum output power of the frequency synthesizer (1.5V rms or ~16dbm) and the frequency range of interest (dc - 1000 MHz). A Level 7 mixer, such as an HP 10514A, requiring 7 dbm reference signal at the LO port, satisfies the design constraints. A Level 10 mixer with suitable frequency response could also be used. The mixer adds some additional subtlety to the circuit since the appropriate power level and phase of the input signals (LO,RF) must be maintained.

A lockin amplifier (EG&G5407) detects the in-phase and quadrature components of the demodulated signal at the piezo-electric drive frequency. Near a sample resonance, the outputs of the lockin — if it is in the X-Y mode — appear similar to those shown in Fig. 4-2. Unless there are additional resonances present or some non-linearity in the motion of the sample, adjusting the phase of the lockin can make the signal appear

(a) modulated rf signal

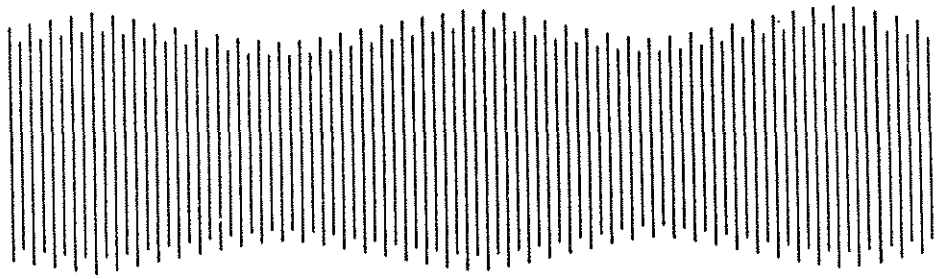

(b) diode detector

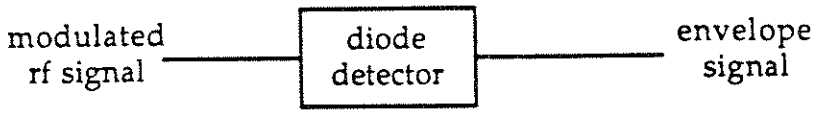


(c) rf mixer

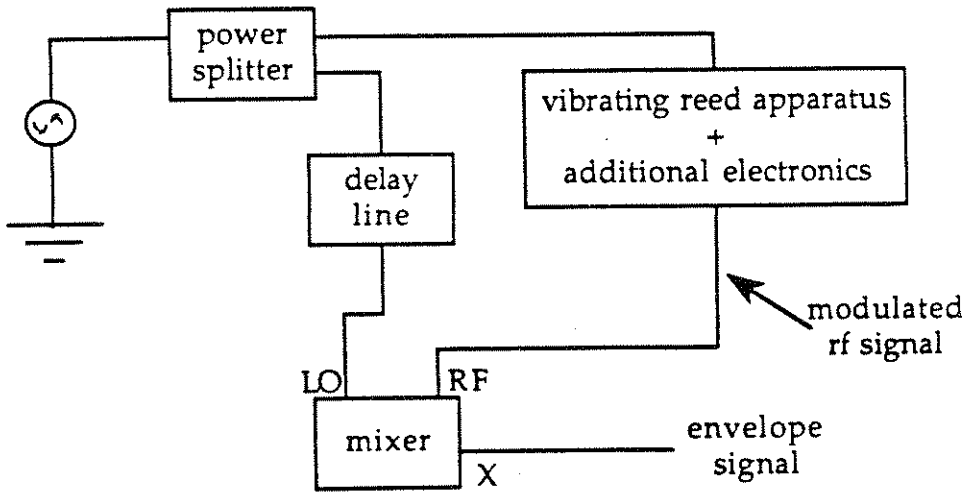


Fig. 4-5. Schematic of two rf demodulation techniques (b,c) for a modulated rf signal (a), with typical carrier frequency ~400 MHz and modulation frequency ~kHz.

exactly as shown in Fig. 4-2. The resonant frequency is determined either by the zero crossing of the in-phase or by the peak position of the quadrature. The former provides a more sensitive probe of the resonant frequency and thus Young's modulus.

Many previous experiments have followed the resonant frequency by operating in a phase-locked configuration; i.e. the in-phase output of the lockin is connected to the voltage controlled output (VCO) port of the piezo-electric drive. If the resonant frequency shifts, then the non-zero in-phase signal will cause the frequency of the drive to shift commensurately. This method, while convenient, reduces the sensitivity of the circuit because the frequency stability is no longer determined by the synthesizer, which may be as stable as 1 part in $10^8$ per hour, but is determined by the lock-in and extraneous line noise. The computer controlled configuration described below provides the possibility of greater sensitivity.

**4.43 Computer assisted data acquisition**

An HP9000-216 computer connects to the analog circuit, depicted in Fig. 4-6, to monitor and control the system and to store the data along with pertinent system parameters. Voltmeters with HPIB (HP interface bus) ports are connected to the diode and lockin $X_i$ and $X_o$ output ports. The computer directly controls the HP3325B frequency synthesizer.

The tree-structured program, DIO_FSCAN, has two distinct data taking routines; "measure_fscan" which measures the outputs of the lockin $X_i$ and $X_o$ ports as functions of frequency (i.e. it produces curves similar to that shown in Fig. 4-2) and "measure_fstep" which tracks and records the resonant frequency and quadrature output as functions of temperature. For either routine, the user must enter a set of parameters

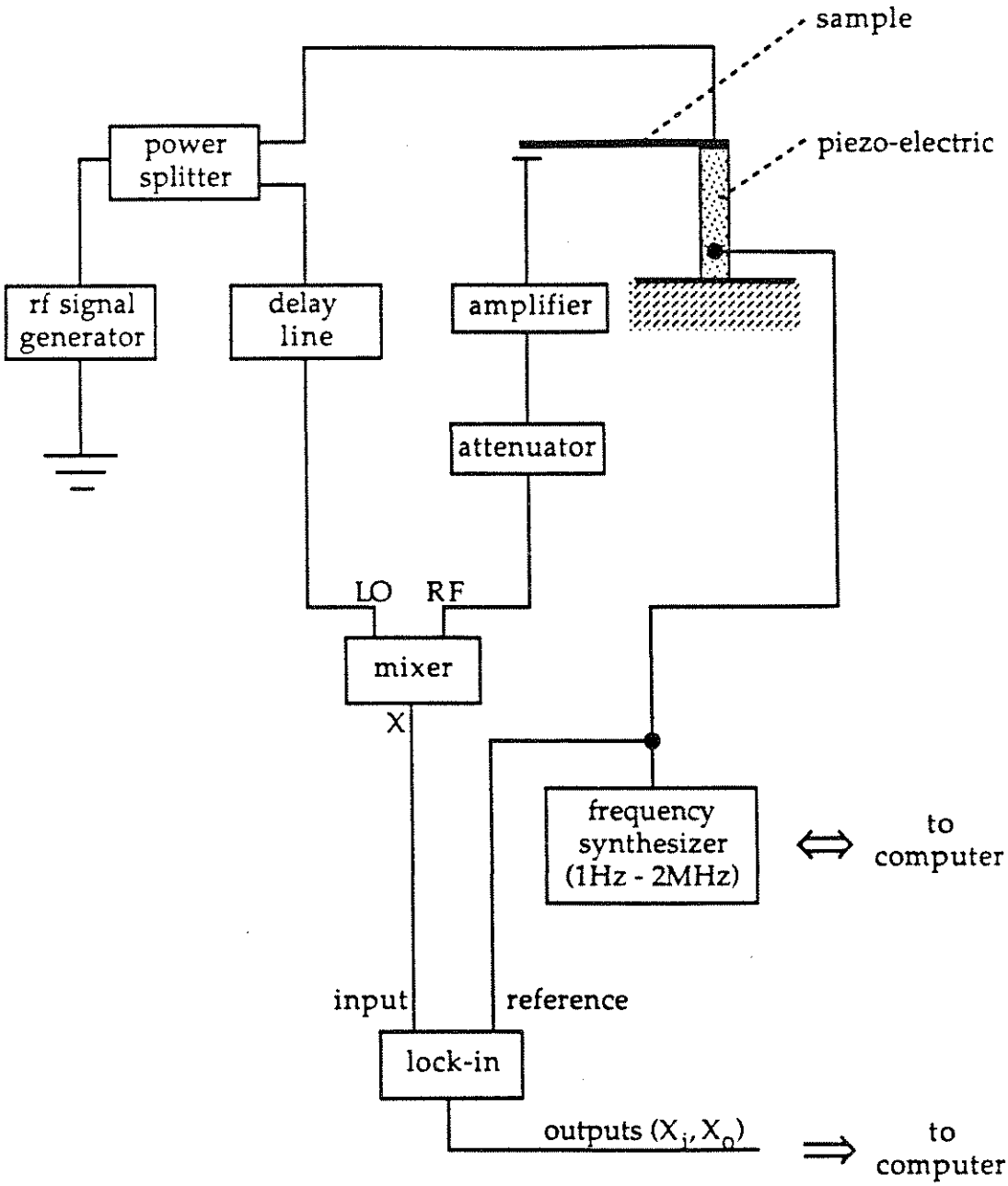


Fig. 4-6. Schematic diagram of vibrating reed analog electronics. On the mixer, LO, RF and X denote the local oscillator, input, and output ports, respectively. (The particular devices used are as follows: rf signal generator: HP8656A, power splitter: Mini-Circuits ZSC-2-4, delay line: General Radio Co. 874-LK20, amplifier: Avantek GPM-1052, attenuator: Kay 5150, mixer: HP10514A, frequency synthesizer: HP 3325B, lock-in: EG&G 5407.)

"exp_param" which describe the configuration of devices to which the computer is connected and assist the computer in tracking and determining the resonant frequency. ( The "information" subroutine in the main menu contains a description of each of these parameters.) During the experiment, the experimental parameters can be changed and each set is stored as one "mode" of the experiment. When the sample data is stored, it is linked with the appropriate mode.

The subtleties of the computer program lie in the temperature subroutine, "measure_fstep;" here, at temperature intervals set by the user, the computer determines the zero-crossing of the in-phase signal by taking three data points which straddle the resonant frequency. The computer continues to search until a zero-crossing is found by increasing (decreasing) frequency if the in-phase is positive (negative). The frequency increment, "f_step for zero X," and time delay, "tau_data," between data points are both set by the user and depend on the time delays of the lockin, the Q of the resonance, how rapidly the resonant frequency changes, and how accurately it should be determined. A rule of thumb is that the sensitivity is ~ 1/20 the step frequency and that tau_data should be five times the time delay of the in-phase signal (unless the program is operated in the "follow" mode — see below). When the zero crossing is found, the computer also stores the maximum of the three corresponding quadrature signals as the resonance amplitude. The search for the resonant frequency is accelerated by choosing the "follow" mode which uses the sign of the expected slope of f(T), as entered by the user, and the in-phase output to follow the resonant frequency. Basically, the system acts as a phase locked

loop which maintains the frequency stability of the synthesizer. In this mode, "tau_data" may be 1.5-2 times the in-phase time delay.

In the "measure_fstep" routine, the user may also choose to perform a "q_check" which will fit a Lorentzian to the quadrature and determine both Q and the approximate resonant frequency. Three points are first taken at the top of the Lorentzian and are used to estimate what frequencies would lie roughly half-way down either side of the Lorentzian. The frequency step used here is three times "f_step for zero X," but the user may choose to modify it to properly map out the Lorentzian. The quadrature values of these five points are then best fit. Determining Q takes considerably longer than simply finding the resonant frequency and the sample temperature should be stabilized (<0.5K/min). Over small temperature intervals (10-20K), the resonance amplitude tracks Q, but over large intervals, the proportionality does not hold because the amplitude of the piezo-electric motion, the amount of rf signal transmitted through the sample, and the distance between the sample and pick-up may all change with temperature. Checking Q every 10K or 20K determines the relationship between Q and resonance amplitude. If the program should become "hung" during data gathering, it can be safely "paused" and restarted. The data are stored in COMMON statements which ensures that they aren't erased if the program is restarted.

Computer assisted data acquisition makes vibrating reed experiments much more convenient. Interpreting vibrating reed data involves being aware of features on both small and large scales. Moreover, programs such as NEW_PLOT allow the following data manipulations: removing a slowly varying (either linear or quadratic) background from the data,

subtracting two data sets, or performing simple mathematical manipulations. For more complex analysis and graphical manipulation, it is usually worthwhile to transport the data to an Apple®.

### 4.5 Experimental tricks

This section describes a collection of experimental tricks which the new user of this vibrating reed apparatus may find helpful; it covers (i) handling of small, fragile, samples, and (ii) searching for a resonance.

The vibrating reed apparatus was designed to facilitate the handling and testing of fragile samples; in particular, it is possible to remove samples and reuse them later. A sample mount is first prepared by cutting 10 mil gold foil to the approximate size of the end of the piezo-electric assembly. This square is then weakly affixed to a slide with silver paint, and a second square is bought within ~3/4 of the expected sample length, as shown in Fig. 4-7a. The sample is maneuvered (Fig. 4-7b) onto the two squares by delicate use of forceps or sharpened wooden stick.[38] By positioning the wooden stick under the middle of the sample, the sample can be placed touching both gold squares and the wooden stick withdrawn through the intervening space. Thinned silver paint is then wicked along the top of the sample mount without the "paint brush" approaching the sample. Once the sample is rigidly held by the paint, the additional square is removed and thicker silver paint applied. After this second coat of paint has dried, the piezo-electric assembly (Fig. 4-4) is placed nearby on double sided tape so that the gold rf plate faces up. A coat of silver paint is then applied to this surface. The sample mount with the attached sample is removed from the slide by placing a scalpel underneath the mount and

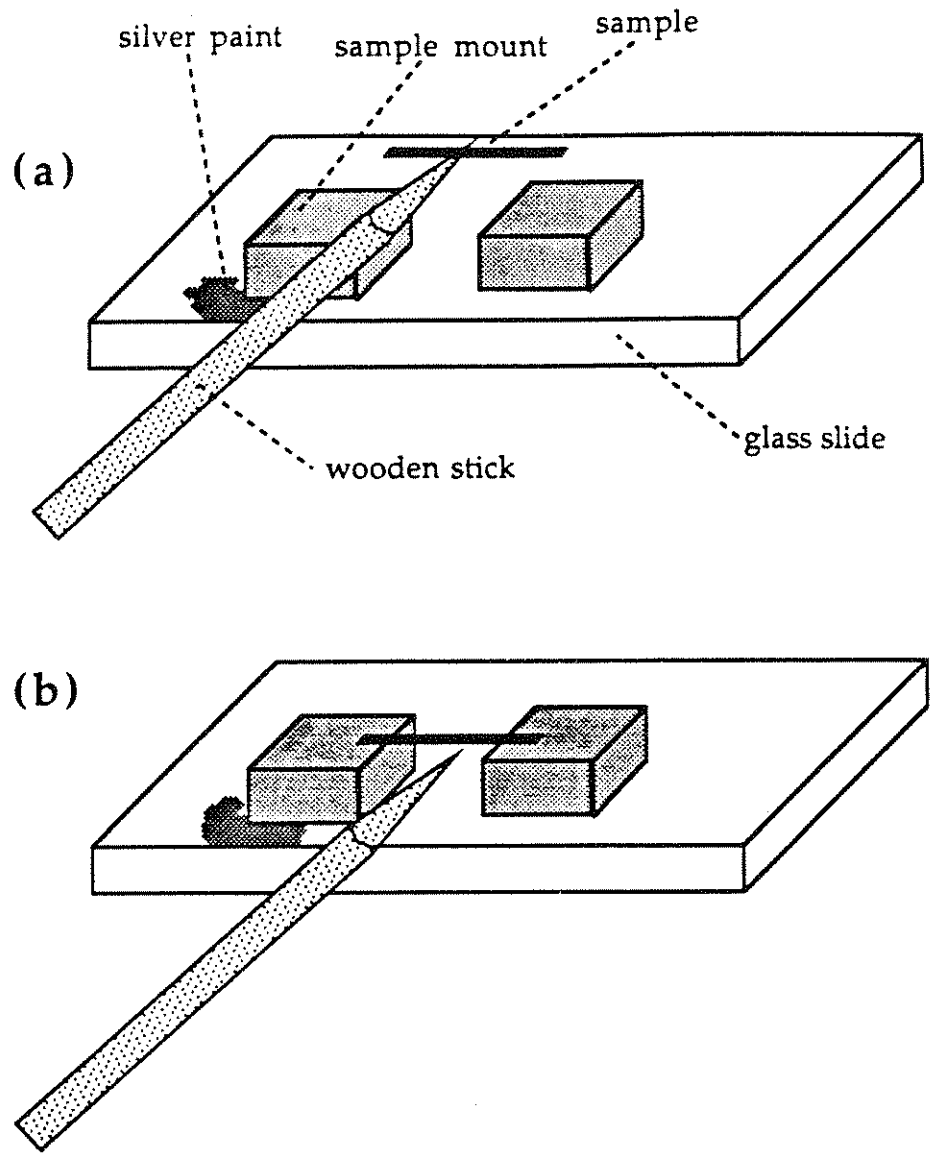


Fig. 4-7. Schematic for handling of delicate beam-like samples (a) for sample adhering to sharpened wooden stick by electrostatic attraction and (b) for sample transferred to sample mount and second Au square.

prying it into the jaws of a delicate pair of forceps. The sample mount is now placed on the piezo-electric assembly and carefully pressed into the rf plate to remove excess silver paint. By placing the assembly under a heat lamp, the silver paint dries within 20 minutes. The assembly is removed from the double-sided tape and, firmly held by heavy forceps at the rf connector, moved to the probe. The pick-up lead should be completely bent away from the sample and the leaf spring fully retracted. Sliding the rf connector over the rf pin in the base roughly secures the assembly. Two 0-80 screws then rigidly clamp it into place.

When bending the pick-up lead to within ~200μm of the sample, one must be aware of its substantial "springiness" and not allow it the strike the sample. The effects of its elasticity are reduced by working under a microscope and by first pulling the lead past the desired position. The forceps must be opened slowly to allow the lead to reach its relaxed position without overshoot.

When the sample and pick-up leak are in place, the piezo-electric drive and rf detection circuits are connected as shown in Fig. 4-6. A quick check of whether the piezo-electric is correctly connected is to listen for the piezo-electric movements at ~12kHz and 10V drive. In this range, its movements should be audible. The power of the reference rf signal is set at a level appropriate for the mixer (probably ~ 10dbm) and its phase should be adjusted with the delay line to yield the largest signal out of the mixer (as checked by a dc voltmeter). By choosing the correct amplifier and attenuator, the size of the detected input to the mixer is adjusted to be at least 7 db below the reference (checked with diode detector and voltmeter). A quick check to determine whether the demodulation circuit

is operating correctly is to set the internal modulation of the rf synthesizer at 1% and 1 kHz; as the piezo-electric drive synthesizer is swept through 1 kHz, large interference should be evident at the lock-in outputs. The slow search for resonances may now begin. With a 10V drive into the piezo-electric and a ~ 1mm long sample, the amplitude of the resonance should be between 1-30 μV.

Its necessary to determine which resonances arise from the sample and which arise from extraneous sources (pick-up lead, rf lead, instabilities in the piezo-electric assembly, electrical resonances, etc.). The piezo-electric assembly may be checked quickly by pressing down firmly with a wooden stick; if this significantly affects the signal, the resonance can be safely attributed to the assembly. Moving the position of the pick-up slightly with the fine adjustment screw will reduce the amplitude of the resonance only if it arises from the sample or pick-up. The pick-up lead may then be lightly touched with a sharpened wooden stick, painted with silver paint or dabbed with a methanol droplet to determine whether it is the source.

The remaining resonances must now be investigated to ensure that they arise from the sample. The safest (and slowest) test is to put a drop of silver paint on the sample mount and to push it toward the fixed end of the sample. Reducing the effective length of the sample will increase the resonant frequency. A faster (and more dangerous) method is to carefully lay a piece of lint (e.g. a Kimwipe® fiber) on the sample. This should completely damp out any vibration. Another method is to use a drop of methanol either near the fixed end of the sample or on the sample itself on the sample mount. If there are several resonances, they should

roughly obey the proportions for flexural resonances, i.e. 1 : 6.267 : 17.547 : 34.387 : 56.843.

After the experiment, the sample is recovered as follows:

(i) remove the piezo-electric assembly from the base and and again place it on double-sided tape with the sample mount facing up

(ii) cut a long, thin piece of masking tape (~ 1.5" x 0.08") and attach one end to the sample mount and one to the underlying slide

(iii) use a scalpel to pry loose the side of the sample mount while holding the piezo-electric assembly with a pair of heavy forceps

(iv) remove the sample mount and sample from the masking tape and store it for further use.

## References


1. Göran Grimvall, *Thermophysical Properties of Materials* (North-Holland, Amsterdam, 1986).

2. G. Simmons and H. Wang, *Single Crystal Elastic Constants and Calculated Aggregate Properties: A Handbook* (M. I. T. Press, Cambridge, Mass., 1971).

3. A. S. Nowick and B. S. Berry, *Anelastic Relaxation in Crystalline Solids* (Academic Press, New Yord, 1972).

4. Robert W. Keyes, in *Solid State Physics*, F. Seitz, D. Turnbull and H. Ehrenreich ed., (Academic Press, New York, 1967), p. 37.

5. John J. Hall, Phys. Rev. **161**, 756 (1967).

6. Robert W. Keyes, Phys. Rev. Lett. **34**, 1334 (1975).

7. L. D. Landau and E. M. Lifshitz, *Statistical Physics* (Pergamom, London, 1959).

8. A. J. Millis and K. M. Rabe, Phys. Rev. **B38**, 8908 (1988).

9. L. R. Testardi, Phys. Rev. **B12**, 3849 (1975).

10. L. R. Testardi, Phys. Rev. **B3**, 95 (1971).

11. L. R. Testardi, in *Physical Acoustics*, W. P. Mason and R. N. Thurston ed., (Academic, New York, 1973), p. 193.

12. M. Barmatz, L. R. Testardi and F. J. DiSalvo, Phys. Rev. **B12**, 4367 (1975).

13. Xiao-Dong Xiang, Ph.D. Thesis, University of Kentucky, Lexington (1989).

14. M. J. Skove, T. M. Tritt, A. C. Ehrlich and H. S. Davis, Rev. Sci. Instrum. **62**, 1010 (1991).

15. Shen Huimin, Wang Yening, Zhang Zhifang, Zhang Shiyuan and Sun Linhai, J. Phys. C **20**, L889 (1987).

16. T. Tiedje, R. R. Haering and W. N. Hardy, J. Acoust. Soc. Am. **65**, 1171 (1979).

17. R. C. Lacoe, Ph. D. Thesis, University of California, Los Angeles (1983).

18. B. A. Auld, *Acoustic Fields and Waves in Solids* (Wiley, New York, 1973).

19. M. Saint-Paul, J. L. Tholence, H. Noël, J. C. Levet, M. Potel, P. Gougeon and J. J. Capponi, Solid State Comm. **66**, 641 (1988).

20. M. Saint-Paul, J. L. Tholence, H. Noël, J. C. Levet, M. Potel and P. Gougeon, Physica C **166**, 405 (1990).

21. John E. Fischer, Paul A. Heiney, Andrew R. McGhie, William J. Romanow, Arnold M. Denenstein, Jr. John P. McCauley and Amos B. Smith, Science **252**, 1288 (1991).

22. M. Boekholt, J. V. Harzer, B. Hillebrands and G. Güntherodt, Physica C **179**, 101 (1991).

23. Henry Chou, K. Yamada, J. D. Axe, S. M. Shapiro, G. Shirane, Isao Tanaka, Kenichi Yamane and Hironao Kojima, Phys. Rev. **B42**, 4272 (1990).

24. R. L. Willett, M. A. Paalanen, R. R. Ruel, K. W. West, L. N. Pfeiffer and D. J. Bishop, Phys. Rev. Lett. **65**, 112 (1990).

25. Stuart W. Wenzel and Richard M. White, in *Microsensors*, Richard S. Muller, Roger T. Howe, Stephen D. Senturia, Rosemary L. Smith and Richard M. White ed., (IEEE Press, New York, 1991), p. 283.

26. A. Migliori, William M. Visscher, S. E. Brown, Z. Fisk, S. -W. Cheong, B. Alten, E. T. Ahrens, D. A. Kubat-Martin, J. D. Maynard, Y. Huang, D. R. Kirk, K. A. Gillis, H. K. Kim and M. H. W. Chan, Phys. Rev. **B41**, 2098 (1990).

27. A. Migliori, William M. Visscher, S. Wong, S. E. Brown, I. Tanaka, H. Kojima and P. B. Allen, Phys. Rev. Lett. **64**, 2458 (1990).

28. M. H. Jericho and A. M. Simpson, Phys. Rev. **B34**, 1116 (1986).

29. Jr. W. Weaver, S. P. Timoshenko and D. H. Young, *Vibration Problems in Engineering* (Wiley, New York, 1990).

30. R. F. S. Hearmon, *An Introduction to Applied Anisotropic Elasticity* (Oxford University Press, London, 1961).

31. J. W. Brill and W. Roark, Phys. Rev. Lett. **53**, 846 (1984).

32. X.-D. Xiang, J. W. Brill and W. Fuqua, Rev. Sci. Instrum. **60**, 3035 (1989).

33. S. Hoen, I. D. Parker, W. N. Creager and A. Zettl, Syn. Met. **41-43**, 3871 (1990).

34. G. Meyer and N. M. Amer, Appl. Phys. Lett. **53**, 1045 (1988).

35. D. Rugar, H. J. Mamin, R. Erlandsson, J. E. Stern and B. D. Terris, Rev. Sci. Instrum. **59**, 2337 (1988).

36. D. Rugar, H. J. Mamin and P. Guethner, App. Phys. Lett. **55**, 2588 (1989).

37. *RF/IF Signal Processing Handbook* (Mini-Circuits, P. O. Box 350116, Brooklyn, New York, 11235, 1990).

38. An 1/16" pine dowel soaked in methanol proved the easiest to sharpen. No anomalous effects were seen with schlangenholtz dowels.

# Chapter 5: Elastic Response of High-Temperature Superconductors

## 5.1 Introduction

The unusually high superconducting transition temperatures associated with the metallic oxides La-Ba-Cu-O,[1] Y-Ba-Cu-O,[2] and related structures[3-6] suggest a new superconductivity mechanism. The observed zero or very small isotope shifts[7-10] give evidence for electron pairing mediated at least in part by non-phonon excitations. However, recent theoretical advances[11-13] suggest that anharmonic lattice vibrations may explain both the high $T_c$'s and the small isotope shifts. Indeed, the first study of the elastic properties of a high-temperature superconductor (HTSC), performed on $La_{2-x}Sr_xCuO_4$, demonstrated a dramatic lattice-mode softening well above $T_c$.[14] Large anharmonic terms in the interatomic potential are usually a signature of proximity to a structural phase transition. Similarly, for conventional superconductors with relatively high $T_c$'s, such as the A-15 materials, the large $T_c$ appears intimately linked with structural instability.[15, 16]

A particularly useful probe of phonon structure and electron-phonon coupling in a solid is the determination of the bulk elastic properties of the material. For example, soft phonon modes associated with electron-phonon driven Peierls transitions in charge density wave systems,[17] and those associated with the relatively high transition temperatures of most A-15 superconductors,[15, 16] are readily accessible by ultrasound propagation or vibrating reed measurements. The magnitudes of the elastic constants place significant bounds on the form of the interatomic

potentials. Their temperature dependence is an important tool for determining the degree of anharmonicity in the potentials, the presence and thermodynamics of any structural phase transitions, and the effects of various structural defects (dislocations, vacancies, impurities, etc.).

This chapter reports on measurements of Young's modulus (Y) and damping ($\delta$) of both polycrystalline and single crystal HTSC's, employing a modified vibrating reed technique. For $YBa_2Cu_3O_7$, our measurements allow intergranular effects in polycrystalline samples to be distinguished from intrinsic crystal elastic properties.[18] Single crystal elastic measurements in the a-b plane also yield information on the orthorhombic shear. In single crystal studies we find a small anomaly in the Young's modulus near $T_c$ which we identify as resulting from the thermodynamics of the superconducting phase transition. In polycrystalline specimens, a large anomalous lattice stiffening is observed in the vicinity of $T_c$, in accord with other studies.[19-24] Surprisingly, this anomaly persists in single crystal measurements, suggesting it to be an intrinsic material property of $YBa_2Cu_3O_7$. Al-doped crystals show a reduced $T_c$ and Y shows no anomalous effects. For $Bi_2Sr_2CaCu_2O_8$, the superconducting transition has surprisingly little effect on Y or $\delta$. The oxygen configuration of the material significantly affects its elastic properties. Finally, for single crystal Tl-Ba-Ca-Cu-O, Y hardens below $T_c$, though less spectacularly than $YBa_2Cu_3O_7$. From the behavior of Y near $T_c$, $\partial T_c/\partial\sigma$ and $\partial^2 T_c/\partial\sigma^2$ for $\sigma$ along the a-b plane is calculated for each of these materials. Because the stress dependence of $T_c$ varies significantly from material to material, these results imply that no additional phase

transition, which couples directly to stress in the a-b plane, underlies the superconducting pairing mechanism.

The remainder of this chapter is organized as follows: Sect. 5.2 describes our experimental technique; Sect. 5.3 details our results for polycrystalline and single crystal $YBa_2Cu_3O_7$. Sections 5.4, 5.5, and 5.6 describe and discuss the elastic properties of Al-doped $YBa_2Cu_3O_7$, $Bi_2Sr_2CaCu_2O_8$, and Tl-Ba-Ca-Cu-O, respectively. Sect. 5.7 summarizes the conclusions culled from these experiments.

## 5.2 Experimental technique

Polycrystalline samples of $YBa_2Cu_3O_7$ were prepared by standard methods described elsewhere.[25] Needle-shaped specimens suitable for vibrating reed measurements were cut from sintered pellets using a diamond saw. Single crystals of $YBa_2Cu_3O_7$ were prepared in a gold crucible from an off-stoichiometry eutectic melt. Following synthesis, crystals with typical dimensions 1mm x 0.25mm x 0.1mm (small dimension = c-axis) were further annealed in an oxygen environment at 750°C. Resistivity measurements showed $T_c$'s near 91K for both polycrystalline and single crystal samples, with transition widths $\leq$ 2K. dc magnetic susceptibility measurements using a SQUID magnetometer indicated typical diamagnetic onsets near 90K with ~10K transition widths.

Single crystals of $Bi_2Sr_2CaCu_2O_8$ are grown by mixing powders of $Bi_2O_3$, CuO, $SrCO_3$, and $CaCO_3$ in molar percentages 22.4%, 32%, 26.9%, and 18.7%, respectively, in a ball mill with acetone. The resulting powder is placed in a gold crucible, heated at 920°C for 5 hours and cooled to 820°C at a rate of 3°C/hour in flowing $O_2$. Crystals grow as micaceous sheets and

SEM analysis confirmed the composition as $Bi_2Sr_2CaCu_2O_8$. X-ray analysis shows that the c-axis is perpendicular to the cleavage plane and has a spacing of 3.0nm. Typical crystal dimensions are 1.50 x 0.10 x. 0.02 $mm^3$ (the smallest dimension is the c-axis). The samples are characterized by both 4-probe dc resistance and dc magnetic susceptibility which indicate a bulk transition temperature of ~84K and resistive transition widths of 2-3K.

For elasticity measurements, samples are rigidly clamped with silver paint at one end. For some materials ($YBa_2Cu_3O_7$, Al-doped $YBa_2Cu_3O_7$, and $Tl_3Ba_2Ca_2Cu_3O_{10}$), a load mass (silver paint) is attached at the free end to reduce the flexural resonant frequency. As described in Chapt. 4, flexural vibrations are induced in the sample capacitively[26] and detected with an rf capacitive technique.[27] Single crystals are mounted with the c-axis parallel to the direction of oscillation. Changes in response frequency $\omega_r$ are related to Y by $\Delta Y/Y = 2\Delta\omega_r/\omega_r$, and $\delta$ is determined directly from the reciprocal of Q, where Q is proportional to the resonance vibration amplitude.

**5.3 Elastic measurements on polycrystalline and single crystal $YBa_2Cu_3O_7$**

Fig. 5-1 shows Y and $\delta$ for polycrystalline $YBa_2Cu_3O_7$ as functions of temperature.[9] The most striking feature is a sharp increase in Y just below $T_c$ ($\Delta Y/Y = +4.5\times10^{-3}$); this is accompanied by a dramatic peak in $\delta$. The anomaly in Y at a second order phase transition can be related to the stress dependence of $T_c$ using thermodynamic considerations[28, 29]

$$\frac{\Delta Y}{Y} = -\frac{Y\Delta C_p}{T_c}\left(\frac{\partial T_c}{\partial \sigma_i}\right)^2 \qquad (5.1)$$

where

$$\Delta Y \equiv Y(T_c^-) - Y(T_c^+) \qquad (5.2)$$

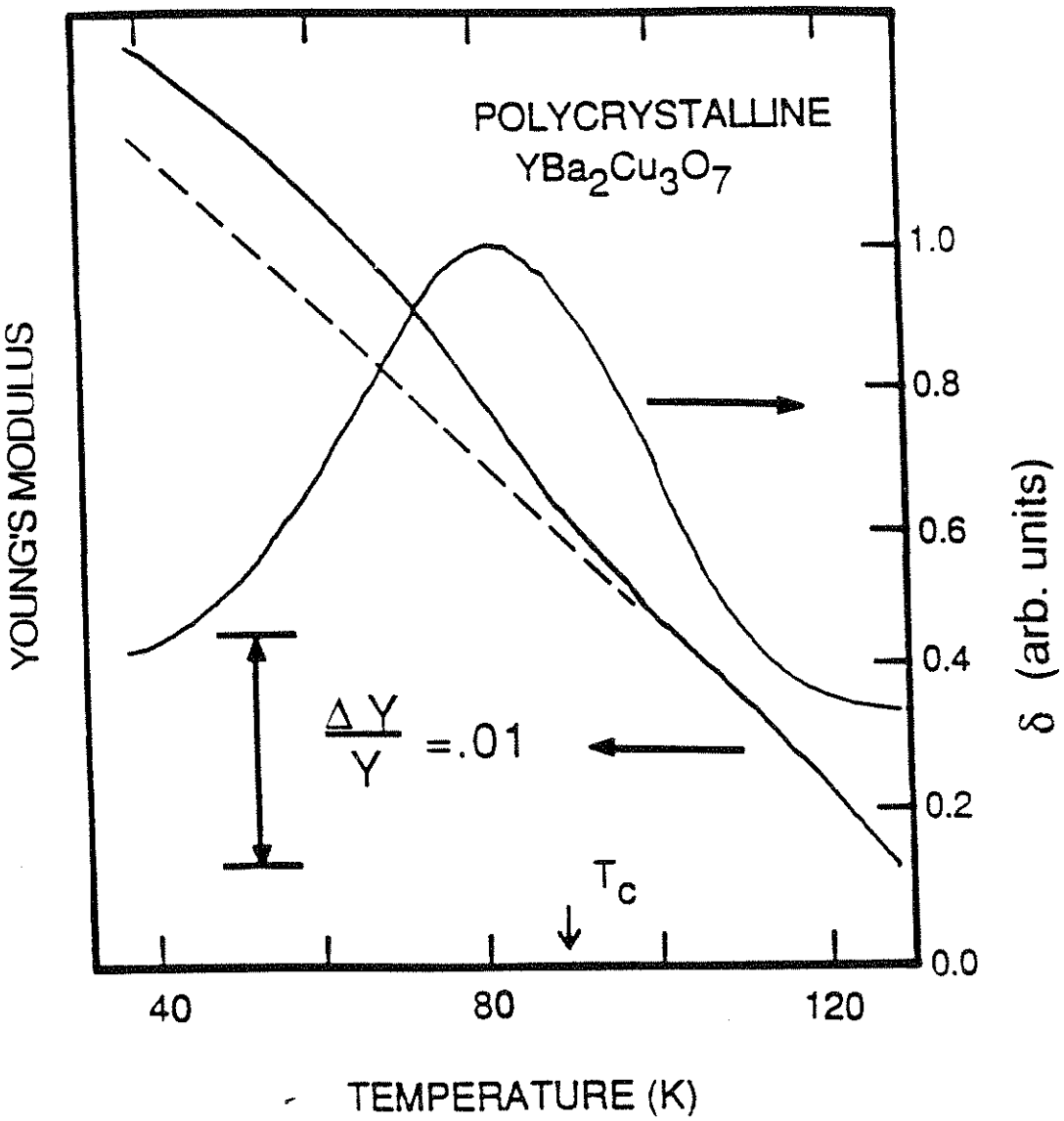


Fig. 5-1. Young's modulus (Y) and internal friction (δ) in polycrystalline $YBa_2Cu_3O_7$. The dashed line is an extrapolation of the high-temperature Y behavior.

and $\sigma_i$ is the appropriate stress and $\Delta C_p$ is the specific heat anomaly associated with the transition. With $\Delta C_p/T_c = 55$ mJ/mole·K$^2$ (Ref. 30) and assuming $\partial T_c/\partial \sigma_i \approx \partial T_c/\partial P \approx .07$ K/kbar (Ref. 31) and $Y = 2.2 \times 10^{12}$ dynes/cm$^2$ (Ref. 32), $\Delta Y/Y$ at $T_c$ is predicted to be of order $-6 \times 10^{-5}$. This predicted value is of opposite sign and orders of magnitude smaller that our measured Y change in the polycrystalline specimen. Similar unusually large anomalies at $T_c$ have been reported for polycrystalline $YBa_2Cu_3O_7$ by ultrasonic and torsional measurements.[19-24]

Recent elasticity studies[33] of (polycrystalline) high-$T_c$ superconductors have indicated that the polycrystalline Young's modulus may be strongly influenced by the single crystal shear modulus, which demonstrates the importance of measuring the elastic properties of single crystal specimens. Single crystal measurements also isolate non-intrinsic features introduced by grain boundaries.

Figs. 5-2a,b show, respectively, Y and $\delta$ as functions of temperature for single crystal $YBa_2Cu_3O_7$.[18, 34] Between 295K and 4.2K, Y monotonically increases with a total change of 11%. However, substantial changes in slope in Y are apparent near $T_c$ and at other temperatures. $\delta$ shows a dramatic peak near $T_c$. Before discussing these large anomalies, we examine the detailed behavior of Y near $T_c$. Fig. 5-3 shows, on a high resolution scale, Y as a function of T near 80K. The data has been adjusted by subtracting a constant slope (that measured at 70K) from experimental points. This adjustment allows discontinuities in Y to be more easily distinguished. Near 80K, which corresponds roughly to the magnetic transition midpoint for this particular crystal, there is a discontinuity in the Young's modulus $\Delta Y/Y = -9 \times 10^{-5}$ which is of the expected sign and

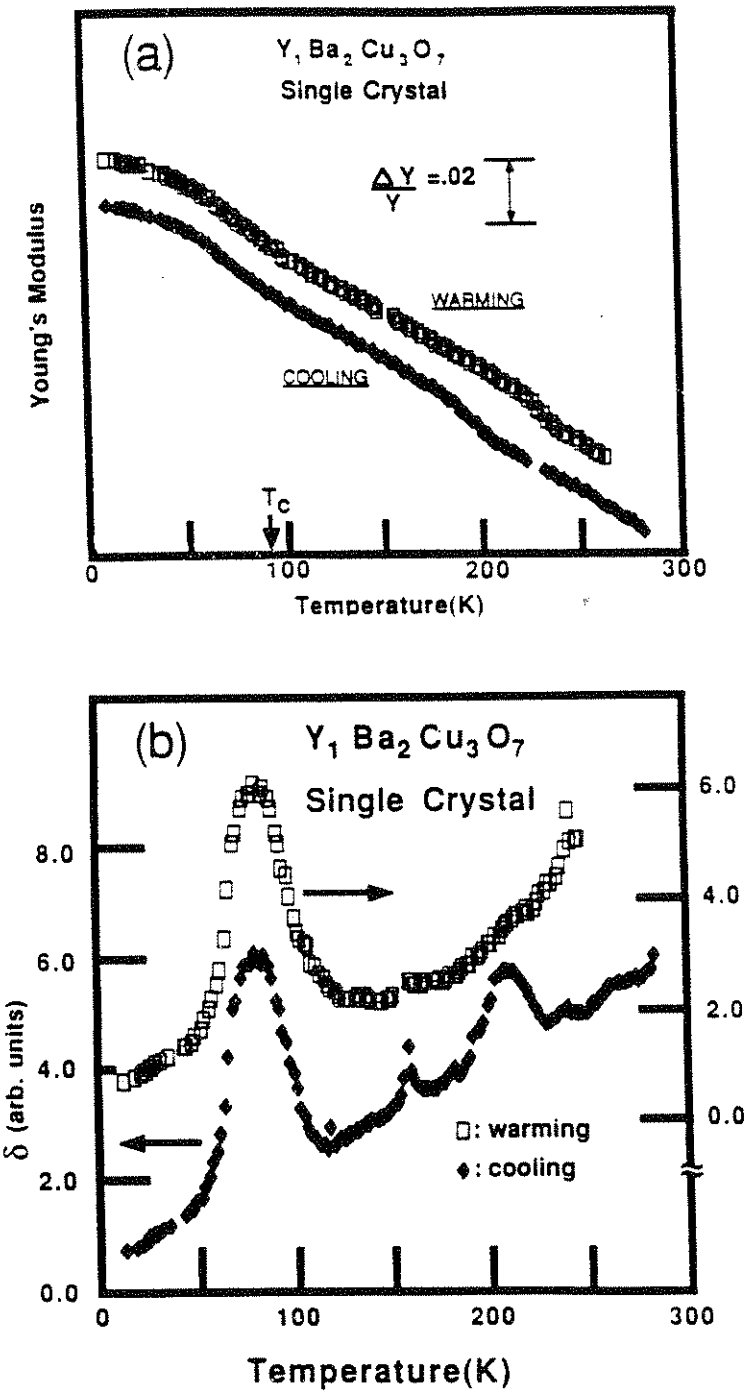


Fig. 5-2. (a) Young's modulus vs T in single crystal $YBa_2Cu_3O_7$. The warming and cooling curves are vertical displaced for clarity.
(b) Internal friction vs T for single crystal $YBa_2Cu_3O_7$.

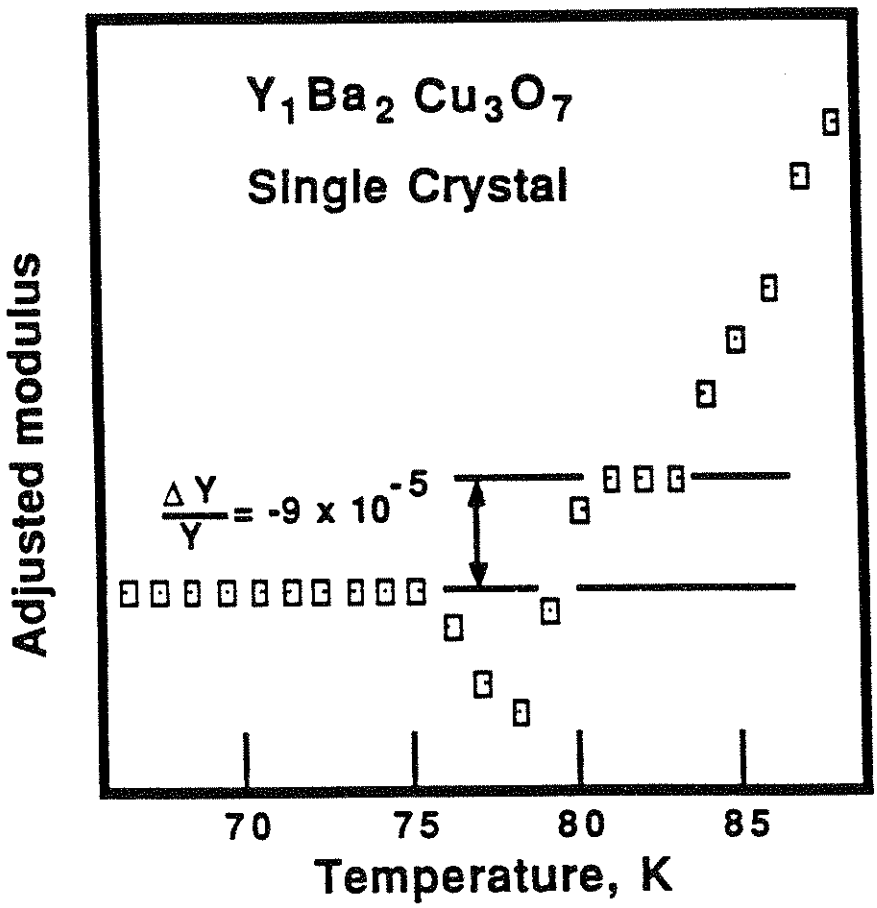


Fig. 5-3. Adjusted (see text) Young's modulus in single crystal $YBa_2Cu_3O_7$ near $T_c$. The data indicate a discontinuity $\Delta Y/Y = -9 \times 10^{-5}$.

order of magnitude from the thermodynamics of the superconducting phase transition (see above). From equation 5.1, our measured $\Delta Y/Y$ yields $\partial T_c/\partial \sigma_i$ = 0.09 K/kbar. This is the predicted a-b plane stress dependence of $T_c$ in single crystal $YBa_2Cu_3O_7$, and the first such prediction for a high-$T_c$ superconductor, and is similar in magnitude to $\partial T_c/\partial P$ determined from pressure studies,[31, 35, 36] i.e. $\partial T_c/\partial P$ = 0.043 - 0.07 K/kbar.

Fig. 5-3 shows significant change in slope at the superconducting transition; this slope change causes the apparent hardening for $T<T_c$ visible in Figs. 5-1 and 5-2a. From this data, $\Delta(\partial \ln Y/\partial T) = -1.3 \times 10^{-4}\ K^{-1}$,

where
$$\Delta\left(\frac{\partial \ln Y}{\partial T}\right) \equiv \frac{1}{Y}\left[\frac{\partial Y}{\partial T}(T_c^-) - \frac{\partial Y}{\partial T}(T_c^+)\right]. \qquad (5.3)$$

The large slope change is similar to that present at $T_c$ for the A-15 materials[15, 16] and indicates that the condensation of electrons into the superconducting state significantly affects the interatomic potential. This would be the case if there were a nearby structural transition (soft mode) which is being stabilized by the electronic condensate. The values of $\Delta(\partial \ln Y/\partial T)$ have traditionally been used to determine $\partial^2 T_c/\partial \sigma_i^2$; however, formal thermodynamic calculations[29, 37] yield

$$\Delta\left(\frac{\partial \ln Y}{\partial T}\right) = -\frac{Y \Delta C_p}{T_c}\left[\frac{\partial^2 T_c}{\partial \sigma_i^2} + \frac{A}{T_c}\left(\frac{\partial T_c}{\partial \sigma_i}\right)^2 + B\left(\frac{\partial T_c}{\partial \sigma_i}\right)\right] \qquad (5.4)$$

where $A = (\Delta C_p/T_c)/[\Delta(\partial C_p/\partial T)]$ and B is generally small and depends on the third order strain tensor and the effect of strain on the electronic density. For a conventional, weakly coupled, superconductors, $A \equiv 0.43$.[38] From specific heat data[39] on polycrystalline samples of $YBa_2Cu_3O_7$, $A \equiv 0.062$. For either case, the second term on the right hand side of equation

5.4 is too small to contribute significantly. The third term should not be particularly large for this material because Y(T) is not particularly dependent on temperature nor does the free carrier density change drastically with applied stress. Therefore, $\partial^2 T_c/\partial\sigma_i^2 = +0.01$ K/kbar$^2$. Thus, even for small stresses (~kbar), the quadratic dependence of $T_c$ should dominate the linear dependence. A variety of pressure experiments[31, 35, 36] have seen very little or no quadratic pressure dependence of $T_c$. However, these experiments were performed at relatively high pressures (4-140 kbar). Interestingly, two experiments[40, 41] which included pressures less that 1 kbar both exhibited significant quadratic pressure dependence of $T_c$.

The data of Figs. 5-2a,b show additional unusual and unexpected features. Changes in the slope of Y are observed near 200-240K (hysteretic) and 100K, and there is a gradual rolloff in Y near 40-60K. Fig. 5-2b shows that many of the features in Y have associated structures in $\delta$ (the feature near 200K in Fig. 5-2b is particularly interesting since it is largely suppressed upon sample warming). Interestingly, a sharp peak at 160K and additional structure near 260K are visible in the internal friction yet no associated anomalies are evident in the Young's modulus. The reduced temperature dependence of the Young's modulus which occurs below 60K and the associated reduction of the internal friction has been seen in other materials[42] and can be attributed to the freezing out of phonon modes as $T\rightarrow 0$. A rather surprising finding is that near 100K, the measured single crystal data is similar to that for the polycrystalline samples (Fig 1). This suggests that the anomalous stiffening below $T_c$

observed in polycrystalline samples is not due to intergranular effects, but is intrinsic to $YBa_2Cu_3O_7$.

It has been suggested[19] that the dramatic elastic anomaly near $T_c$ in $YBa_2Cu_3O_7$ is associated with a structural phase transition, as evidenced by high resolution x-ray scattering experiments[43] which show an anomaly in the orthorhombic splitting. In the geometry employed for our single crystal vibrating reed measurements, the measured Y is that associated with uniaxial loading along the a-b plane (Cu-O planes); the corresponding shear modulus is that between these planes. The general (first order corrected) expression[44] relating $\omega_r$ and Y is

$$\omega_r^2 = Yt^3s\,[(1 + Kt^2Y/L^2G)\,4L^3M]^{-1} \tag{5.5}$$

where t is the sample thickness (order 0.1mm), s is the sample width (order 0.25mm), L is the sample length (order 1mm), M is the loading mass, G is the shear modulus, and K~1. From Eq. (2), $\omega_r$ is significantly influenced by G only in the limit $G \leq Y/100$. G is bounded by the arithmetic and geometric means of $c_{44}$ and $c_{55}$ and for $YBa_2Cu_3O_7$ it is unlikely that the above limit is satisfied.

The direct connection between Y measured in our experiments and the stiffness tensor $c_{ij}$ is not straightforward because of the substantial twinning in the a-b plane. If we assume that the a and b axes are randomly distributed in the a-b plane, then in the Reuss limit

$$Y_R = \frac{8(c_{11} - c_{12})\left[c_{33}(c_{11} + c_{12}) - 2c_{13}^2\right]}{c_{33}(6c_{11} - c_{12}) - 4c_{13}^2 + \Delta/c_{66}} \tag{5.6}$$

where $\Delta = (c_{11} - c_{12})[c_{33}(c_{11} + c_{12}) - 2c_{13}^2]$ and for convenience we have assumed $c_{11} \equiv c_{22}$ and $c_{13} \equiv c_{23}$. In the Voigt limit,

$$Y_V = \frac{2(c_{11} - c_{12} + 2c_{66})[c_{33}(c_{11} + c_{12}) - 2c_{13}^2]}{c_{33}(3c_{11} + c_{12} + 2c_{66}) - 4c_{13}^2} \tag{5.7}$$

These expressions act as formal boundaries for Y, i.e. $Y_R \leq Y \leq Y_V$. In both limits, the orthorhombic shear modulus $C_s=(c_{11} - c_{12})/2$ influences the effective Y. This modulus is conjugate to the orthorhombic strain 2(b-a)/(b+a), which some structural studies[43] have suggested to show anomalous behavior near $T_c$. The anomalously large increase in $\partial Y/\partial T$ could arise from changes in the orthorhombic shear. The source of our observed single crystal elastic anomalies near 160K, 200-240K, and 265K is not clear. There are no confirmed corresponding anomalies in the structural or magnetic properties of $YBa_2Cu_3O_7$ in these temperature ranges. Interestingly, numerous reports have appeared of resistive fluctuations in Y-Ba-Cu-O between 220K and 240K.

After the completion of this experiment, several additional results have been reported for single crystal $YBa_2Cu_3O_7$. M. Saint-Paul *et al.*,[45] using an ultrasonic technique, found no anomalies at $T_c$ in $c_{11}$, $c_{33}$, and $c_{44}$ to 50 ppm. X. D. Shi *et al.*,[32] however, confirmed the existence of softening in Y and change in slope associated with the superconducting transition. From their study, $\Delta Y/Y \sim 3.8 \times 10^{-4}$, a value which yields $\partial T_c/\partial \sigma_i$ five times larger than the values determined from pressure studies, and $\Delta(\partial \ln Y/\partial T) \sim 7 \times 10^{-5}\,K^{-1}$.

In conclusion, the single crystal Young's modulus of $YBa_2Cu_3O_7$ has been measured and compared to the polycrystalline result. The expected

elastic anomaly at $T_c$ has been resolved for the first time, and it is consistent with thermodynamic predictions. Intergrain coupling in polycrystalline samples does not appear to be the sole source of the lattice stiffening below $T_c$.

### 5.4 Elastic properties of single crystal Al-doped $YBa_2Cu_3O_7$

The large slope change at $T_c$ visible in Figs. 8-1 and 8-3 suggests that a structural transition may be associated with superconductivity in $YBa_2Cu_3O_7$. This transition can be further investigated by altering the crystal structure, either by substituting different elements or by removing oxygen, to change the superconducting properties. Growing crystals in an aluminum crucible causes Al atoms to be substituted at some of the copper sites and reduces $T_c$ to ~60K (see inset Fig. 5-4b). These crystals typically are thinner than pure $YBa_2Cu_3O_7$ crystals (typical dimensions 1.00 x 0.20 x 0.050 $mm^3$) and are thus ideal for vibrating reed measurements.

Fig. 5-4 shows the Young's modulus and damping as functions of temperature for one such crystal. Though the total Young's modulus change between 4.2K and 300K is similar (13.5% versus 10.5% for pure $YBa_2Cu_3O_7$), few features present in Fig. 5-2 are evident in Fig. 5-4. In particular, there is no slope change at 85K or at $T_c$ (60K). In fact, Fig. 5-5b shows a slight downward curvature from 60-50K, implying that lattice anharmonicity washes out any slope change associated with $T_c$. The strong damping peak at 85K for the pure crystal is barely visible in the doped sample. Moreover, the doped material shows additional damping peaks at 150K and 250K. Clearly, the substitution of Al significantly affects both the superconducting and elastic properties. Because any Young's modulus

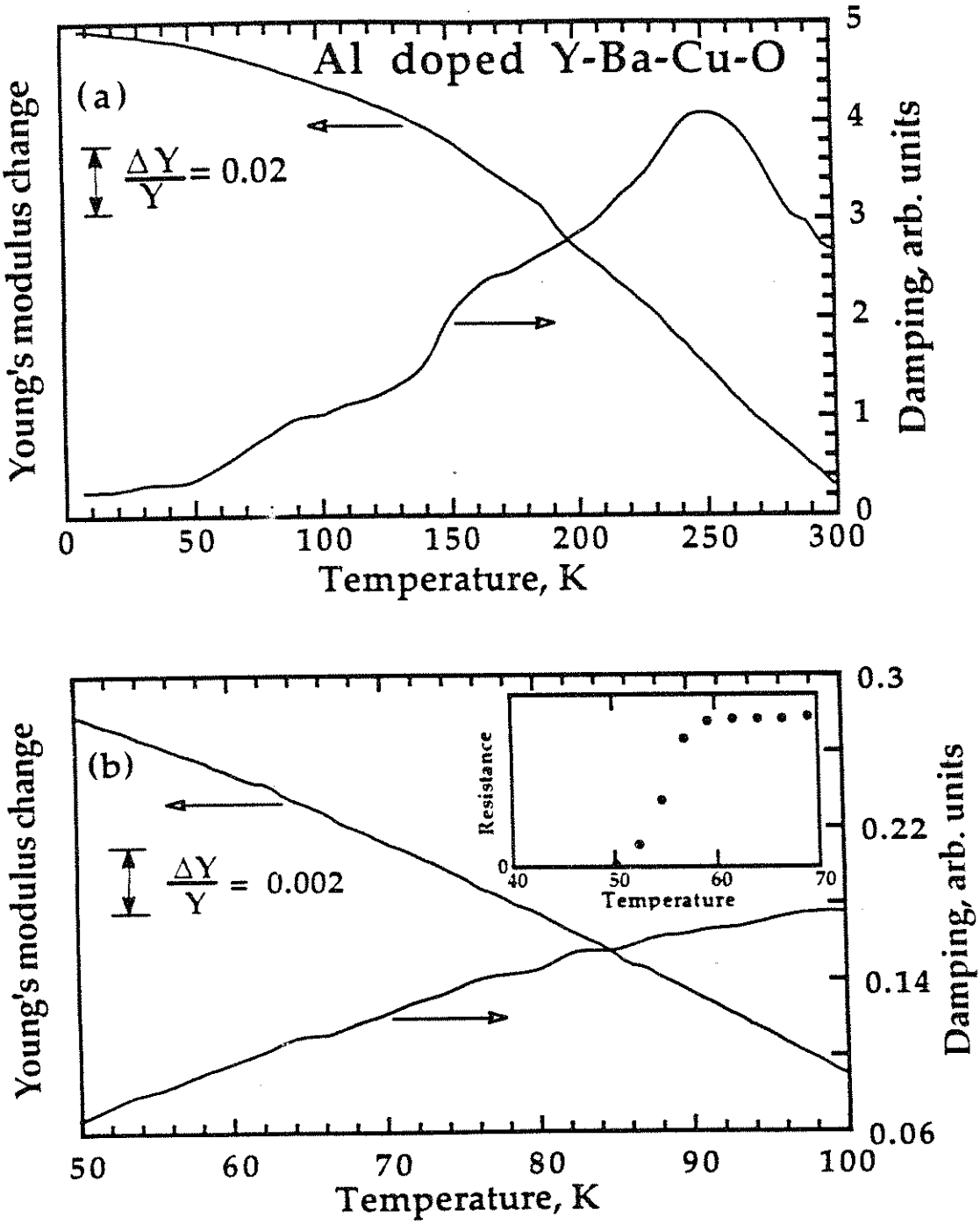


Fig. 5-4. Young's modulus and damping of Al-doped $YBa_2Cu_3O_7$ as functions of temperature in the ranges (a) 4.2-300K and (b) 50-100K. The inset of (b) shows the sample resistance in this same region.

anomaly associated with $T_c$ is imperceptible, both $\partial T_c/\partial\sigma_i$ and $\partial^2 T_c/\partial\sigma_i^2$ are small, and it suggests that lattice stability increases as $T_c$ is reduced. However, it is clear from a comparison of the crystal morphologies and of Figs. 5-2 and 5-4 that Al substitution affects the structure more drastically than simply altering $T_c$.

## 5.5 Elastic properties of single crystal $Bi_2Sr_2CaCu_2O_8$

### 5.51 Introduction

In $Bi_2Sr_2CaCu_2O_8$ the electrons which condense into the superconducting state lie in Cu-O planes. Several theorists[11, 13] have suggested that either the in-plane oxygen atoms or the apical oxygen atoms lie in strongly anharmonic wells. Because the positions of these atoms strongly affect the Fermi surface electrons, they may play an important role in electron pairing.[46] Vibrating reed studies of this material, as for $YBa_2Cu_3O_7$, are important probes for incipient structural transitions and phonon softening. This section describes first the elastic properties of single crystal $Bi_2Sr_2CaCu_2O_8$ (Sect. 5.52) and second the effect of oxygen deficiencies on its superconducting and elastic properties (Sect. 5.53).

### 5.52 Elastic properties of oxygenated $Bi_2Sr_2CaCu_2O_8$

$Bi_2Sr_2CaCu_2O_8$, because it grows as micaceous sheets, is ideally suited to vibrating reed measurements. Since the c-axis is parallel to the direction of oscillation, the experiment probes the Young's modulus for uniaxial stress in the a-b plane. If it is assumed that the stiffnesses in the a and b directions are roughly equal ($c_{11}=c_{22}$; $c_{13}=c_{23}$), then

$$Y = (c_{11} - c_{12})\left(1 + \frac{c_{12}c_{13} - c_{13}^2}{c_{11}c_{33} - c_{13}^2}\right). \qquad (5.8)$$

Y depends strongly on the orthorhombic shear modulus ($C_s=c_{11} - c_{12}$) and weakly on $c_{33}$ and $c_{13}$. Using the resonant frequencies of four crystals and equation 4.2, $Y= 1.1 \pm 0.3 \times 10^{12}$ dynes/cm$^2$ at room temperature; this value is consistent with ultrasonic[47] and Brillouin scattering[48] experiments.

Fig. 5-5 depicts the Young's modulus change and damping as functions of temperature for two samples of the ten studied. The softening between 4.2K and 300K, $\Delta Y/Y(300K)$, varies significantly from sample to sample. Sample #2 shows the smallest softening (~3.4%) of all samples. However, other than a scaling factor, Y depends similarly on temperature for all samples. Wachtman *et al.*[49] and Grimvall[42] noticed that Y(T) for many oxides can be well described by

$$Y(T) = [1 - bT\exp(-T_0/T)]Y(0), \qquad (5.9)$$

where b is a parameter which depends on the lattice anharmonicity; the Debye temperature ($\theta_D$) ~ $2T_0$; and Y(0) is the zero temperature Young's modulus. At large T, Y(T) in equation 5.9 is linear and extrapolates to Y(0) at $T=T_0$. For all samples studied, $2T_0 \cong 160$K. From specific heat measurements, $\theta_D$~250K.[50, 51] The discrepancy between the two $\theta_D$ suggests that lower energy phonons have a larger interaction with the non-quadratic terms in the interatomic potential and contribute a larger fraction of the anharmonic softening. Interestingly, the slope of Y(T) does not approach zero for $T<T_0$. Indeed, for some samples, the slope increased for T<15K. These results suggest that there is a linear distribution of low energy strain states which contribute significantly to Y(T), perhaps arising from the coupling of Cu spins or from the movement of oxygen vacancies through a variety of barriers. Low temperature specific heat data show a

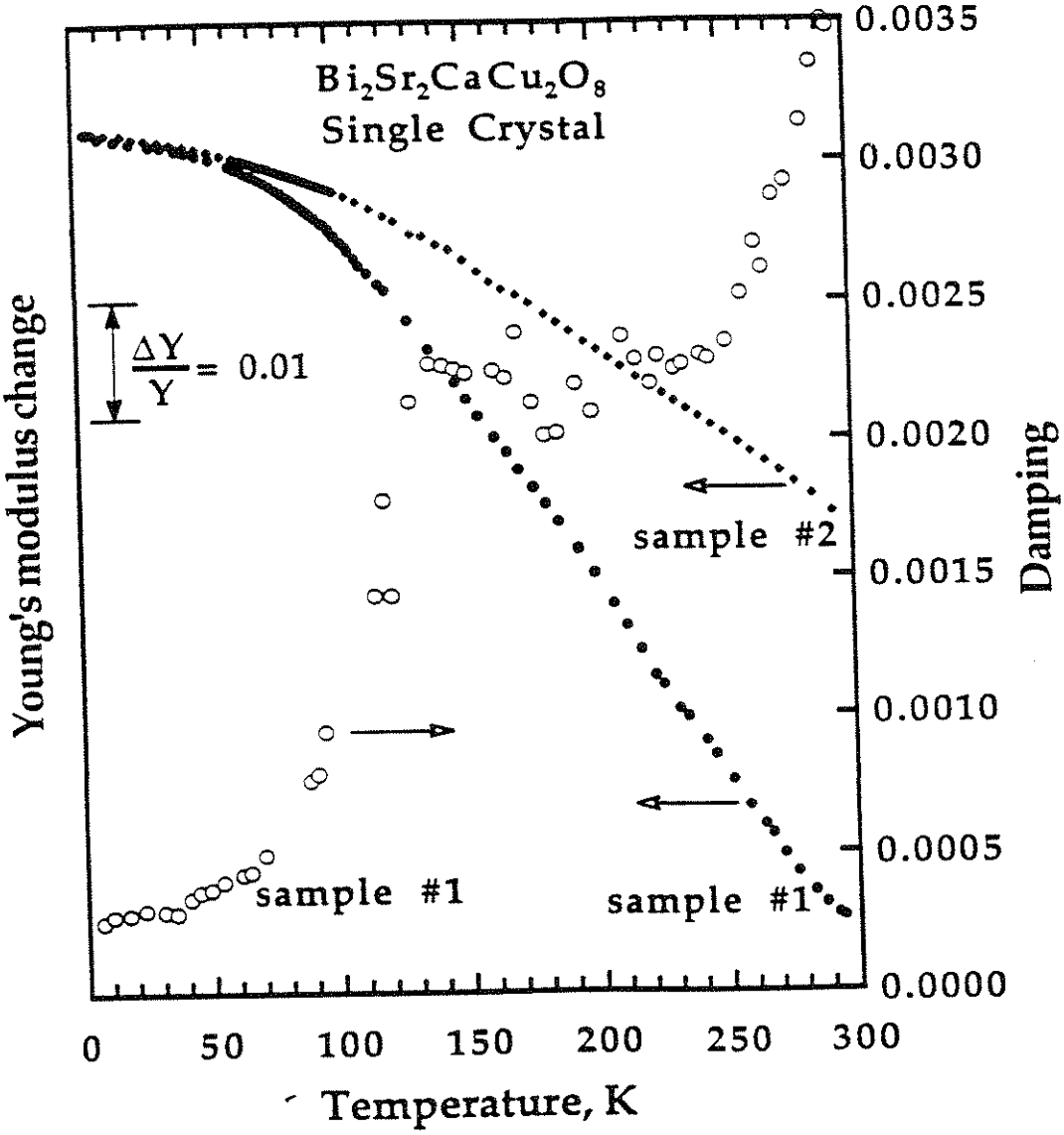


Fig. 5-5. Young's modulus and damping as functions of temperature for two single crystals of $Bi_2Sr_2CaCu_2O_8$.

1/T dependence for T< 3.5K, a characteristic of spin glasses and other two-level systems.[51]

Fig. 5-6 shows Y as a function of T near $T_c$. The resistive transition (shown in the inset for a typical sample) is centered at 84K with a 2K 90%-10% width. Magnetic measurements on similar crystals show 5-10K transitions which start 1-2K below the resistive onset. Unlike $YBa_2Cu_3O_7$, $Bi_2Sr_2CaCu_2O_8$ shows no large change in $\partial Y/\partial T$ at $T_c$. Indeed, even after a linear slope, fitted from 90K to 100K, has been subtracted from Y(T), no slope change at $T_c$ is evident for either of the samples (see Fig. 5-6b). The scatter in the data reflects small, irreversible, changes in the sample geometry, i.e. minor crack growth or delamination of one micaceous sheet from another. Using sample #2 to set bounds on anomalies associated with the transition, we find

$$|\Delta Y/Y| < 1.0 \times 10^{-5} \tag{5.10}$$

and

$$-8.3 \times 10^{-7}K^{-1} < \Delta(\partial \ln Y/\partial T) < +4.0 \times 10^{-6}K^{-1}. \tag{5.11}$$

Here, we assume that the transition occurs over 5K and starts at 84K. Using equation 5.2, E~70GPa (Ref. 48), and $\Delta C_p/T_c \sim$ 26 mJ/mole·K$^2$ (Ref. 52), we determine $|\partial T_c/\partial \sigma| < 0.09$ K/kbar for uniaxial stresses applied along the a-b plane. In Fig. 5-6b, sample #2 shows a small softening of ~0.5 x $10^{-5}$ at 83K; however, this lies within the experimental uncertainty of our data. The change in slope at $T_c$ is often used to determine $\partial^2 T_c/\partial \sigma^2$;[16, 19] however, as shown in equation 5.4, there are many additional terms which must be considered. Because $\Delta(\partial \ln Y/\partial T)$ is small, $\partial^2 T_c/\partial \sigma_i^2$ is likely to be small for this material. Assuming that the terms in equation 5.4 do not fortuitously cancel, we set the following bounds on $\partial^2 T_c/\partial \sigma_i^2$:

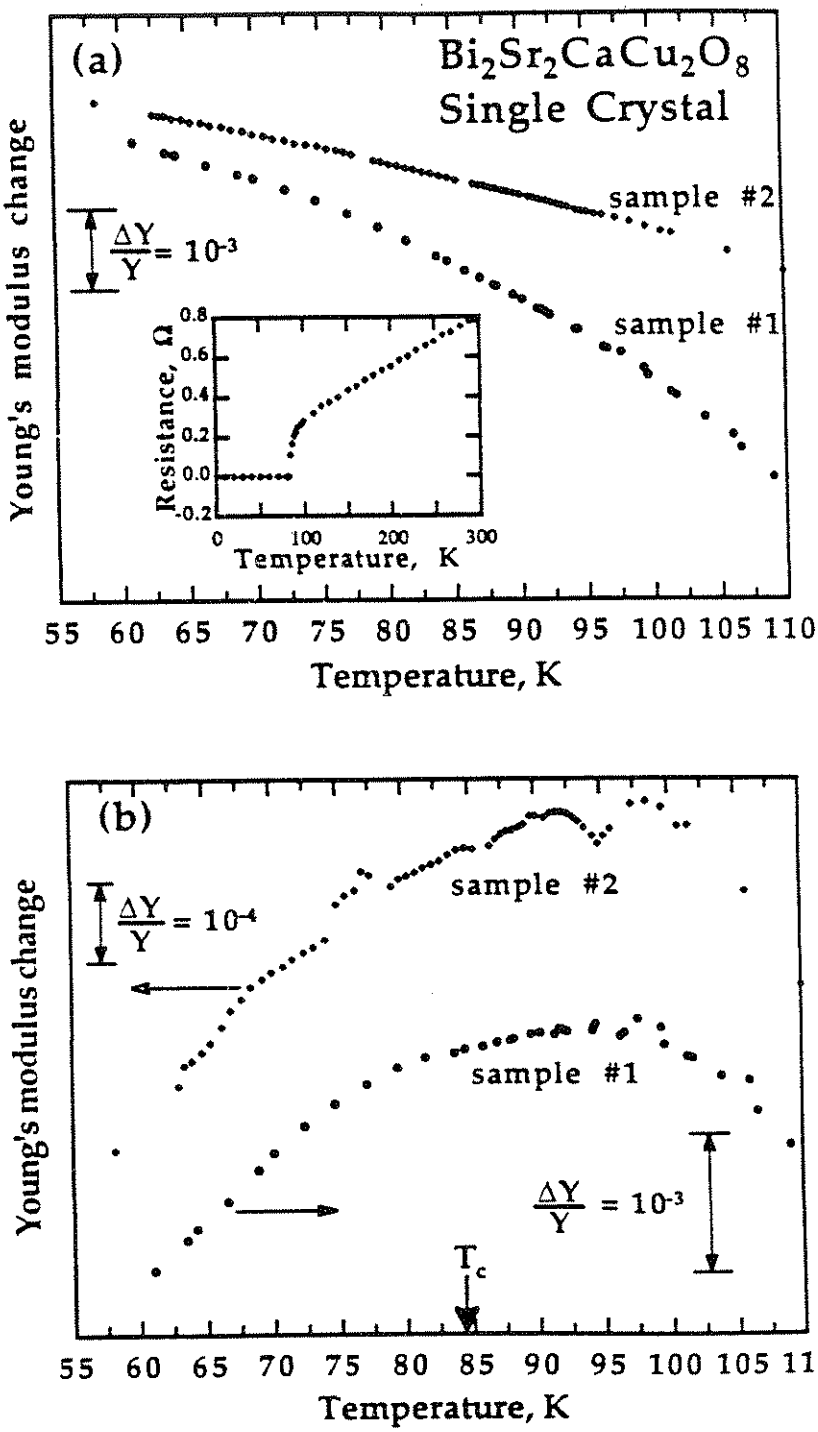


Fig. 5-6. (a) Young's modulus vs T for two single crystals of $Bi_2Sr_2CaCu_2O_8$ near $T_c$ (~84K). The inset show the resistance of a crystal from the same batch. (b) Modified Young's modulus vs T for two single crystals of $Bi_2Sr_2CaCu_2O_8$ near $T_c$. The Young's modulus has been modified by subtracting a linear best fit (90-100K) from the data.

$$-3 \times 10^{-3}\ \mathrm{K/kbar^2} < \partial^2 T_c/\partial\sigma_i^2 < 6.5 \times 10^{-4}\ \mathrm{K/kbar^2}. \qquad (5.12)$$

These values are similar to those for conventional superconductors in which there is believed to be no structural softening.[16] A pressure study[53] on multi-phase Bi-Sr-Ca-Cu-O found that both transition temperatures (85K and 110K) increased with applied pressure; $\partial T_c/\partial P = 0.13$ K/kbar. While this value lies outside our bounds for $\partial T_c/\partial\sigma_i$, it includes the effect of c-axis stress on $T_c$. No quadratic pressure dependence of $T_c$ was evident.

After the completion of this experiment, there have been several additional investigations of the elastic properties of $Bi_2Sr_2CaCu_2O_8$. X. D. Xiang *et al.*[37] have carefully studied G for shear stresses with a c-axis component (i.e. it probes some combination of $c_{44}$, $c_{55}$, $c_{13}$, or $c_{23}$, the exact relation depending sensitively of sample geometry). They found $\Delta G/G < 10^{-4}$ and $\Delta(\partial \ln G/\partial T) < 4 \times 10^{-5}$ K$^{-1}$ which implies that $\partial^2 T_c/\partial\sigma_\beta^2 < 9 \times 10^{-3}$ K/kbar$^2$ for $\sigma_\beta$, the appropriate shear stress. This value is an order of magnitude less than that estimated for other superconductors[29] and indicates that the superconducting state does not strongly couple to out-of-plane shear stresses. Using Brillouin light scattering, which determines the high frequency (~20GHz) $\omega$ vs. k for acoustic phonons, Boekholt *et al.*[48] determined the following elastic constants: $c_{11}$ = 125 GPa, $c_{33}$ = 76 GPa, $c_{12}$ = 79 GPa, $c_{13}$ =56 GPa, and $c_{44}$ = 16 GPa. Ultrasonic measurements on ceramics[54, 55] have yielded confusing results with a plethora of possible phase transitions and much scatter in the data, believed to arise from sample porosity and variation in the intergranular coupling. In ultrasonic measurements on single crystal $Bi_2Sr_2CaCu_2O_8$, Saint-Paul *et al.*[47] and Wang *et al.*[56] found substantial softening near $T_c$ of the longitudinal mode launched in the a-b plane ($\Delta V_L/V_L \sim 2 \times 10^{-4}$). Recent experiments[57, 58] on

whisker-like samples of $Bi_2Sr_2CaCu_2O_8$ have found peculiar behavior of the stress-strain curve and of Y(T). These crystals grow with the a-axis along the whisker axis. For uniaxial stresses applied along this axis, they found a surprisingly small Young's modulus (~20 GPa), which conflicts with the values of Y and $c_{ij}$ derived in the all other experiments. Moreover, for this geometry, Y decreases with decreasing temperature and the stress-strain curves show a peculiar hysteresis at high temperature.[58] It is suggested that there is a stress induced phase transition of 270K<T<330K and that vibrating reed and ultrasonic measurements do not detect this transition because the time scale for the phase transition is longer than the period of the applied stress. Another tensile experiment[56] detected ferroelastic behavior at 95K and 130K. Interestingly, one experiment on $YBa_2Cu_3O_7$, also using a direct measurement of the stress-strain curve showed similar results.[59] These curious results are difficult to interpret because significant variations in stress can occur when applying a strain to a thin sample. Moreover, sheet delamination may also play a role — at least for the $Bi_2Sr_2CaCu_2O_8$ material. However, these results may also indicate additional, stress sensitive, phase transitions and lattice instabilities in these materials.

In conclusion, we find that $Bi_2Sr_2CaCu_2O_8$ exhibits no anomalies in Y or $\partial Y/\partial T$ at the superconducting transition. This behavior places severe constraints on $\partial T_c/\partial \sigma_i$ and $\partial^2 T_c/\partial \sigma_i^2$ for $\sigma_i$ along the a-b plane. Though $YBa_2Cu_3O_7$ has a large $\partial^2 T_c/\partial \sigma_i^2$ at $T_c$, reminiscent of the A-15 materials, the fact that $Bi_2Sr_2CaCu_2O_8$ shows so little stress dependence of $T_c$ suggests that a structural instability does no underlie the electronic pairing mechanism in these materials. However, the Young's modulus measured

(eqtn 5.8) does not equally sample all crystal moduli, and it may certainly be possible an instability exists which does not couple strongly to the orthorhombic shear ($c_{11}$ - $c_{12}$).

**5.53 Young's modulus studies of oxygen deficient $Bi_2Sr_2CaCu_2O_{8-y}$**

The free carrier density of the superconducting cuprates is extremely sensitive to oxygen stoichiometry. In the normally insulating $La_2CuO_{4-\delta}$, it is possible to induce metallic, and even superconducting behavior by the addition of oxygen interstitials.[60-63] Indeed, Preyer *et al.*[64-66] have suggested that the carriers significantly affect local microscopic strain. An experiment probing Y at low T as a function of hole doping would yield important information about these carriers. $YBa_2Cu_3O_{7-x}$ shows a striking variation of $T_c$ with x, having a plateau at 60K for $x \cong 0.5$ and decreasing to zero as $x \rightarrow 1$.[67-69] $T_c$ depends sensitively on the annealing conditions which control the ordering of oxygen vacancies in the Cu-O chains.[68, 70-73] In $Bi_2Sr_2CaCu_2O_8$, oxygen stoichiometry strongly affects the normal state resistivity and the superconducting transition.[74-78] Oxygen is removed by vacuum or argon annealing crystals at elevated temperatures (275°C - 500°C). Vibrating reed studies of crystals with different oxygen configurations provide important information on the role of oxygen in stabilizing the structural and in inducing electronic pairing.

Fig. 5-7a shows the resistance, R(T), of a particular $Bi_2Sr_2CaCu_2O_8$ crystal for three different oxygen configurations. After the first oxygen anneal (10hr at 650°C with a 5hr ramp to room temperature in flowing oxygen), which produces a sharp $T_c$ of 84K, the sample is vacuum annealed (10hr at 550°C with a 5hr ramp to room temperature in <3millitorr of oxygen). The room temperature resistance climbs from 0.6

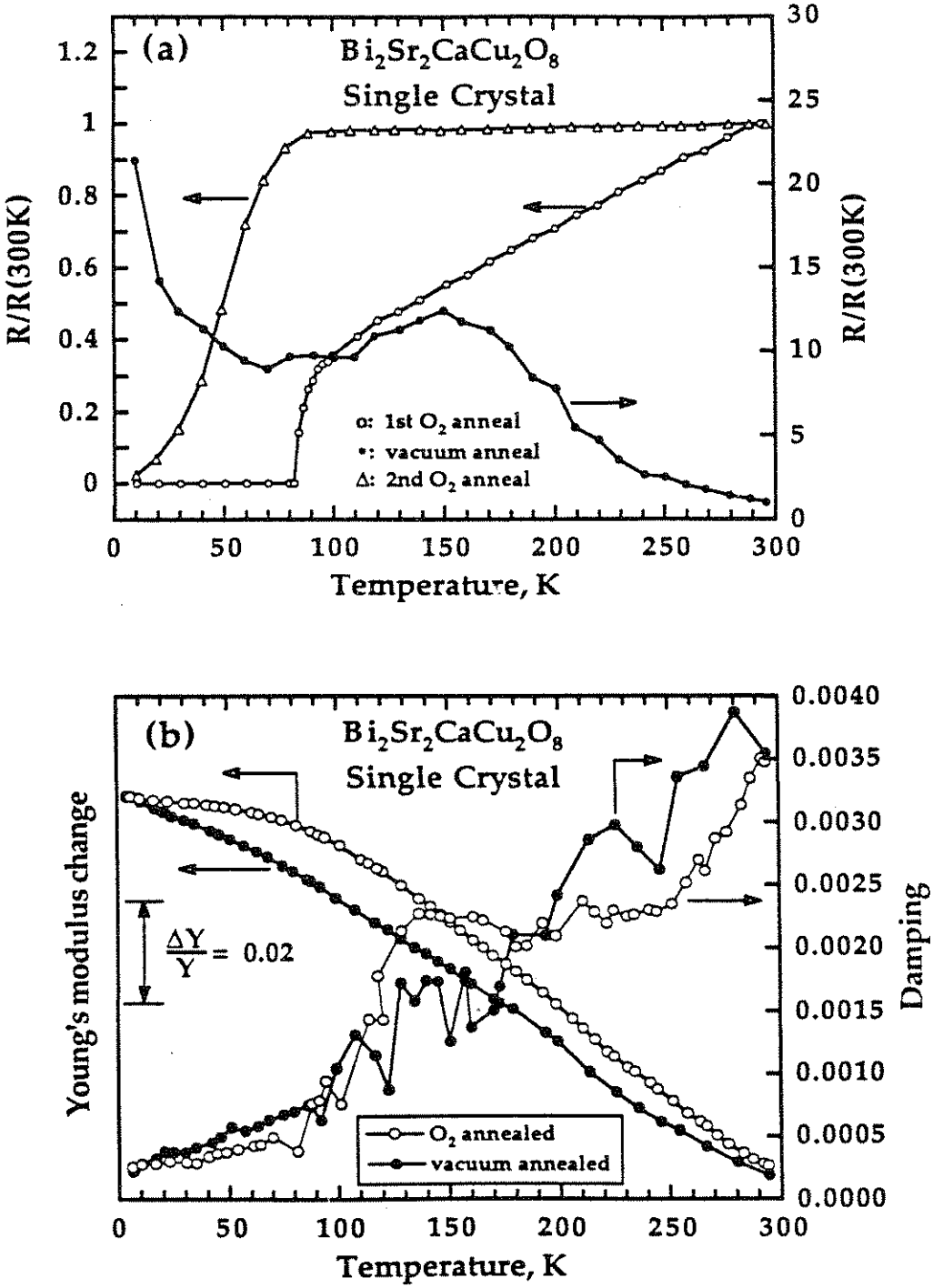


Fig. 5-7. (a) Resistance (R) normalized to R(300K) as a function of temperature for three different oxygen configurations of one $Bi_2Sr_2CaCu_2O_8$ crystal. A more complete description of the annealing procedures is included in the text. (b) Young's modulus and damping for two different oxygen configurations of one $Bi_2Sr_2CaCu_2O_8$ crystal. The anneals are identical to the first two resistance anneals. No Young's modulus experiment was performed for the 2nd $O_2$ anneal.

Ω to 1 MΩ and the crystal has a faint brownish cast. R(T) is now semi-conductor-like and shows no evidence of superconductivity for T>4K. Reannealing the crystal in oxygen (10hr at 650°C with a 5hr ramp to room temperature in flowing oxygen) reduces the room temperature resistance to 30 Ω with superconductivity evident at 60K.

Several crystals were annealed under identical conditions to study the structural effects of oxygen removal. As noted in a previous study[76], de-oxygenated $Bi_2Sr_2CaCu_2O_8$ shows a greater tendency to delaminate (i.e. cleave along the a-b plane). This is apparent in vibrating reed experiments by large and irreproducible changes in resonant frequency, $f_o$, and damping. At times, these changes are preceded by a temperature range in which $f_o(T)$ is reproducible, though anomalous (large $|\partial f_o/\partial T|$). Cleaner $f_o(T)$ are produced by removing portions of the crystal which appear weakly attached, though anomalous behavior is still seen. One de-oxygenated crystal, annealed under identical conditions as the resistive sample, shows reproducible behavior in $f_o(T)$. Fig. 5-7b plots Y and damping as functions of T for this crystal. The sample had dimensions 1.4 x 0.3 x 0.01 $mm^3$ and is affixed to a Cu support plate with silver paint as outlined in Chapter 4.

After the vacuum anneal, the room temperature $f_o$ dropped 30% to 2.63 kHz. The total Young's modulus change between 4.2K and 300K remains identical; however, no longer is any freezing out of phonon modes evident at low temperatures. $\partial Y/\partial T$ remains non-zero down to 4.2K, reminiscent of Y(T) for glasses.[79, 80] Indeed, Anderson and Bömmel[81] have shown that a distribution of structural relaxations causes similar Y(T) for fused silica. This suggests that the oxygen vacancies are

disordered and there exists a broad distribution of activation energies for vacancy movement. The low temperature (T<20K) increase in Y(T) seen in some oxygenated samples may arise from the same mechanism. The damping curve of the vacuum annealed sample shows substantial scatter, perhaps caused by partial delaminations. The 140K damping peak is no longer evident though there appears to be new peaks at 210K and 270K. At low temperatures, the damping is more temperature dependent than for the $O_2$ anneal, again suggestive of a distribution of low energy relaxation phenomena.[81]

In summary, annealing conditions play an important role in determining the elastic properties of $Bi_2Sr_2CaCu_2O_8$ crystals. Vacuum annealing induces a glassy distribution of oxygen vacancies and alters the relaxation mechanisms available to the superconducting material. Further measurements are necessary to confirm these results.

### 5.6 Young's modulus studies of single crystal Tl-Ba-Ca-Cu-O

Young's modulus measurements[18, 37] on single crystal HTSC's have revealed remarkable stress dependence of $T_c$ for $YBa_2Cu_3O_7$ and surprisingly little stress dependence for $Bi_2Sr_2CaCu_2O_8$. It is conceivable that as the structures become more tetragonal, the dependence of $T_c$ on stress along the a-b plane is reduced and there is less interplay between the superconducting state and the underlying crystal structure. An obvious test of this hypothesis is the determination of the elastic properties of the Tl-Ba-Ca-Cu-O based superconductors. This section describes a vibrating reed study on single crystals of Tl-Ba-Ca-Cu-O grown from an off-stoichiometry melt (cation ratios of 2:1:1:2) by John Wei and Don Morris at

Lawrence Berkeley Laboratory. Typical crystal dimensions are 0.75 x 0.25 x 0.05 $mm^3$ with $T_c$~115K determined resistively and magnetically. Tl-Ba-Ca-Cu-O sample composition rarely correspond with the initial composition.[82, 83] An accurate phase determination is hindered by there being a variety of phases in the Tl-Ba-Ca-Cu-O system with similar lattice constants and each showing a range of $T_c$'s. Indeed, even with "single crystals," there can be substantial intergrowth of additional phases.[83] Preliminary studies at Lawrence Berkeley Laboratory suggest that the crystal is $Tl_3Ba_2Ca_2Cu_3O_{10}$. Magnetic susceptibility studies on crystals from the same growth indicate a small fraction (~5%) of a secondary superconducting phase with $T_c$~100K — most likely $Tl_2BaCa_2Cu_2O_8$.[51] A load mass was attached at one end of the sample to reduce the resonance frequency. Flexural modes were excited capacitively and damping, $\delta$, is calculated from 1/Q.

Fig. 5-8 shows the Young's modulus and damping as functions of temperature for one crystal. Between 20K and 300K, Y decreases by 11%, similar to $YBa_2Cu_3O_7$. The anomaly at 230K in Y and $\delta$ arises from a spurious resonance interacting with the sample resonance and does not reflect the true Young's modulus. A small upturn in Y is visible at 170K and accompanies a peak in the damping. A similar feature occurs at 130K in $Bi_2Sr_2CaCu_2O_8$. An additional damping peak, without an apparent feature in Y, occurs at 80K. Interestingly, Y does not show a strong downward curvature at low T. As for de-oxygenated $Bi_2Sr_2CaCu_2O_8$, there appears to be a distribution of low energy relaxations, most likely arising from Cu magnetic interactions or the movement of oxygen or thallium vacancies or interstitials. Low temperature specific heat data[51] for crystals

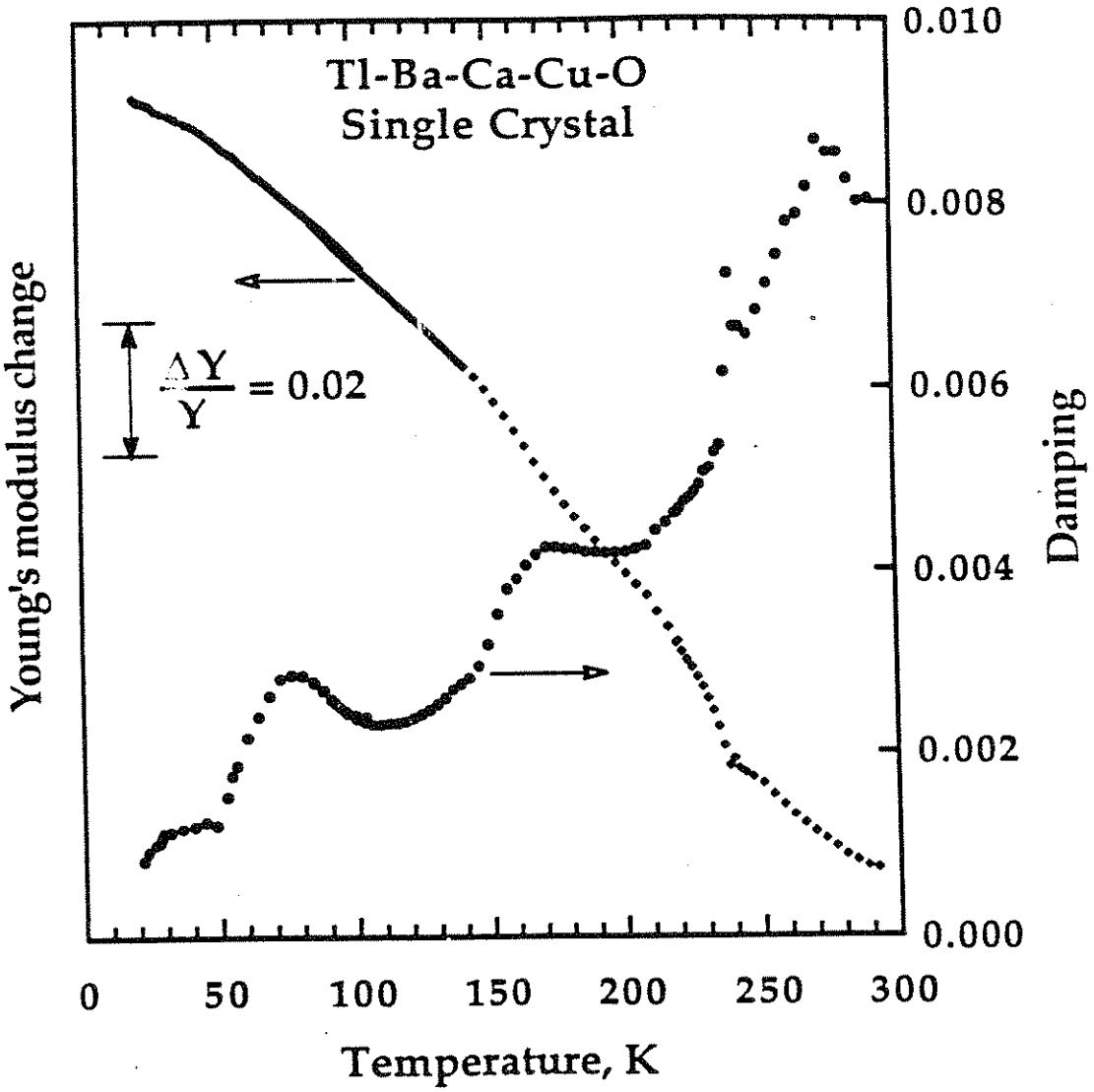


Fig. 5-8. Young's modulus and damping as functions of temperature for single crystal Tl-Ba-Ca-Cu-O.

grown similarly show a 1/T dependence for T< 15K, a characteristic of spin glasses and other two-level systems. The presence of such defects, because they reduce the number of free carriers, explains the reduced $T_c$. Y exhibits a small upward curvature at 108K associated with the superconducting phase transition.

Fig. 5-9a plots the four-probe sample resistance and dc susceptibility near $T_c$ (~110K). Fig. 5-9b shows Y(T) in this same region; the upper curve represents the true Y(T) while the lower curve has a linear background removed. A small softening of $\Delta Y/Y \sim -3 \times 10^{-5}$ is evident near the transition; however, further studies of crystals with sharper $T_c$'s are required to confirm this value. Assuming the $Y \sim 1 \times 10^{12}$ dynes/cm$^2$ and using $\Delta C_p/T_c = 20$ mJ/mole·K$^2$ (ref. 84), we find $\partial T_c/\partial \sigma_i \equiv 0.2$ K/kbar. The values of $\Delta C_p/T_c$ for Tl-Ba-Ca-Cu-O are significantly affected by composition an ' range from 20 mJ/mole·K$^2$ (ref. 84) to 50 mJ/mole·K$^2$ (ref. 52). The predicted values of $\partial T_c/\partial \sigma_i$ and $\partial^2 T_c/\partial \sigma_i^2$ will scale accordingly. Unlike $Bi_2Sr_2CaCu_2O_8$, there is a clear slope change associated with the phase transition, $\Delta(\partial \ln Y/\partial T) = -1.06 \times 10^{-4}$. As for $YBa_2Cu_3O_7$, the small value of $\Delta Y/Y$ ensures that the second term in the equation relating $\Delta(\partial \ln Y/\partial T)$ and $\partial^2 T_c/\partial \sigma_i^2$ (eqtn. 5.4) is too small to explain the large slope change associated with the transition. Again ignoring terms arising from anharmonicity and Fermi energy effects, we find $\partial^2 T_c/\partial \sigma_i^2 = 0.14$ K/kbar$^2$. The value of $\partial T_c/\partial \sigma_i$ is nearly identical to the value of $\partial T_c/\partial P$ determined from pressure studies by Shun-hui *et al.*[85] Interestingly, as for $YBa_2Cu_3O_7$, no quadratic dependence of $T_c$ on P is seen in the range 0-8 kbar; however few data points were taken at low P (<2kbar).

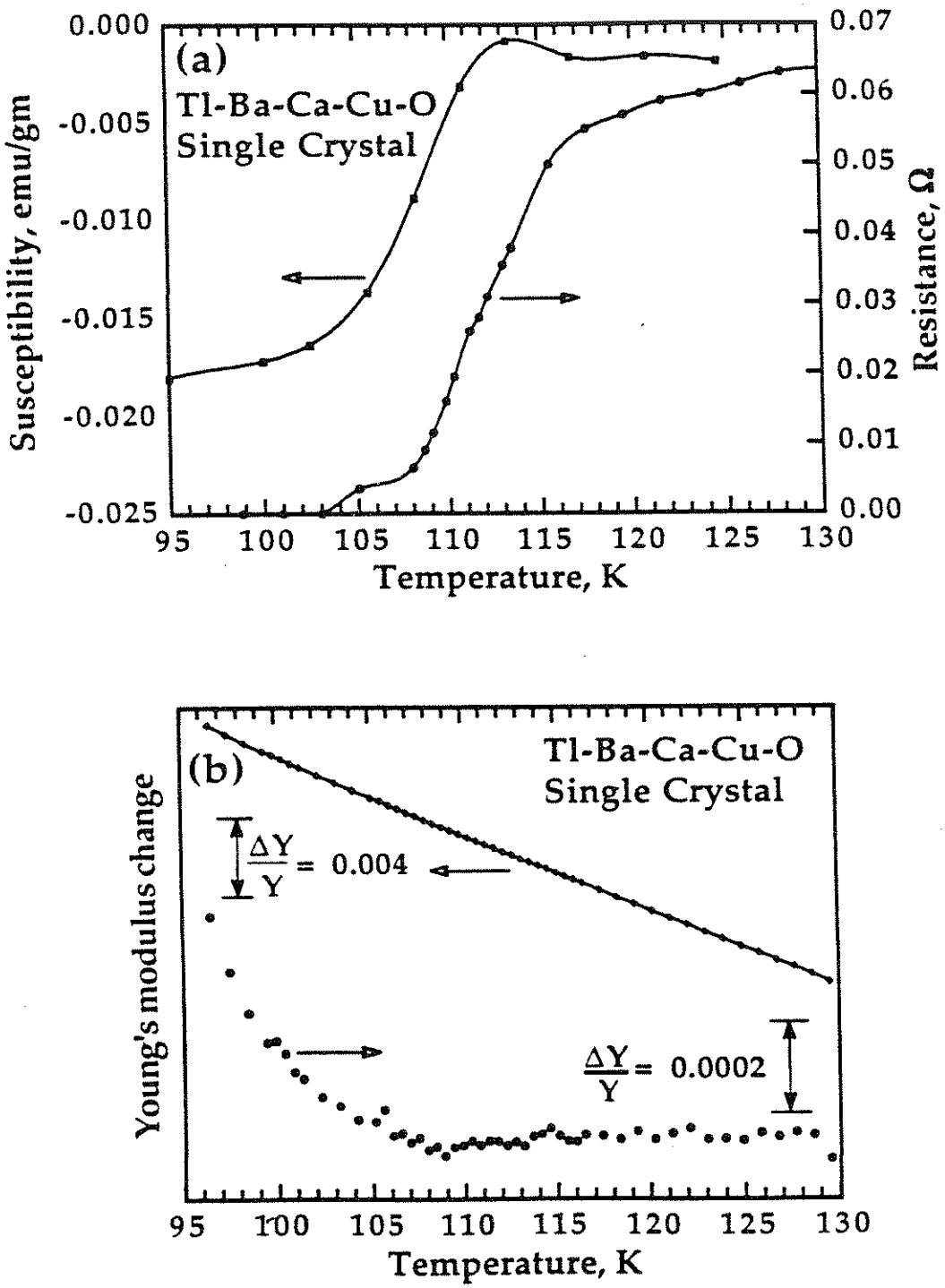


Fig. 5-9. (a) Magnetic susceptibility and resistance as functions of temperature for single crystal Tl-Ba-Ca-Cu-O. (b) Young's modulus as a function of temperature for single crystal Tl-Ba-Ca-Cu-O. The lower curve has been adjusted by subtracting linear background (fitted between 120K and 130K) from the data to magnify any anomalies in Y.

The elastic properties of single crystal Tl-Ba-Ca-Cu-O exhibit features similar to both $YBa_2Cu_3O_7$ and $Bi_2Sr_2CaCu_2O_8$. Relaxation peaks occur at 170K and 80K. $\partial^2T_c/\partial\sigma_i^2$ for $\sigma_i$ along the a-b plane is predicted to be quite large for this compound, similar to $YBa_2Cu_3O_7$.

### 5.7 Summary of results

The Young's modulus of single crystal $YBa_2Cu_3O_7$ has been measured and compared to the polycrystalline result. The expected elastic anomaly at $T_c$ has been resolved for the first time, and it is consistent with thermodynamic predictions. Intergrain coupling in polycrystalline samples does not appear to be the sole source of the lattice stiffening below $T_c$. Indeed, the hardening is demonstrated to arise from a change in $\partial Y/\partial T$ associated with the superconducting phase transition. Similar hardening is seen in Tl-Ba-Ca-Cu-O. The large magnitude of the predicted $\partial^2T_c/\partial\sigma_i^2$ from these anomalies suggests that a structural softening may be coupled with the superconducting transition. However, no anomaly in Y or $\partial Y/\partial T$ occurs for $Bi_2Sr_2CaCu_2O_8$ for stresses along the a-b plane. Thus, for a common structural transition to occur in these materials, the softening can not couple directly to $(c_{11} - c_{12})$; otherwise it should be equally visible in all materials. It is possible that the more two-dimensional morphology of $Bi_2Sr_2CaCu_2O_8$ reduces the effect of a structural softening in $c_{13}$ or $c_{33}$. Since only low P or $\sigma$ experiments[40, 41] (P, $\sigma$<2kbar) show a large quadratic dependence of $T_c$ on $\sigma$, it would be interesting to do more careful pressure effect measurements in this region. A summary of the values of $\Delta Y/Y$, $\Delta(\partial \ln Y/\partial T)$, $|\partial T_c/\partial\sigma_i|$, and $\partial^2T_c/\partial\sigma_i^2$ is included in Table 5.1.

| Parameter | $YBa_2Cu_3O_7$ | $Bi_2Sr_2CaCu_2O_8$ | $Tl_2Ba_2Ca_2Cu_3O_{10}$ |
|---|---|---|---|
| a (Å) | 3.82 [69] | 5.41 [82] | 5.399 [82] |
| b (Å) | 3.89 [69] | 5.44 [82] | 5.399 [82] |
| c (Å) | 11.68 [69] | 30.89 [82] | 36.25 [82] |
| Form. weight (amu) | 666 | 888.4 | 1318.6 |
| Vol/mole ($cm^3$) | 104.5 | 136.4 | 264.16 |
| $\Delta C_p/T_c$ ($mJ/moleK^2$) | 55 [30] | 25.8 [52] | 20 [84] |
| Y (dynes/$cm^2$) | $2.2 \times 10^{12}$ [32] | $6.7 \times 10^{11}$ [48] | $\sim 1 \times 10^{12}$ |
| $\Delta Y/Y$ | $-9 \times 10^{-5}$ | $< 1 \times 10^{-5}$ | $3 \times 10^{-5}$ |
| $\Delta(\partial \ln Y/\partial T)$ ($K^{-1}$) | $-1.3 \times 10^{-4}$ | $> -8.3 \times 10^{-7}$ $< 4.0 \times 10^{-6}$ | $-1.1 \times 10^{-4}$ |
| $\lvert\partial T_c/\partial \sigma_i\rvert$ (K/kbar) | 0.09 | < 0.09 | 0.2 |
| $\partial^2 T_c/\partial \sigma_i^2$ ($K/kbar^2$) | +.01 | $> -3.0 \times 10^{-3}$ $< 6.5 \times 10^{-4}$ | + 0.13 |
| $\partial T_c/\partial P$ (K/kbar) | 0.07 [31] | 0.13 [53] | 0.2 [85] |

Table 5.1. Various thermodynamic quantities associated with the superconducting phase transition. References for quantities not determined in this experiment are noted as [Ref.].

Altering the superconducting properties of particular materials (doping $YBa_2Cu_3O_7$ with Al or removing oxygen from $Bi_2Sr_2CaCu_2O_8$) causes substantial changes in the Young's modulus and damping. Al-doped $YBa_2Cu_3O_7$ shows no change in $\partial Y/\partial T$ at $T_c$ and removing oxygen from $Bi_2Sr_2CaCu_2O_8$ causes a Y(T) with no low temperature knee, presumably an effect of a broad distribution of oxygen vacancy relaxation modes. A more extensive study is required to determine which effects are directly related to the superconductivity in these materials.

## References


1. J. G. Bednorz and K. A. Müller, Z. Phys. B **64**, 189 (1986).

2. M. K. Wu, J. R. Ashburn, C. J. Torng, P. H. Hor, R. L. Meng, L. Gao, Z. J. Huang, Y. Q. Wang and C. W. Chu, Phys. Rev. Lett. **58**, 908 (1987).

3. C. Michel, M. Hervieu, M. M. Borel, A. Grandin, F. Deslandes, J. Provost and B. Raveau, Z. Phys. **B68**, 421 (1987).

4. H. Maeda, Y. Tanaka, M. Fukuton and T. Asano, Appl. Phys. Lett. **27**, L209 (1988).

5. Z. Z. Sheng and A. M. Hermann, Nature **332**, 55 (1988).

6. Z. Z. Sheng and A. M. Hermann, Nature **332**, 138 (1988).

7. L. C. Bourne, M. F. Crommie, A. Zettl, Hans-Conrad zur Loye, S. W. Keller, K. L. Leary, Angelica M. Stacy and Don Morris, Phys. Rev. Lett. **58**, 2337 (1987).

8. L. C. Bourne, A. Zettl, T. W. Barbee III and Marvin L. Cohen, Phys. Rev. **B36**, 3990 (1987).

9. B. Batlogg, R. J. Cava, A. Jayaraman, R. B. van Dover, G. A. Koruouklis, S. Sunshine, D. W. Murphy, L. W. Rupp, H. S. Chen, A. White, K. T. Short, A. M. Mujsce and E. A. Rietman, Phys. Rev. Lett. **58**, 2333 (1987); **60**, 754 (1988); .

10. Tanya A. Faltens, William K. Ham, Steven W. Keller, Kevin J. Leary, James N. Michaels, Angelica M. Stacy, Hans-Conrad zur Loye, Donald E. Morris, T. W. Barbee III, L. C. Bourne, Marvin L. Cohen, S. Hoen and A. Zettl, Phys. Rev. Lett. **59**, 915 (1987).

11. N. M. Plakida, Europhys. Lett. **4**, 1309 (1987).

12. Vincent H. Crespi and Marvin L. Cohen, Phys. Rev. **B44**, 4712 (1991).

13. Vincent H. Crespi and Marvin L. Cohen, (submitted to Phys. Rev. B).

14. L. C. Bourne, Marvin L. Cohen, William N. Creager, Michael F. Crommie, Angelica M. Stacy and A. Zettl, Phys. Lett. **A120**, 494 (1987).

15. L. R. Testardi, in *Physical Acoustics*, W. P. Mason and R. N. Thurston ed., (Academic, New York, 1973), p. 193.

16. L. R. Testardi, Phys. Rev. **B3**, 95 (1971).

17. M. Barmatz, L. R. Testardi and F. J. DiSalvo, Phys. Rev. **B12**, 4367 (1975).

18. S. Hoen, L. C. Bourne, Choon M. Kim and A. Zettl, Phys. Rev. **B38**, 11949 (1988).

19. S. Bhattacharya, M. J. Higgins, D. C. Johnston, A. J. Jacobson, J. P. Stokes, D. P. Goshorn and J. T. Lewandowski, Phys. Rev. Lett. **60**, 1181 (1988).

20. D. J. Bishop, A. P. Ramirez, P. L. Gammel, B. Batlogg, E. A. Rietman, R. J. Cava and A. J. Millis, Phys. Rev. **B36**, 2408 (1987).

21. G. Cannelli, R. Cantelli, F. Cordero, G. A. Costa, M. Ferretti and G. L. Olcese, Phys. Rev. **B36**, 8907 (1987).

22. G. Cannelli, R. Cantelli and F. Cordero, Phys. Rev. **B38**, 7200 (1988).

23. C. Durán, P. Esquinazi, C. Fainstein and M. Núñez Regueiro, Solid State Commun. **65**, 957 (1988).

24. H. M. Ledbetter, M. W. Austin, S. A. Kim, T. Datta and C. E. Violet, J. Mater. Res. **2**, 790 (1987).

25. S. Hoen, W. N. Creager, L. C. Bourne, M. F. Crommie, T. W. Barbee III, Marvin L. Cohen, A. Zettl, Luis Bernardez and John Kinney, Phys. Rev. **B39**, 2269 (1989).

26. T. Tiedje, R. R. Haering and W. N. Hardy, J. Acoust. Soc. Am. **65**, 1171 (1979).

27. R. C. Lacoe, Ph. D. Thesis, University of California, Los Angeles (1983).

28. L. R. Testardi, Phys. Rev. **B12**, 3849 (1975).

29. A. J. Millis and K. M. Rabe, Phys. Rev. **B38**, 8908 (1988).

30. M. V. Nevitt, G. W. Crabtree and T. E. Klippert, Phys. Rev. **B36**, 2398 (1987); S. E. Inderhees, M. B. Salamon, T. A. Friedmann and D. M. Ginsberg, Phys. Rev. **B36**, 2401 (1987);.

31. J. E. Schirber, D. S. Ginley, E. L. Venturini and B. Morosin, Phys. Rev. **B35**, 8709 (1987).

32. X. D. Shi, R. C. Yu, Z. Z. Wang, N. P. Ong and P. M. Chaikin, Phys. Rev. **B39**, 827 (1989).

33. X.-D. Xiang, J. W. Brill, L. W. DeLong, L. C. Bourne, A. Zettl, Jonathan C. Jones and L. A. Rice, Solid State Comm. **65**, 1073 (1988).

34. S. Hoen, L. C. Bourne, Choon M. Kim and A. Zettl, Bull. Am. Phys. Soc. **33**, 513 (1988).

35. H. A. Borges, R. Kwok, J. D. Thompson, G. L. Wells, J. L. Smith, Z. Fisk and D. E. Peterson, Phys. Rev. **B36**, 2404 (1987).

36. A. Driessen, R. Griessen, N. Koeman, E. Salomons, R. Grouwer, D. G. de Groot, K. heeck, H. Hemmes and J. Rector, Phys. Rev. **B36**, 5602 (1987).

37. X.-D. Xiang, M. Chung, J. W. Brill, S. Hoen, P. Pinsukanjana and A. Zettl, Solid State Commun. **69**, 833 (1989).

38. Michael Tinkham, *Introduction to Superconductivity* (Robert E. Krieger, Malabar, Florida, 1975).

39. A. Junod, D. Eckert, T. Graf, G. Triscone and J. Muller, submitted to *Proc. Materials and Mechanisms of Superconductivity: High-Temperature Superconductivity* (Stanford University, Palo Alto, CA, 1989).

40. M. F. Crommie, Amy Y. Liu, A. Zettl, Marvin L. Cohen, P. Parilla, M. F. Hundley, W. N. Creager, S. Hoen and M. S. Sherwin, Phys. Rev. **B39**, 4231 (1989).

41. P. H. Hor, L. Gao, R. L. Meng, Z. J. Huang, Y. Q. Wang, K. Forster, J. Vassilious, C. W. Chu, M. K. Wu, J. R. Ashburn and C. J. Torng, Phys. Rev. Lett. **58**, 911 (1987).

42. Göran Grimvall, *Thermophysical Properties of Materials* (North-Holland, Amsterdam, 1986).

43. P. M. Horn, D. T. Keane, G. A. Held, J. L. Jordan-Sweet, D. L. Kaiser, F. Holtzberg and T. M. Rice, Phys. Rev. Lett. **59**, 2772 (1987).

44. E. Goens, Ann. Phys. (N.Y.) **11**, 649 (1931).

45. M. Saint-Paul, J. L. Tholence, H. Noël, J. C. Levet, M. Potel, P. Gougeon and J. J. Capponi, Solid State Comm. **66**, 641 (1988).

46. W. E. Pickett, H. Krakauer, R. E. Cohen and D. J. Singh, Science **255**, 46 (1992).

47. M. Saint-Paul, J. L. Tholence, H. Noël, J. C. Levet, M. Potel and P. Gougeon, Physica C **166**, 405 (1990).

48. M. Boekholt, J. V. Harzer, B. Hillebrands and G. Güntherodt, Physica C **179**, 101 (1991).

49. Jr. J. B. Wachtman, W. E. Tefft, Jr. D. G. Lam and C. S. Apstein, Phys. Rev. **122**, 1754 (1961).

50. R. A. Fisher, S. Kim, S. E. Lacy, N. E. Phillips, D. E. Morris, A. G. Markelz, J. Y. T. Wei and D. S. Ginley, Phys. Rev. **B38**, 11942 (1988).

51. J. S. Urbach, D. B. Mitzi, A. Kapitulnik, J. Y. T. Wei and D. E. Morris, Phys. Rev. **B39**, 12391 (1989).

52. A. K. Bandyopadhyay, P. Maruthikumar, G. L. Bhalla, S. K. Agarwal and A. V. Narlikar, Physica C **165**, 29 (1990).

53. K. Kumagai and M. Kurisu, **27**, L1029 (1988).

54. Jian Dong, Tingzhang Deng, Fengying Li and Yushu Yao, Phys. Rev. **B42**, 301 (1990).

55. Lin Sihan, He Yusheng, Wei Chongde and Shen Zhaohui, Supercond. Sci. Technol. **2**, 145 (1989).

56. Ye-Ning Wang, Jin Wu, Hui-Min Shen, Jin-Song Zhu, Xiao-Hua Chen, Yi-Feng Yan and Zhong-Xian Zhao, Phys. Rev. **B41**, 8981 (1990).

57. T. M. Tritt, M. Marone, Xin-Fen Chen, M. J. Skove, A. C. Ehrlich, G. X. Tessema, D. J. Gillespie, J. P. Franck and J. Jung, Physica C **178**, 296 (1991).

58. T. M. Tritt, M. Marone, A. C. Ehrlich, M. J. Skove, D. J. Gillespie, R. L. Jacobsen, G. X. Tessema, J. P. Franck and J. Jung, Phys. Rev. Lett. **68**, 2531 (1992).

59. Shen Huimin, Wang Yening, Zhang Zhifang, Zhang Shiyuan and Sun Linhai, J. Phys. C **20**, L889 (1987).

60. S-W. Cheong, M. F. Hundley, J. D. Thompson and Z. Fisk, Phys. Rev. **39**, 6567 (1989).

61. M. F. Hundley, J. D. Thompson, S-W. Cheong, Z. Fisk and J. E. Schirber, Phys. Rev. **B41**, 4062 (1990).

62. A. Migliori, William M. Visscher, S. E. Brown, Z. Fisk, S. -W. Cheong, B. Alten, E. T. Ahrens, D. A. Kubat-Martin, J. D. Maynard, Y. Huang, D. R. Kirk, K. A. Gillis, H. K. Kim and M. H. W. Chan, Phys. Rev. **B41**, 2098 (1990).

63. B. Andraka, U. Anlheim, J. S. Kim, G. Fraunberger, G. R. Stewart, B. Morosin, E. L. Venturini, D. S. Ginley and J. E. Schirber, Phys. Rev. **B42**, 10016 (1990).

64. C. Y. Chen, N. W. Preyer, P. J. Picone, M. A. Kastner, H. P. Jenssen, D. R. Gabbe, A. Cassanho and R. J. Birgeneau, Phys. Rev. Lett. **63**, 2307 (1989).

65. N. W. Preyer, R. J. Birgeneau, C. Y. Chen, D. R. Gabbe, H. P. Jenssen, M. A. Kastner, P. J. Picone and Tineke Thio, Phys. Rev. **B39**, 11563 (1989).

66. C. Y. Chen, R. J. Birgeneau, M. A. Kastner, N. W. Preyer and Tineke Thio, Phys. Rev. **B43**, 392 (1991).

67. R. J. Cava, B. Batlogg, C. H. Chen, E. A. Rietman, S. M. Zahurak and D. Werder, Nature **329**, 423 (1987).

68. R. Beyers, B. T. Ahn, G. Gorman, V. Y. Lee, S. S. P. Parkin, M. L. Ramirez, K. P. Roche, J. E. Vazquez, T. M. Gür and R. A. Huggins, Nature **340**, 619 (1989).

69. J. D. Jorgensen, B. W. Veal, A. P. Paulikas, L. J. Nowicki, G. W. Crabtree, H. Claus and W. K. Kwok, Phys. Rev. **B41**, 1863 (1990).

70. D. de Fontaine, G. Ceder and M. Asta, Nature **343**, 544 (1990).

71. G. Ceder, R. McCormack and D. de Fontaine, Phys. Rev. **B44**, 2377 (1991).

72. B. W. Neal, H. You, A. P. Paulikas, H. Shi, Y. Fang and J. W. Downey, Phys. Rev. **B42**, 4770 (1990).

73. R. McCormack, D. de Fontaine and G. Ceder, Phys. Rev. **B45**, 12976 (1992).

74. G. Briceno and A. Zettl, Phys. Rev. **B40**, 11352 (1989).

75. L. Forrò, J. R. Cooper, B. Leontic and B. Keszei, Europhys. Lett. **10**, 371 (1989).

76. M. F. Crommie and A. Zettl, Phys. Rev. **B41**, 10978 (1990).

77. M. F. Crommie, Amy Y. Liu, Marvin. L. Cohen and A. Zettl, Phys. Rev. B **41**, 2526 (1990).

78. L. Forrò and J. R. Cooper, Europhys. Lett. **11**, 55 (1990).

79. M. Barmatz and H. S. Chen, Phys. Rev. **B9**, 4073 (1974).

80. S. Hunklinger and M. v. Schickfus, in *Amorphous Solids: Low-Temperature Properties*, W. A. Phillips ed., (Springer-Verlag, Berlin, 1981), p. 81.

81. O. L. Anderson and H. E. Bömmel, J. Am. Ceram. Soc. **38**, 125 (1955).

82. R. M. Hazen, L. W. Finger, R. J. Angel, C. T. Prewitt, N. L. Ross, C. G. Hadidiacos, P. J. Heaney, D. R. Veblen, Z. Z. Sheng, A. El Ali and A. M. Hermann, Phys. Rev. Lett. **60**, 1657 (1988).

83. S. S. P. Parkin, V. Y. Lee, E. M. Engler, A. I. Nazzal, T. C. Huang, G. Gorman, R. Savoy and R. Beyers, Phys. Rev. Lett. **60**, 2539 (1988).

84. A. Junod, D. Eckert, G. Triscone, J. Muller and V. Y. Lee, submitted to *Proc. Materials and Mechanisms of Superconductivity: High-Temperature Superconductivity* (Stanford, Palo Alto, CA, 1989).

85. Han Shun-hui, Zhang Yu-lin, Han han and Liu Yong, Physica C **156**, 113 (1988).

# Chapter 6: Magneto-Elastic Properties of $NbSe_3$

## 6.1 Introduction

Similar to high-temperature superconductors, charge-density wave (CDW) materials exhibit low-dimensional electron systems with strong electron-phonon coupling. However, in these materials, the Fermi surface electrons condense not to a superconducting state, but to a charge-density wave state in which the electron density is modulated at a wavevector twice the Fermi wavevector ($k_F$). This transition, the Peierls transition, is accompanied by a softening of an optical phonon mode at the wavevector $k_F$ and a static displacement of the underlying atoms at $2k_F$.

Elastic measurements have played a vital role in probing the CDW condensate. In the region of the Peierls transition ($T_p$), both the Young's modulus (Y) and damping ($\delta$) exhibit anomalous behavior and Y hardens for $T < T_p$.[1] Brill *et al.*,[2] using a vibrating reed technique to measure Y, have shown that depinning the CDW causes Y to soften by an amount, $Y_{CDW}$, approximately equal to the amount of hardening associated with $T_p$. These results have been explained both phenomenologically by describing the CDW as a separate entity with its own associated spring constant[3] and microscopically by considering the loss of free carrier screening which occurs as they condense into the CDW.[4] However, recent tensile measurements[5] at larger stresses, have found no softening in Y at the depinning threshold ($E_T$). The nature of the coupling between the CDW and the lattice remains an open question.

$NbSe_3$ is a quasi-one-dimensional CDW material comprised of bi-pyramidal units of a single Nb atom bound to 6 chalcongenides, as shown

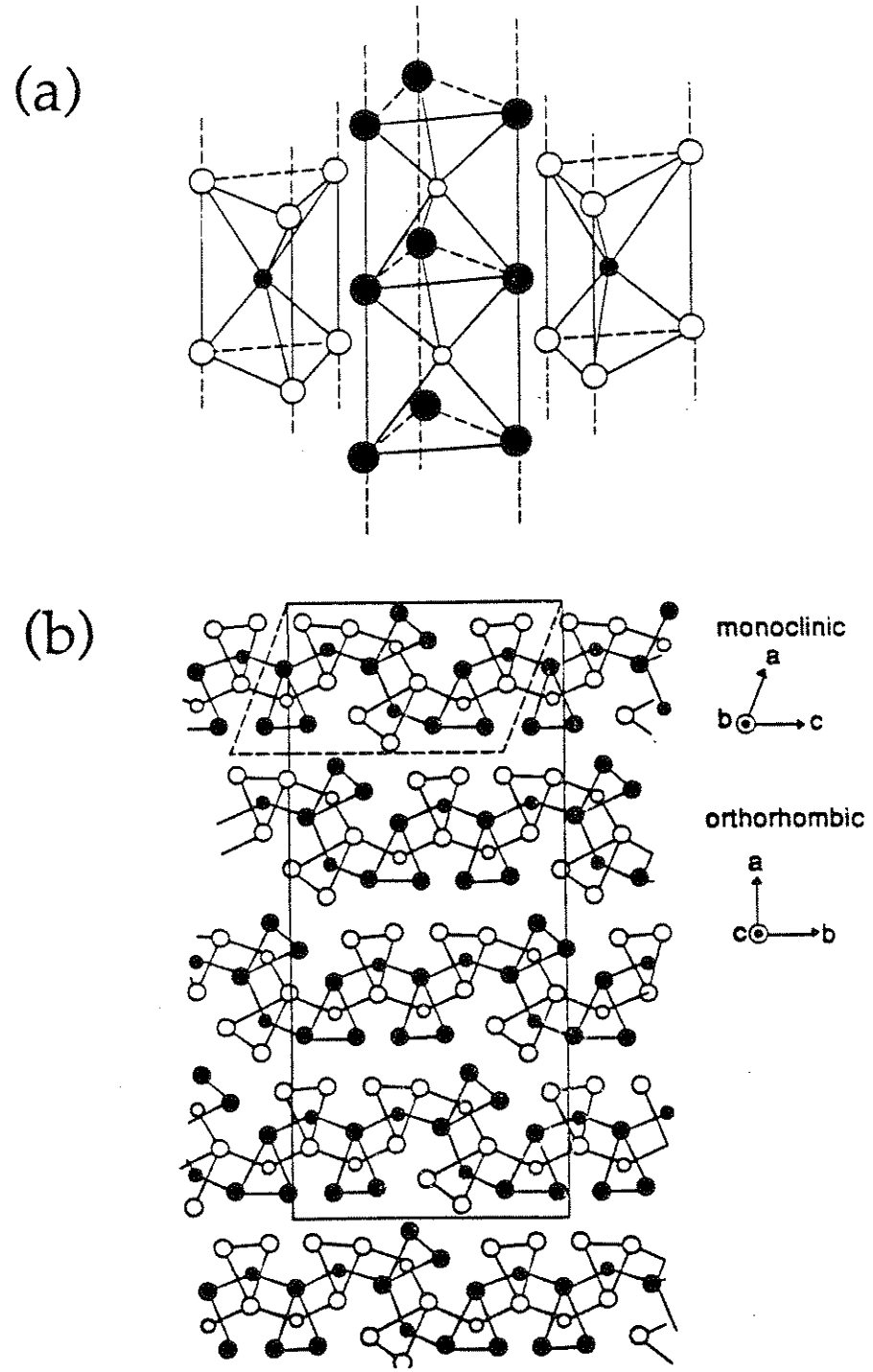


Fig. 6-1. (a) Schematic of chain structure for $MX_3$ (M=Ta, Nb; X=S, Se). The M atoms are bound to 6 X atoms. The fill pattern is a visual aid showing which atoms form interchain bonds. (b) A view parallel to the chain axis of the monoclinic ($NbSe_3$ or $TaS_3$) and orthorhombic ($TaS_3$) crystal structures. The solid and dashed outlines are the orthorhombic and monoclinic unit cells, respectively. These figures are adapted from Ref. 6.

in Fig. 6-1a.[6] These pyramids form long chains with relatively weak interchain bonds and electric conduction is largely confined to the chain direction. The crystal structure for $NbSe_3$, shown in Fig. 6-1b is monoclinic with 6 chains per unit cell. The orthorhombic structure describes the similar material $TaS_3$.

$NbSe_3$ undergoes two Peierls transitions, one at 144K ($T_1$) and one at 59K ($T_2$), and exhibits interesting magnetic and elastic properties. For temperatures below the second Peierls transition, magneto-resistance[7] and narrow band noise[8, 9] studies indicate magnetically induced carrier conversion from the conduction band into the CDW condensate. From the mean field theory of Maki and Virosztek,[4] for which $Y_{CDW}$ scales as the density of carriers condensed in the CDW, we expect an increase in Y to occur with the application of a magnetic field. Parker *et al.*,[10] in a recent magneto-resistance study, suggest a magnetically induced phase transition at 30K. Their data, depicted in Fig. 6-2, show a huge increase in resistance with applied field centered at 30K. Young's modulus studies are an extremely sensitive tool for investigating the existence and thermodynamics of phase transitions.[11, 12]

We clearly resolve the fluctuation anomalies in Y and $\delta$ at $T_1$ and in Y at $T_2$. We apply a reduced temperature analysis of the fluctuation region around $T_1$ to determine the dimensionality of this transition. For T<100K, we see anomalous magnetically induced softening of Y which is nearly temperature independent. There is some evidence for magnetically induced elastic stiffening for $T<T_1$, but no evidence of an additional phase transition at 30K. The remainder of this chapter is organized as follows. Sect. 6.2 outlines our experimental method. Sect. 6.3 describes and

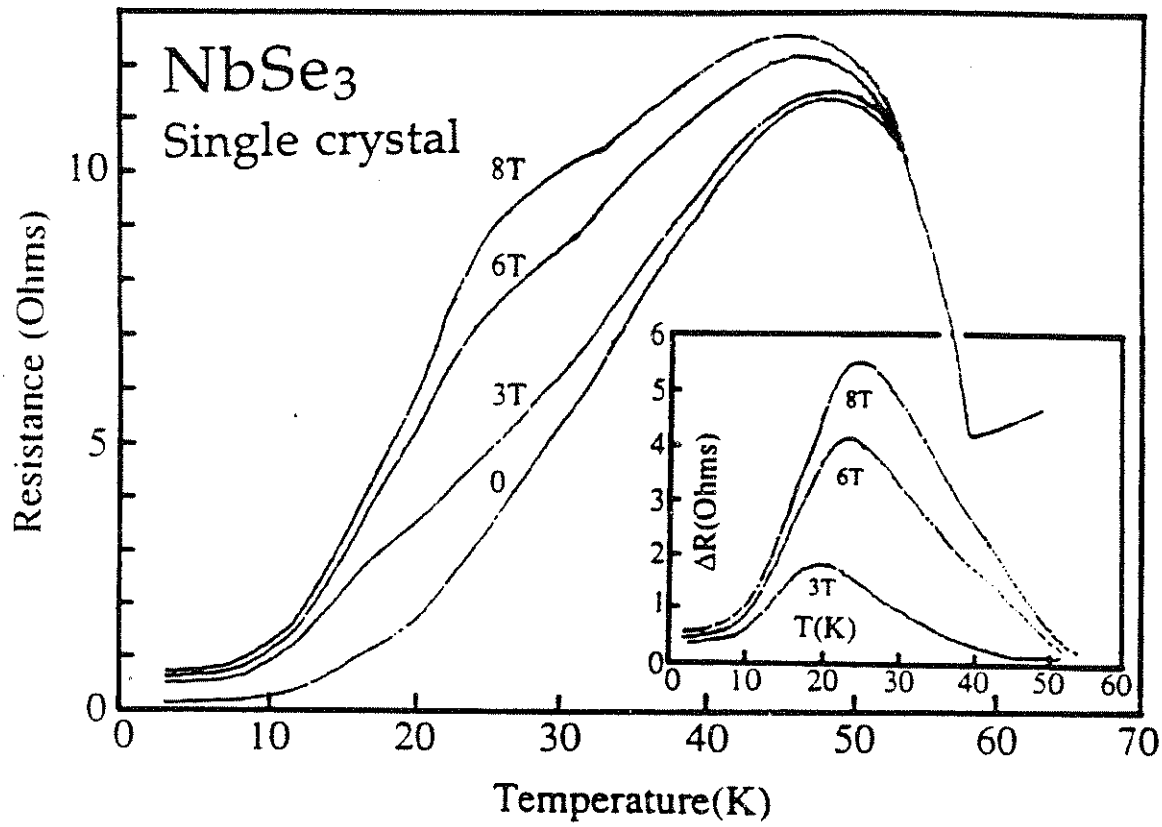


Fig. 6-2. Magnetic field dependence of sample resistance (R) vs temperature for single crystal $NbSe_3$, from Ref. 10. The inset shows $\Delta R$ ($\equiv R(H)-R(H=0)$ as a function of temperature.

discusses our Young's modulus results for the upper and lower CDW transitions. Sect. 6.4 presents and discusses our results for magnetic field effects on Y. A conclusion follows in Sect. 6.5.

## 6.2 Experimental method

Single crystals of $NbSe_3$ were prepared using vapor transport and high purity starting compounds. Y and $\delta$ are determined as functions of temperature and magnetic field using a modified vibrating reed technique described in Chapt. 4. Flexural vibrations are excited with a piezo-electric transducer (Stavely-EBL Division, lead zirconate Navy Channel 5a) and sample displacements are detected with an rf capacitance method.[13] Changes in the resonance frequency, $f_o$, are related to Y by $\Delta Y/Y = 2\Delta f_o/f_o$, and changes in $\delta$ are determined from the reciprocal of Q ($\equiv f_o/\text{FWHM}$ where FWHM is the full-width at half-maximum of the resonance). Over small temperature ranges, Q is proportional to the resonance vibration amplitude since the amplitude of the piezo-electric oscillation and the coupling between the sample and the rf pickup change slowly with temperature. Samples are cooled in ~ 1 torr of He which acts as an exchange gas and reduces the resonance Q to yield reasonable measurement time scales.

This experimental configuration is sensitive to Young's modulus changes of 0.1 ppm. For the investigation of the subtle effects of magnetic fields, we are limited not by the excitation and detection apparatus, but by the structural stability of sample and the mechanical coupling of the sample to the rf plate on the free end of the piezo-electric. Though we examined several crystals, we obtained best results when the free end of

the beam was the uncut, as grown, end of a crystal. Because the silver paint used to make electrical contact with the rf plate shows some cracking upon cooling, we use stycast to provide the mechanical contact to the crystal.

### 6.3 Young's modulus near the upper and lower Peierls transitions

For our best sample (dimensions = 3.0 x 0.02 x ~0.005 $mm^3$), we find the ratios of the fundamental to the first four harmonics to lie within .1% of those for a perfect cantilever beam (1 : 6.267 : 17.55 : 34.39 : 56.84). Unless otherwise noted the results describe the magnetic and temperature dependence of the first harmonic (3521 Hz at 295K). Between 4.2K and 300K, this sample shows a 4.3% decrease in Y. At room temperature, Q ~ 600, independent of the He pressure, and at 4.2K, Q ~ 2000 and depends on the He pressure. In vacuum at 4.2K, Q ~ $10^5$.

Fig. 6-3 shows Y and $\delta$ near $T_1$. Fluctuation anomalies are clearly present in both quantities, and the reduced Young's modulus anomaly $(Y-Y_0(T))/Y_0$ is plotted against the reduced temperature $\tau = (T-T_p)/T_p$ in Fig. 6-4. A linear form for $Y_0(T)$ does not give results independent of the range over which $Y_0$ was fit. We find consistent results using two quadratic fits extending from 10K to 50K above and below the transition respectively. The first and third harmonics show similar temperature dependences. In the range $\ln|\tau| = -3.5$ to -5, the curves have a slope $\cong -1.1$ for $\tau>0$ and $\cong -0.74$ for $\tau<0$.

The results of the reduced temperature plot, Fig. 6-4, are inconclusive in demonstrating scaling behavior of Y at $T_1$. Using mean field theory with non-linear electron dispersion, Nakane[14] predicted that $\Delta Y/Y$ should

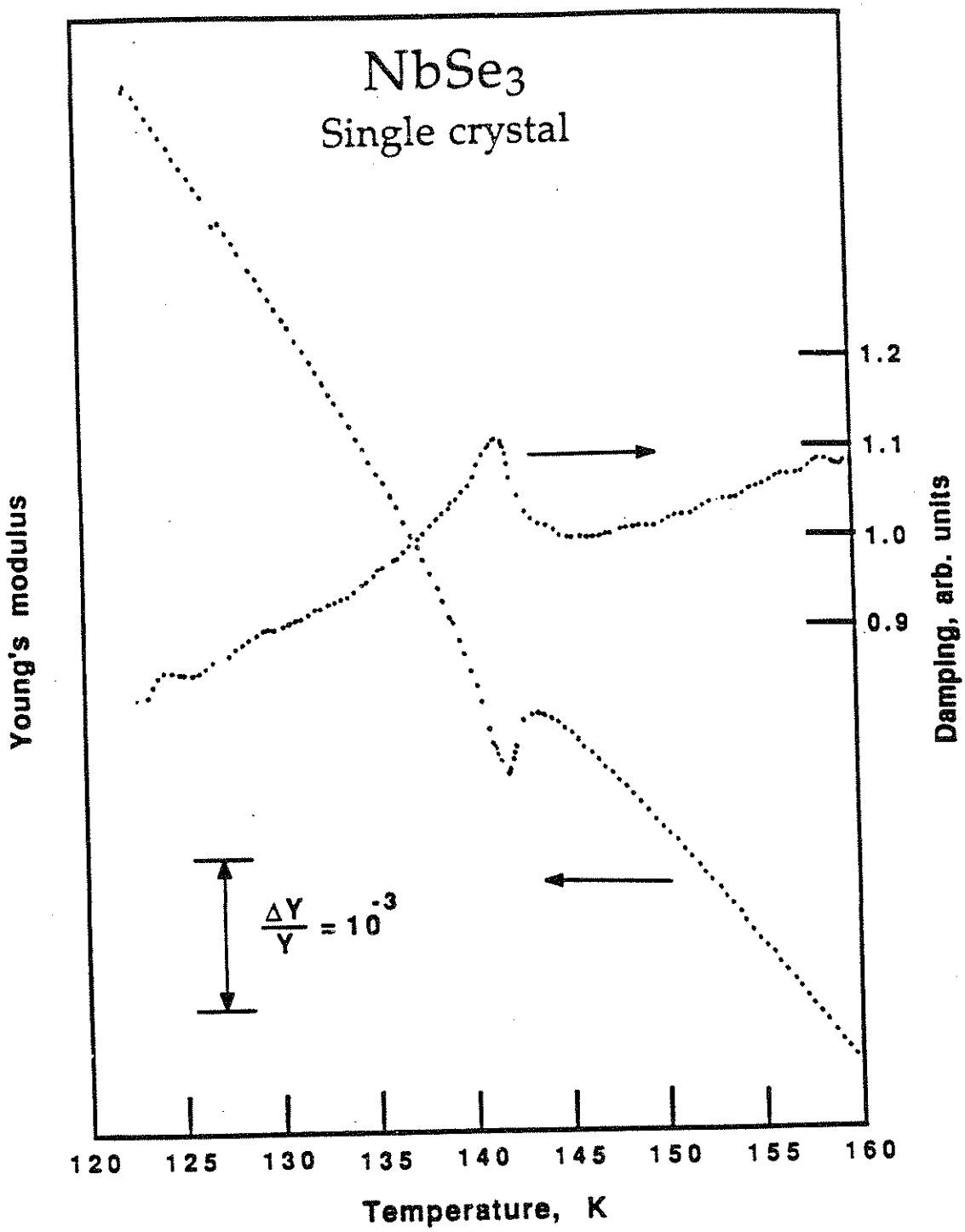


Fig 6-3. Young's modulus (Y) and damping plotted as functions of temperature near the upper CDW transition for single crystal $NbSe_3$.

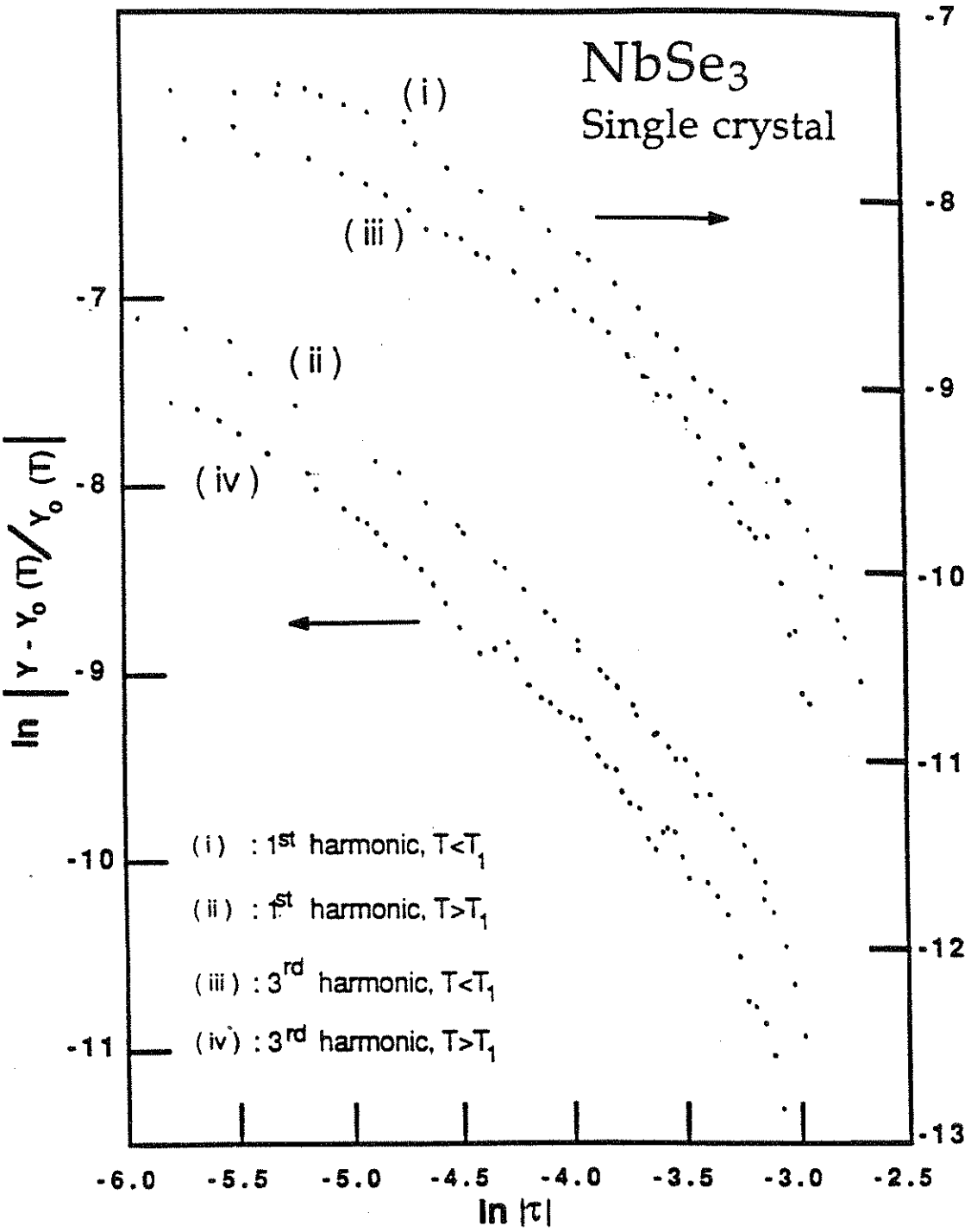


Fig. 6-4. Logarithm of the reduced Young's modulus, $(Y(T)-Y_0(T))/Y_0(T)$, vs the logarithm of the reduced temperature, $\tau \equiv (T-T_0)/T_0$, near the upper CDW transition (144K) for the first and third harmonics of single crystal $NbSe_3$.

scale as $\tau^{3/2}$ for $\tau >> \tau_1$ and $\tau^{1/2}$ for $\tau < \tau_1$ where $\tau_1$ is a crossover temperature between one-dimensional and three-dimensional fluctuations.

$$\tau_1 = \frac{\Omega_t^2}{\lambda z \Omega_p^2} \approx \frac{\sigma_\perp}{\sigma_\parallel}, \qquad (6.1)$$

where $\sigma_\perp$ and $\sigma_\parallel$ are the transverse and longitudinal conductivities, respectively, $\Omega_t$ is the hopping frequency between chains, $\lambda$ is the electron-phonon coupling constant, z is a parameter of order 1, and $\Omega_p$ is the ionic plasma frequency. We estimate $\tau_1$ from the ratio of the transverse to parallel conductivity to be approximately 0.003. As seen previously in $(TaSe_4)_2I$,[15] the curves above and below $T_p$ do not give similar temperature dependences. The slopes lie between the expected values of -3/2 and -1/2 and may demonstrate a region of intermediate dimensionality. The frequency independence of the slopes is expected since the anomaly arises from the interaction between phonons and the phason mode which exhibits no dispersion in this frequency range.

A small softening in Y is also visible at $T_2$ (Fig. 6-5). The anomaly has previously been described[16, 17] simply as an increase in $\partial Y/\partial T$ at $T_2$ but in our data it is clearly seen as an anomaly ($\Delta Y/Y \cong -1.3 \times 10^{-4}$) which disappears as T is decreased below $T_2$. To obtain the lower curve, we subtracted a quadratic best fit from 25K to 55K. Using a quadratic best fit above the transition, no softening was visible. No anomaly is observed in the damping within our experimental resolution.

### 6.4 Magneto-elastic effects

Fig. 6-6 shows $f_0(T)$ for magnetic fields of 0T and 7.7T. The 7.7T curve shows an anomalous 0.9 Hz decrease in resonant frequency which is nearly independent of temperature. This temperature independent

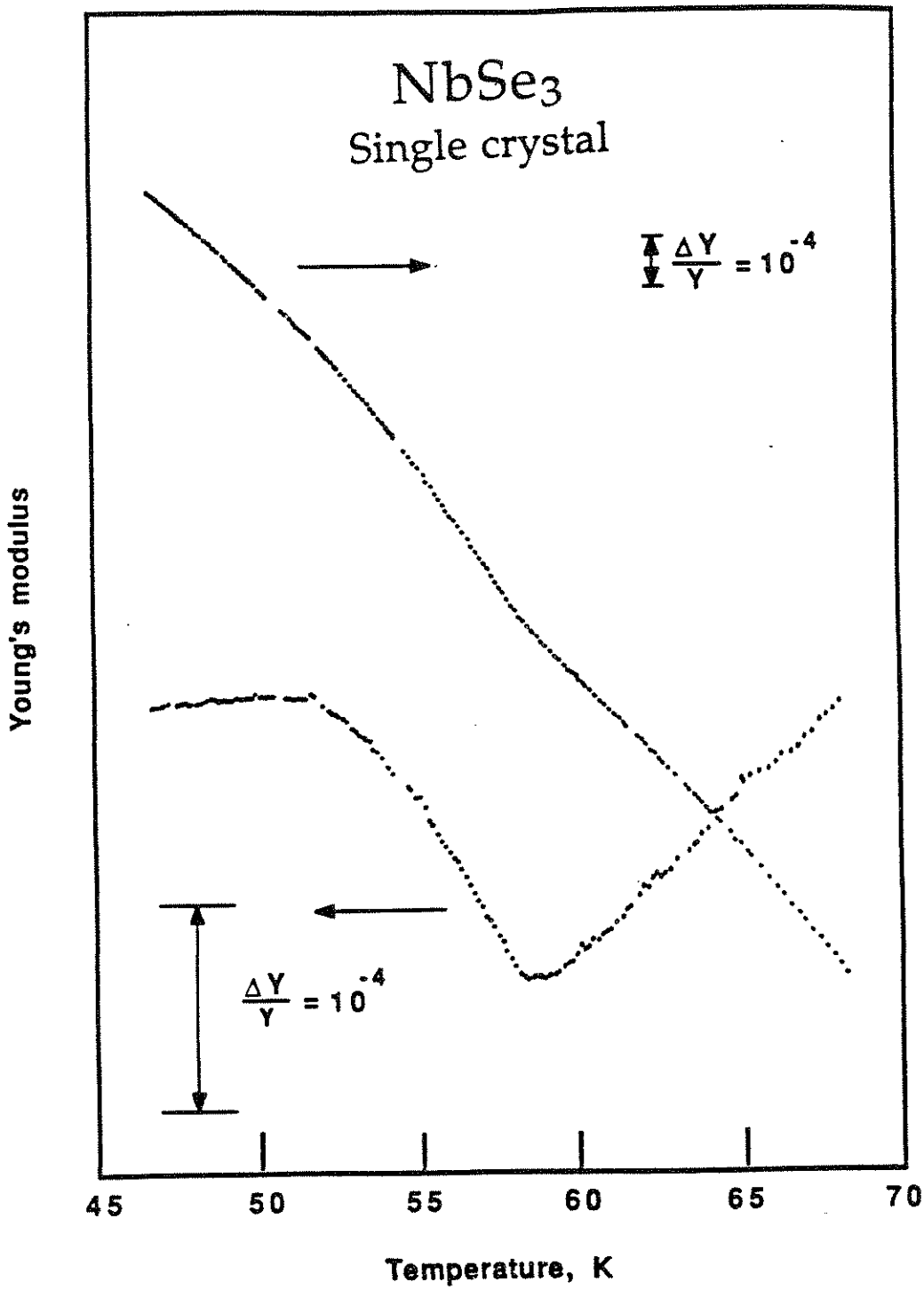


Fig. 6-5. Young's modulus as a function of temperature near the lower CDW transition (59K) of single crystal $NbSe_3$. The data in the lower curve has had a quadratic best fit (30K to 50K) removed to highlight the anomaly.

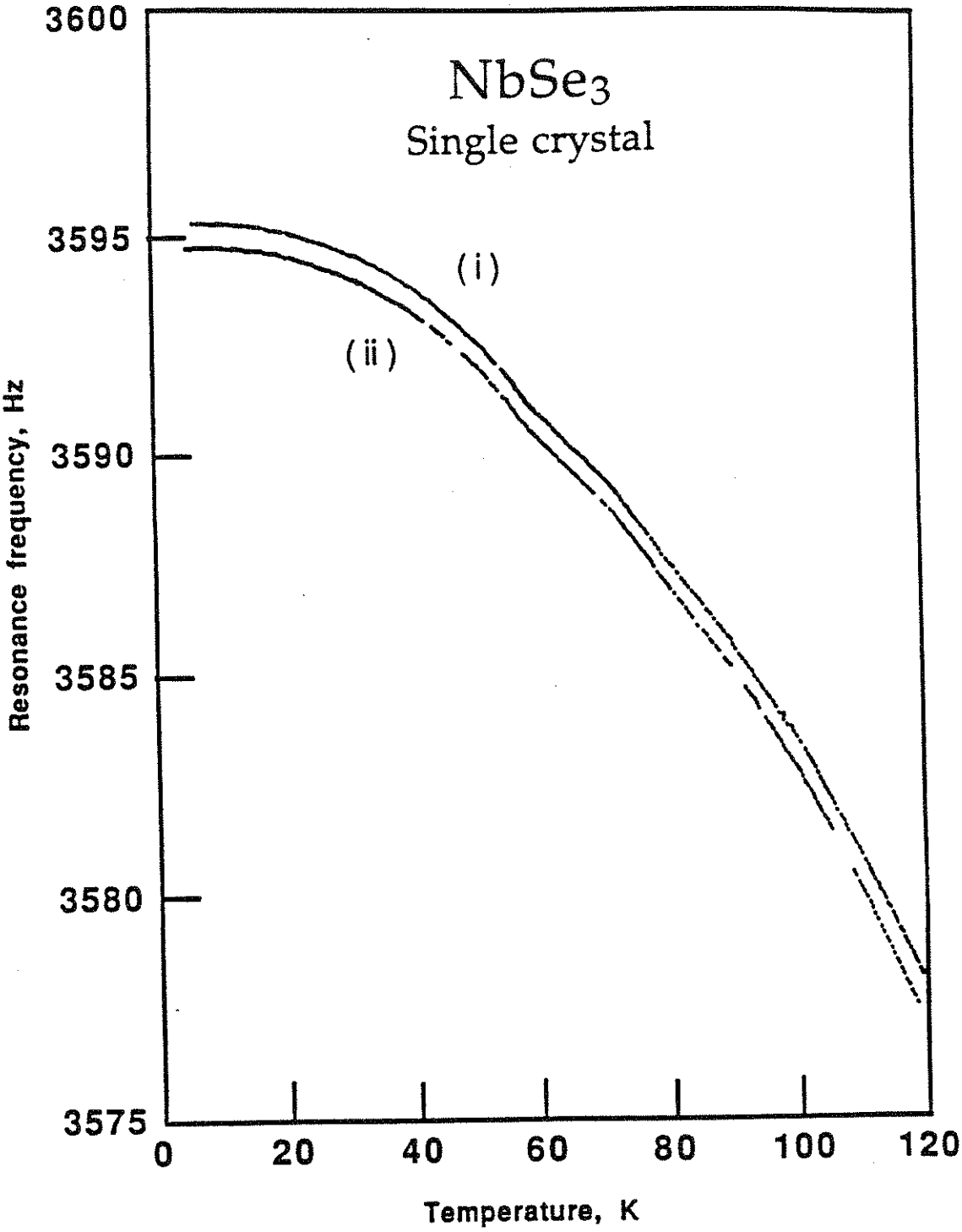


Fig. 6-6. Resonance frequency ($f_o$) plotted as a function of temperature for two magnetic fields, (i) 0T and (ii) 7.7T.

softening is believed to arise from a magneto-mechanical effect and does not reflect an actual change in the Young's modulus. We discuss this effect in greater detail below. To demonstrate the similarity between the two curves, they are replotted in Fig. 6-7a with a quadratic background (fitted between 4.2 and 40K to the 0T data) removed. The 7.7T curve has been vertically shifted to aid comparison. Clearly, they show nearly identical temperature dependence. The small peaks and shifts most likely arise from the freezing out of various relaxation mechanisms.

To increase our sensitivity in the region from 5K to 40K, several runs were averaged to cancel out spurious effects. Fig. 6-7b depicts the 7.7T data with a baseline subtraction of the 0T data. From this data, it seems that additional softening occurs in magnetic fields at 20K, but no feature is evident at 30K. While there is scatter (~3 ppm) in some temperature intervals, many of the finer peaks are reproducible. In a temperature range which includes $T_2$, Fig. 6-8 shows no anomalous magneto-elastic effects associated with the Peierls transition. A peculiar anomaly occurs above the transition, and additional stiffening is evident as the sample is cooled below 45K.

The stiffening observed below 45 K in 7.7T (Fig. 6-6) is consistent with the theory of Maki and Virosztek[4] on the effect of sound velocity of a pinned CDW. The sound velocity should increase below the CDW transition because with pinning, the phason mode can no longer participate in screening the phonons. From their theory,

$$\frac{\Delta Y}{Y} \cong \frac{\lambda g(T)}{1-\lambda}, \qquad (6.2)$$

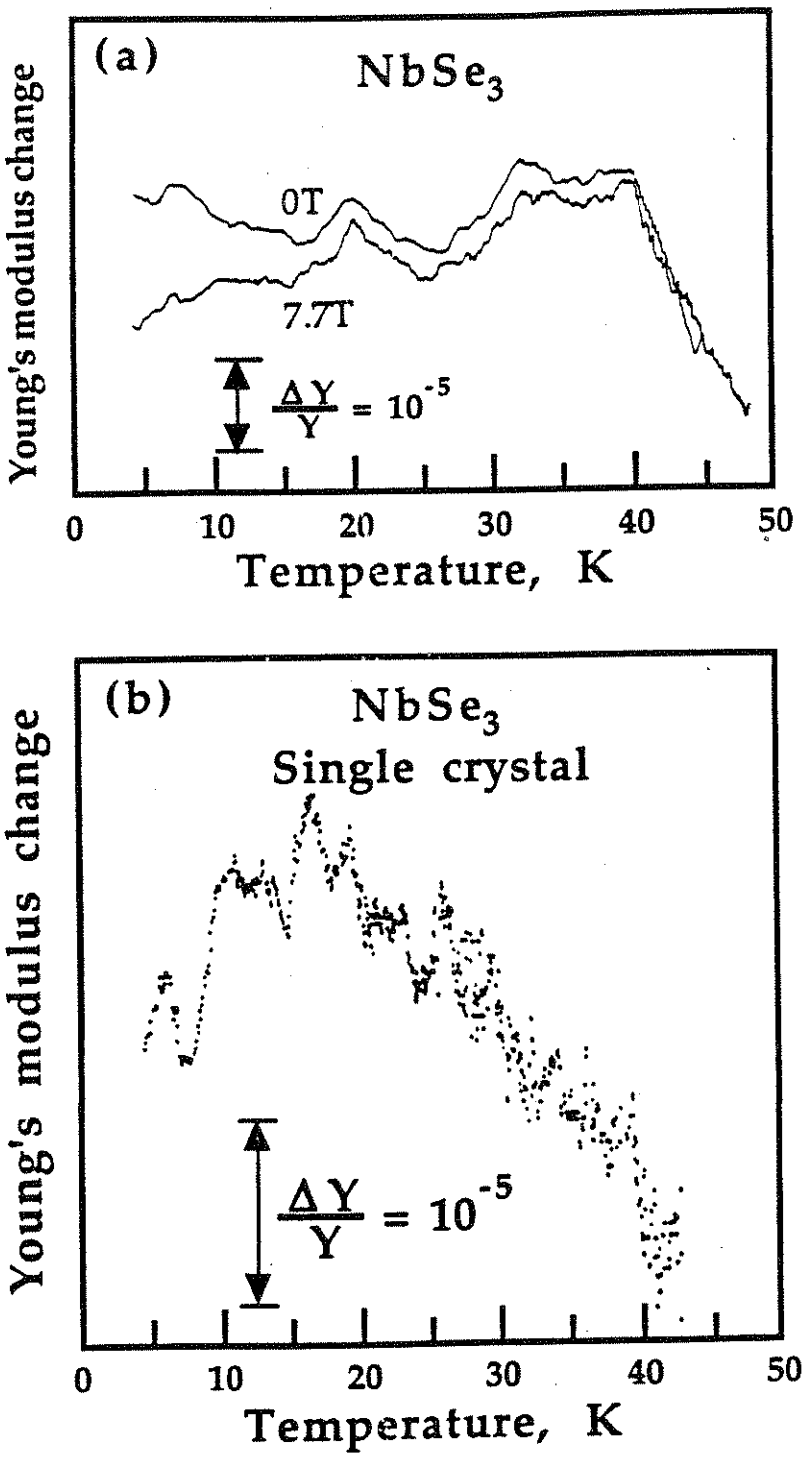


Fig. 6-7. Young's modulus change plotted as a function of temperature below the lower CDW transition. (a) shows the data for 0T and 7.7T plotted with a quadratic background removed to accentuate small scale structure. (b) shows the data for 7.7T normalized by removing a cubic spline fit to the 0T data.

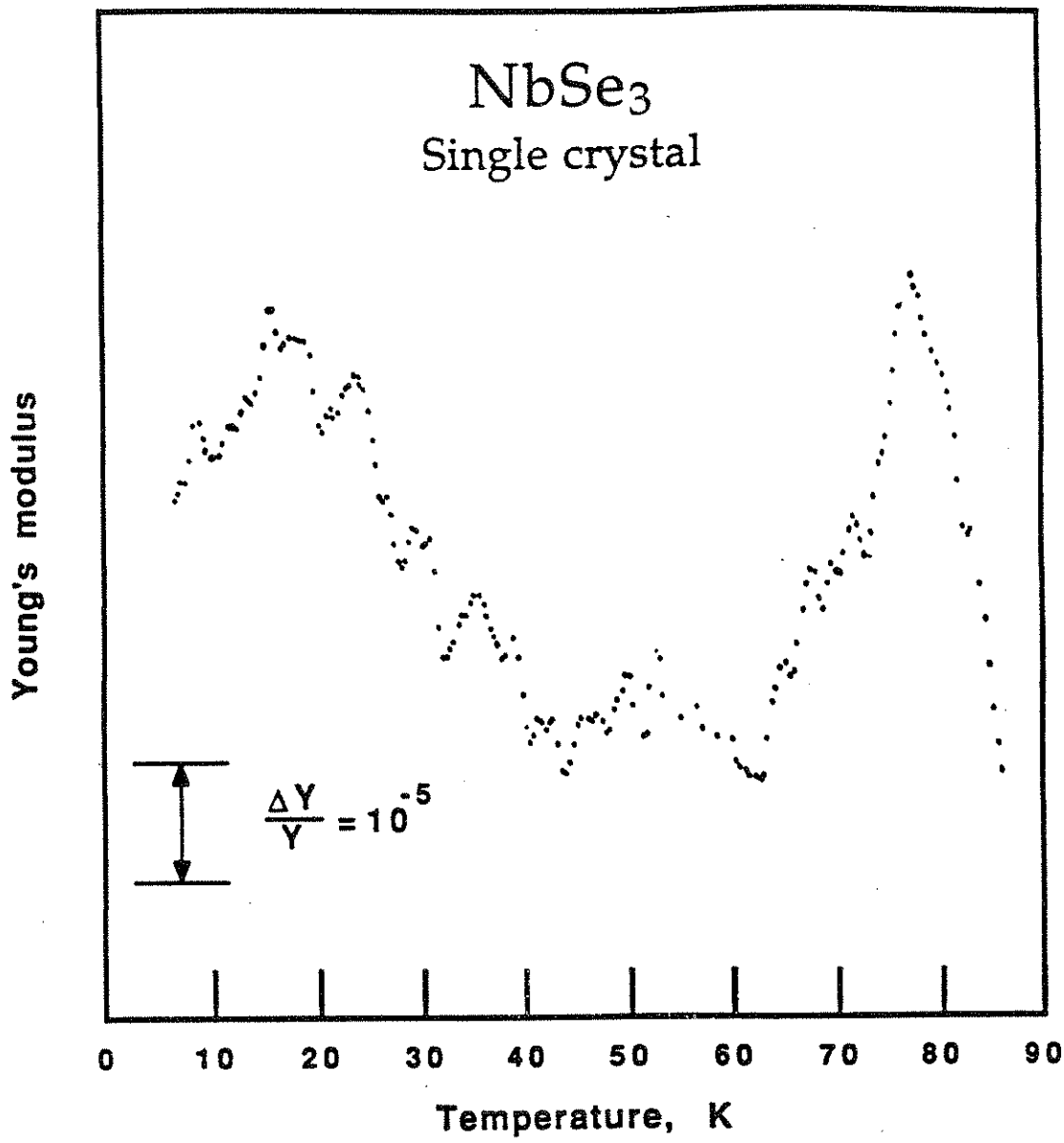


Fig. 6-8. Young's modulus data for single crystal $NbSe_3$ in 7.7T normalized by removing a cubic spline fit to the 0T data.

where g(T) is the CDW carrier density as a function of temperature. From Fig. 6-4, using a straight-line extrapolation from above $T_2$ to 15K below $T_2$, we find $\Delta Y/Y \cong 5.6 \times 10^{-5}$. At this transition approximately 40% of the Fermi surface is destroyed. Both NBN[8, 9] and magnetoresistance[7] experiments indicate carrier conversion into the lower CDW as the magnetic field is increased. At 7.7T, they predict increases of 5% and 30% respectively on the CDW carrier density with an onset of the conversion at 50K. In Figs. 6-7b and 6-8, we see an increase in $\Delta Y/Y$ of $2.8 \times 10^{-5}$ with an onset of ~40K. From equation 6.2, this suggests a 50% increase in the lower CDW carrier density. Because of the shape of the transition, the Young's modulus increase associated with the lower CDW transition may not be correctly reflected by a linear extrapolation.

The softening which sets in at 18K may be the signature of a magnetically induced phase transition. However, the work of Parker *et al.*[10] suggests that the phase transition occurs at higher temperatures, at which no elasticity anomaly is visible. Our experimental configuration is only sensitive to transitions which couple to strain in the b-direction. This phase transition may not couple to this strain and would thus not be observed.

We now consider the magneto-mechanical effects on the sample resonant frequency in greater detail. The data of Fig. 6-5 suggest a huge magnetically induced softening of the Young's modulus ( $\Delta Y/Y = -5 \times 10^{-4}$ at 7.7T). The magnitude of the softening varies as $H^2$ and is similar to that seen for magnetic alloys such as Au-Fe or Cu-Fe.[18] However, the resonant frequency shift is not independent of the flexural mode. As shown in Table 6.1, the relative frequency shift decreases for higher modes —

| Mode | Temperature (K) | Resonant frequency (Hz) | $\Delta f_o$ at H=7.7T (Hz) | $\Delta f_o/f_o$ |
|---|---|---|---|---|
| fundamental | 5.14 | 575.48 | -0.75 | $-1.29 \times 10^{-3}$ |
| | 35.40 | 575.510 | -0.725 | $-1.26 \times 10^{-3}$ |
| 1st harmonic | 5.14 | 3595.57 | -0.90 | $-2.5 \times 10^{-4}$ |
| | 35.40 | 3594.48 | -1.01 | $-2.8 \times 10^{-4}$ |
| 2nd harmonic | 35.40 | 10,014.73 | -0.16 | $-1.6 \times 10^{-5}$ |
| 3rd harmonic | 35.40 | 19,662.38 | -1.22 | $-6.2 \times 10^{-5}$ |

Table 6.1. Dependence of the resonant frequency ($f_o$) on flexural mode, magnetic field (H), and temperature. $\Delta f_o \equiv f_o(7.7T) - f_o(0T)$. The data show that the shift in resonant frequency decreases at higher modes.

though the decrease is not monotonic. All samples show similar decreases in $f_o$ with applied magnetic field. To ~1%, the sample damping in the He environment is not affected by applied fields. The dynamics of a conducting beam in a strong magnetic field are quite complex; both eddy currents and sample paramagnetism can cause significant changes in the resonant frequency.

For our experimental configuration, in which H is parallel to the direction of vibration, eddy current effects are expected to be small. If the sample were a perfect conductor, then an applied magnetic field would induce a new resonant frequency, $f_o'$ and

$$f_o' = f_o ( 1 + \mu_o H^2/2Y)^{1/2} \qquad (6.3)$$

where $\mu_o$ is the permeability of free space.[19] Assuming Y=200GPa, we expect $f_o$ to increase by 60 ppm for a perfect conductor. In a normal conductor, this stiffening is modified by the ratio of the sample's effective inductive impedance ($f_o \cdot L_s$) to its resistive impedance ($R_s$). Using the results of computer modeling,[20] we estimate

$$L_s = (0.370)\, \mu_o\, (w+L) \cong 1.4 \text{ nH} \qquad (6.4)$$

and

$$R_s = (3.33)\, \rho\, (w^2 + L^2)/(dwL) \cong 9\ \Omega. \qquad (6.5)$$

where $\rho$ is the resistivity (~10$\mu\Omega$cm at 5K); and d, w, and L are the plate thickness, width, and length, respectively. For $f_o$ ~ kHz, the inductive impedance is much smaller than the resistive and any inductive changes in the resonance frequency are extremely small (~$10^{-10}$).

The sample damping may be significantly affected by eddy currents. However, the effect of damping, $\delta$ ($\equiv 1/Q$), on the resonance frequency is small; i.e.

$$f_o' = f_o ( 1 - \delta^2 )^{1/2} \qquad (6.6)$$

where $f_o'$ is the shifted resonance frequency. To cause a $2.5 \times 10^{-4}$ decrease in $f_o$, $\delta$ would have to increase to 0.022 (Q=44). However, we see no change in Q from its low temperature value of 2000.

Moon and Pao[21] have predicted and observed significant changes in the resonant frequency arising from the interaction between the external magnetic field and internal paramagnetic or ferromagnetic moments. Because of the boundary conditions at the sample surfaces, the internal and external magnetic fields are not parallel when the sample is bent, and torques occur along the sample. They find

$$f_o' = f_o\left(1 - \frac{H^2}{H_{cn}^2}\right)^{1/2}, \tag{6.7}$$

where

$$H_{cn}^2 = \frac{\mu_o \mu_r Y}{3\chi^2}\left(1 + \mu_r \frac{\pi d}{4L}\right)\left(\frac{n\pi d}{4L}\right)^2, \tag{6.8}$$

and $H_{cn}$ is a critical magnetic field for magneto-elastic buckling of the sample; n is an integer corresponding to the appropriate mode (for the fundamental, first harmonic, etc., n = 1, 2, . . .); and $\chi$ and $\mu_r$ are the sample susceptibility and relative permeability (in MKS units), respectively. Kulick and Scott[22] find $\chi_{NbSe_3} = -54 \times 10^{-6}$ cm$^3$/mole at room temperature, dropping to $-65 \times 10^{-6}$ cm$^3$/mole for T<40K. Using a molar volume of 61.8 cm$^3$/mole ($\chi = 4\pi(65 \times 10^{-6})/61.8 = -13.2 \times 10^{-6}$), we find $H_{cn} = n\ 2.8 \times 10^4$ Tesla. For the 7.7 T field, this $H_{cn}$ yields imperceptible frequency shifts. However, ~ 1.5 ppm of ferromagnetic impurity would explain the observed decrease in resonant frequency. The small decrease in Y with applied field which occurs for T<15K may arise from additional magnetic ordering. Interestingly, the magnetically induced change in $f_o$ for the fundamental and first harmonics scale as 1 : 0.22, similar to that predicted

by Moon and Pao. The anomalous shifts for the second and third harmonics may arise from admixtures of torsional motion in these modes.

Magnetic susceptibility studies of crystals from the same growth, however, found diamagnetic susceptibilities, $\chi_{exp}$, of ~ - 60 x $10^{-6}$ $cm^3$/mole, similar to Kulick and Scott, indicating no ferromagnetic impurities to < 0.1 ppm. Low T data reveal a $\chi_{exp}$ decrease at ~25K with $\chi_{exp} \rightarrow$ -75 x $10^{-6}$ $cm^3$/mole as T$\rightarrow$0. It seems likely that the nearly temperature independent shifts in the resonant frequency arise from a magnetic interaction similar to that described by Moon and Pao. However, there is no evidence for the required magnetic impurities.

### 6.5 Conclusions

We have investigated the temperature and magnetic field dependence of the Young's modulus of $NbSe_3$. The anomaly associated with the lower CDW state has been resolved for the first time and the frequency independence of anomaly at $T_1$ has been confirmed. A reduced temperature analysis of this upper anomaly reveals different behavior for $T < T_1$ and $T > T_1$. The critical exponents associated with this transition suggest that the CDW near $T_1$ may exist in a state of intermediate dimensionality. We see a large, nearly temperature independent softening (~5 x $10^{-4}$) in Y with applied magnetic fields. In the lower CDW state, we see some magnetic enhancement of Y but no evidence for an additional magnetically induced phase transition.

## References


1. M. Barmatz, L. R. Testardi and F. J. DiSalvo, Phys. Rev. **B12**, 4367 (1975).

2. J. W. Brill and W. Roark, Phys. Rev. Lett. **53**, 846 (1984).

3. G. Grüner, A. Zawadowski and P. M. Chaikin, Phys. Rev. Lett. **46**, 511 (1981).

4. K. Maki and A. Virosztеck, Phys. Rev. **B36**, 2910 (1987).

5. T. M. Tritt, M. J. Skove and A. C. Ehrlich, Phys. Rev. **B**, (1991).

6. L. Gor'kov and G. Grüner. *Charge Density Waves in Solids* (North Holland, Amsterdam, 1989) and references therein.

7. R. V. Coleman, G. Eserrman, M. P. Everson, A. Johnson and L. M. Falicov, Phys. Rev. Lett. **55**, 863 (1985).

8. T. M. Tritt, D. J. Gillespie, A. C. Ehrlich and G. X. Tesema, Phys. Rev. Lett. **61**, 1776 (1988).

9. P. Parilla, M. F. Hundley and A. Zettl, Phys. Rev. Lett. **57**, 619 (1986).

10. I. D. Parker, A. L. Chen, A. Zettl and P. Y. Yu, Synth. Met. **43**, 3859 (1991).

11. L. R. Testardi, in *Physical Acoustics*, W. P. Mason and R. N. Thurston ed., (Academic, New York, 1973), p. 193.

12. L. R. Testardi, Phys. Rev. **B12**, 3849 (1975).

13. R. C. Lacoe, Ph. D. Thesis, University of California, Los Angeles (1983).

14. Y. Nakane, J. Phys. Soc. Jpn. **55**, 2235 (1986).

15. Atsushi Suzuki, Hiroshi Mizubayashi and Shigeo Okuda, J. Phys. Soc. Jpn. **57**, 4322 (1988).

16. X.-D. Xiang and J. W. Brill, Phys. Rev. Lett. **63**, 1853 (1989).

17. Xiao-Dong Xiang, Ph.D. Thesis, University of Kentucky, Lexington (1989).

18. T. J. Moran and R. L. Thomas, Phys. Lett. **A45**, 413 (1973).

19. Sylwester Kaliski, Proc. Vib. Prob. **3**, 235 (1962).

20. J. M. Bialek and D. W. Weissenburger, in *Computational Electromagnetics*, Z. J. Cendes ed., (Elsevier Science Publishers, Amsterdam, 1986), p. 193.

21. F. C. Moon and Yih-Hsing Pao, J. App. Mech. **36**, 92 (1969).

22. J. D. Kulick and J. C. Scott, Solid State Comm. **32**, 217 (1979).

# Chapter 7: Metastable Length States of the CDW Material $TaS_3$

## 7.1 Introduction

Charge-density wave (CDW) materials exhibit many unique and interesting properties, such as non-linear resistivity, narrow-band noise (NBN),[1] broadband noise (BBN),[2] and softening of the Young's modulus (Y) upon CDW depinning.[3] Many of these properties can be explained within models which consider the CDW as a deformable medium with associated elasticity.[4-7] The interaction of collective-mode CDW condensate with a random distribution of impurities embedded in the host lattice leads to a hierarchy of metastable electronic configurations.[6] The physics of such random systems is currently of great theoretical and experimental interest. Solid state random systems such as spin glasses and disordered conductors display unusual effects ranging from slow relaxation and metastability to localization and frequency dependent conductivity.[8] Metastable states are believed to be the origin of numerous anomalous CDW transport effects such as polarization memory,[9] low-field resistivity hysteresis[10, 11] and relaxation,[12, 13] and stiffness (Young's modulus) hysteresis.[14, 15] An intriguing but poorly understood problem is how the metastable electronic CDW configuration is reflected back (via the CDW-lattice interaction) onto the underlying lattice structure containing the random impurities.

We have investigated the host crystal lattice structure for different CDW electronic configurations in the CDW conductor $TaS_3$ through measurements of the total sample length L as a function of applied dc bias field E and time t.[16] We find that L is extremely sensitive to E, in many

cases even for $E<E_T$, where $E_T$ is the threshold field for CDW depinning (the electric field at which the charge density wave moves or "slides" over macroscopic distances and adds additional dc current). L(E) is hysteretic but can be carefully and repeatably controlled by E, similar to the situation for piezoelectric insulators. The magnitude of the length change effect with bias field is orders of magnitude larger than that for a comparably-sized commercial piezo-electric or than what would be expected exclusively from an E-induced softening of the Young's modulus of $TaS_3$. We interpret the length states as directly reflecting metastable CDW configurations. Using the length change $\Delta L$ as a probe, we follow the metastable state evolution for various E. The qualitative properties of our results are well explained by a simple model of a deformable CDW interacting with fixed impurities, where randomness plays the central role. However, the size of our effect may be difficult to interpret within existing theories of CDW elasticity.[17, 18]

The remainder of this chapter is organized as follows: Sect. 7.2 outlines the experimental method which allows us to detect length changes to 0.02Å. Sect. 7.3 describes the results for sample length as a function of bias field and time. Sect. 7.4 presents a simple model of an elastic CDW coupled to a lattice. The results of this simulation are qualitatively similar to our experimental results, though the size of the simulated length change is two-orders of magnitude smaller than our experimental results. Sect. 7.5 lists a variety of experiments to further explore this surprising effect, and Sect. 7.6 summarizes our results.

## 7.2 Experimental Method

Long hair-like samples of orthorhombic $TaS_3$ were grown in a quartz ampule using vapor transport. $TaS_3$ is a quasi-one-dimensional material with atomic structure as depicted in Fig. 6-1. While the structure is similar to that of $NbSe_3$, orthorhombic $TaS_3$ has 24 chains per unit cell. The conductivity along the chain direction exceeds that normal to the chains by one to two orders of magnitude.

The experimental set-up consisted of a single high-purity $TaS_3$ fiber clamped between a piezo-electric bimorph and a soft aluminum foil leaf spring with an adjustable spring preload. Bias current was passed through the ends of the sample using silver paint contacts in a two probe configuration. In early experiments, the sample length was monitored with a cryogenic tunneling microscope. A more reliable method proved to be a modified version of a helical resonator detector.[19] As shown schematically in Fig. 7-1, one end of a copper helix is grounded to the outer wall of an electromagnetic cavity. The cavity resonant frequency $f_o$ is extremely sensitive to the termination conditions at the free end of the helix. Changes in sample length alter the helix-spring separation and $f_o$. Extraneous vibrations were filtered out with a time constant of 3 seconds, yielding a sample length change resolution better than 0.2 Å. The grounded aluminum leaf spring and bimorph are mounted an an X-X stage to allow movement parallel to the sample.

At room temperature, the bending displacement of the aluminum leaf spring and the separation ($\delta_o$) between the leaf spring and helix are separately adjusted. At the desired $\delta_o$ (usually ~ 100μm) and sample

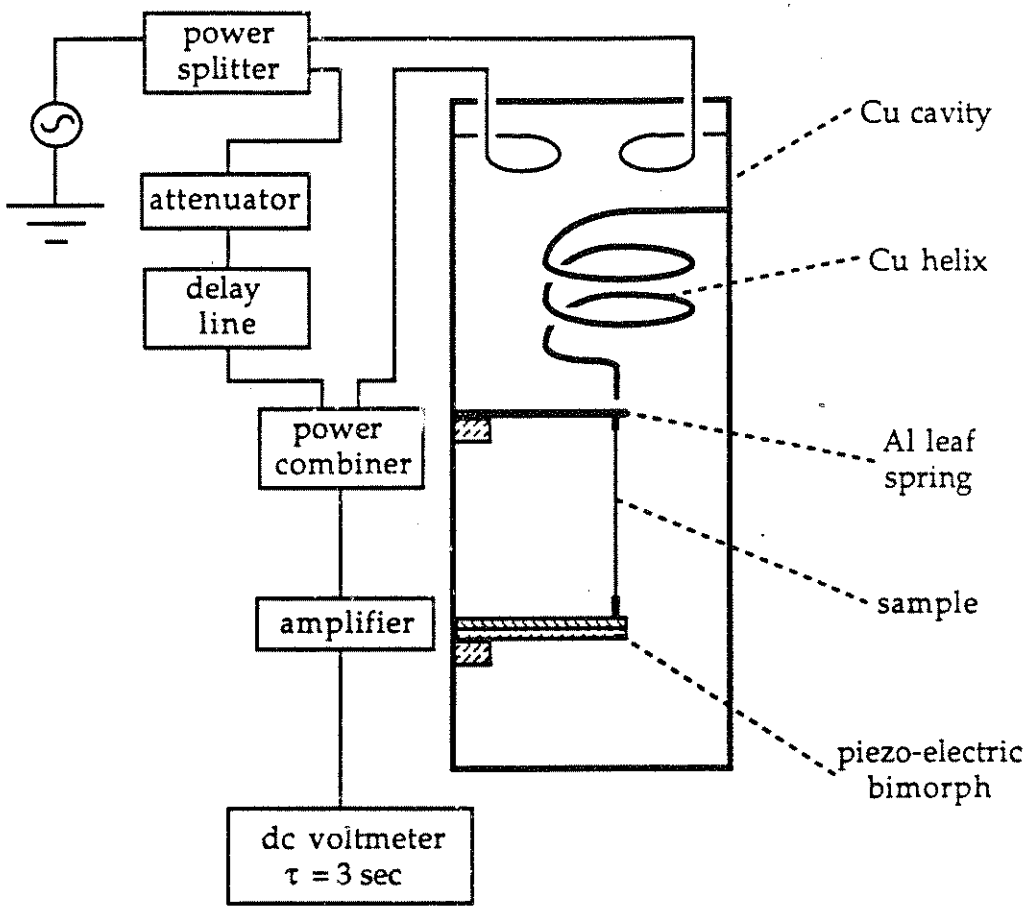


Fig. 7-1. Schematic diagram of helical resonator. The particular devices used are as follows: rf signal generator: HP8656A, power splitter: Mini-Circuits ZSC-2-4, delay line: General Radio Co. 874-LK20, amplifier: Avantek GPM-1052, attenuator: Kay 5150, dc voltmeter: Keithley 177.

tensile stress (~MPa), the bimorph and leaf spring mounts are rigidly clamped to a copper support. The spring constant of the leaf spring is chosen to ensure that the tensile stress remains constant upon cooling. The bimorph was calibrated optically at 300K and 77K and is only used to map the measured changes in resonant frequency to changes in sample length. The most precise bimorph calibration is provided by the helical resonator itself. For $\delta_o$>150μm, the termination conditions change very little upon cooling and the effects of bimorph movement on $f_o$ are identical to those at room temperature. Ten $TaS_3$ crystals were examined, whose lengths and room temperature resistances varied from 0.5-1.0 cm and 30Ω-1kΩ, respectively. Sample threshold fields were of order 200mV/cm at 77K.

## 7.3 Results

### 7.31 Sample length as a function of bias field

Samples were cooled under a small but finite stress (~MPa) with no applied current in ~1 torr of He. After stabilizing the temperature at 77K with drifts of < 5 mK/min, a continuous triangle-wave bias current at ~ 0.01 Hz was applied to the sample and significant length changes occurred. After several cycles in which |E| exceeded $E_T$, L(E) would stabilize to a closed hysteresis curve. Fig. 7-2 depicts this steady state L(E) for one sample under an applied stress of 0.36 MPa. For this sample, ΔL, the difference of the two lengths at E=0, is 40Å, corresponding to a difference in strain of ~$5 \times 10^{-7}$. Even for E~$3E_T$, the lengths for increasing and decreasing fields are not identical, suggesting some "memory" even in the sliding state. Heating effects are visible as an upward curvature at large E.

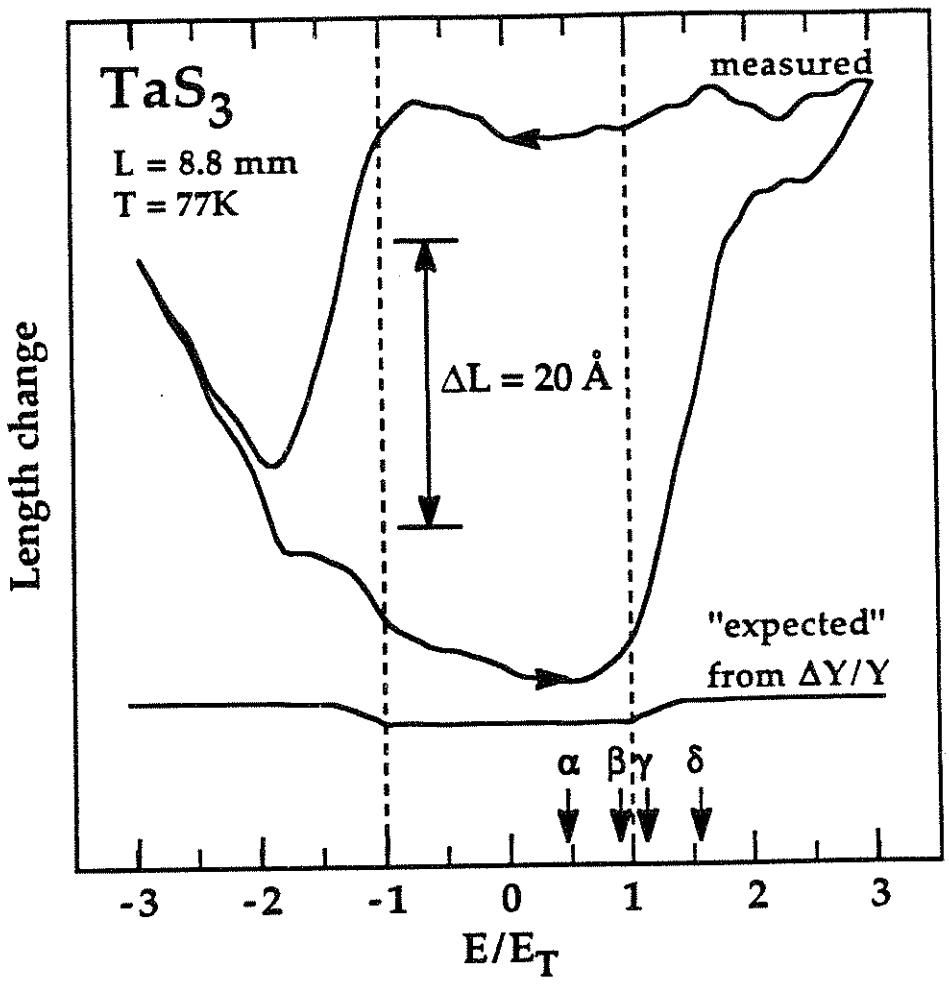


Fig. 7-2. Change in sample length L versus bias field E. The applied triangular waveform for E has a frequency of 0.01 Hz. $E_T \approx 0.18V$. The "expected length change is calculated assuming a softening at $E_T$ of Young's modulus $(\Delta Y/Y) \approx 2\%$ (see text). There is no hysteresis in the "expected" curve. The symbols α, β, γ, and δ refer to bias fields at which the time dependence of L is studied (see Fig. 7-5).

From the form of L(E) at higher temperatures, we estimate that sample heating accounts for ~2 Å length increase at $E_T$.

If the CDW affected the Young's modulus Y but not the equilibrium interatomic spacing, then one would expect L(E) to appear as shown in the lower part of Fig. 7-2. For this calculation we have assumed that Y softens by 2% just above $E_T$, consistent with low stress vibrating reed results.[3] Recent more direct measurements[20] of Y with large applied stresses suggest no softening within ± 0.2%. Indeed, it was the discrepancy between these two experimental results which prompted us to investigate length changes with a small applied stress. Any of the reported hysteretic effects[14, 15] in Y would be too small to see on this scale. Clearly the changes we see are too large to be explained by published changes in Y.

Increasing the range over which E is swept changes the hysteresis only slightly. The shape and size of the steady state curve for a given sample are unaffected by repeated warming and cooling cycles and by the direction in which $E_T$ is first exceeded. Typically, the initial sample length does not lie on the steady state hysteresis curve, a fact we attribute to nonrecoverable thermal stresses being frozen into the sample during cooling. However, no anomalously large length changes are in general detected in the first bias field cycles, and the initial length may lie above, below, or inside the hysteresis loop.

**7.32 Temperature effects on length change**

Fig. 7-3 depicts the steady state length change as a function of bias field for three different temperatures. The size of the hysteresis decreases as temperature increases. The large curvature at higher T reflects greater Joule heating arising from the activated sample resistance. Above the

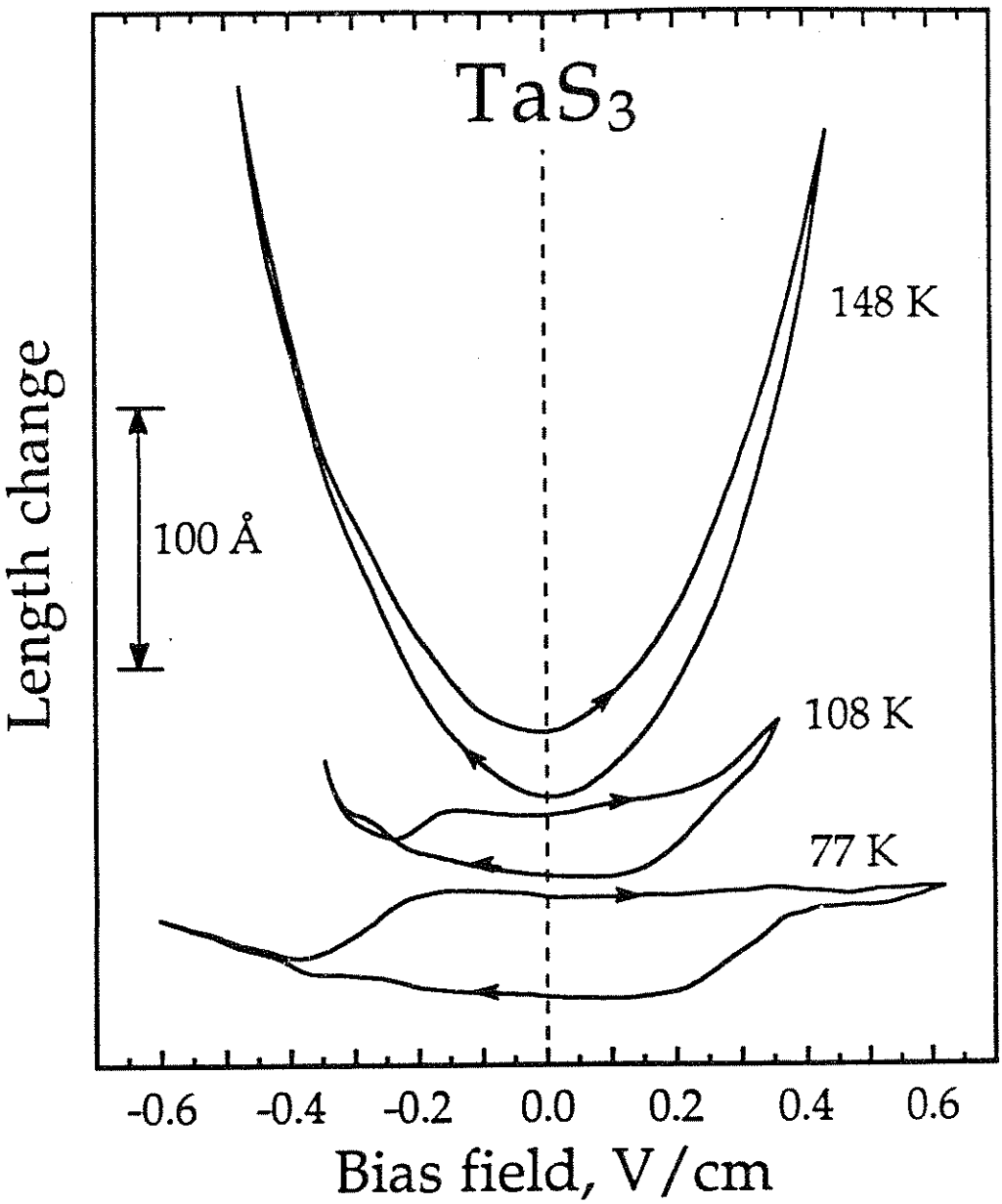


Fig. 7-3. Change in sample length L versus bias field E for three different temperatures. The dotted line is simply a guide for the eye. Heating effects are visible in the 148K data by the strong upward curvature.

Peierls transition (~210K), the hysteresis disappears completely. Based on these curves and assuming that the thermal conductivity of the He gas scales as T, we calculate that heating causes only ~2Å length increase for $E=E_T$ at 77K, too small to explain our observed $\Delta L$.

**7.33 Bending displacements and their bias field dependence**

A surprising characteristic of the length hysteresis is its dependence on stress distribution. The effects vary between samples, but applying a bending moment to the sample can alter the sense in which the hysteresis loop is traversed and increase it size by an order of magnitude. The apparent large length changes with applied moment may arise from sample bending. For samples mounted in a different "clamped-free" configuration, depicted schematically in Fig. 7-4, significant E-induced bending effects are detected. Here, one end of the sample is rigidly clamped and the other end is attached with 0.5mil Au wire to the Al leaf spring. Because of this geometry, no heating effects are visible for fields as large as $10E_T$. However, huge changes of the bending displacement occur at threshold. The bending displacement appears to approach equilibrium at large bias fields, though there is significant hysteresis at low fields. Some samples (L~3mm) show lateral displacements $\Delta L_\perp$ of ~0.1μm. As for the length change experiment, the shape of the hysteresis is dependent of applied stresses and contact configuration. These bending effects may be large enough to affect the interpretation of previous Young's modulus and shear modulus experiments. This effect is not large enough, however, to explain our observed length changes. The "apparent" length change caused by these bending displacements is ~ $\Delta L_\perp^2/L \ll 1$Å.

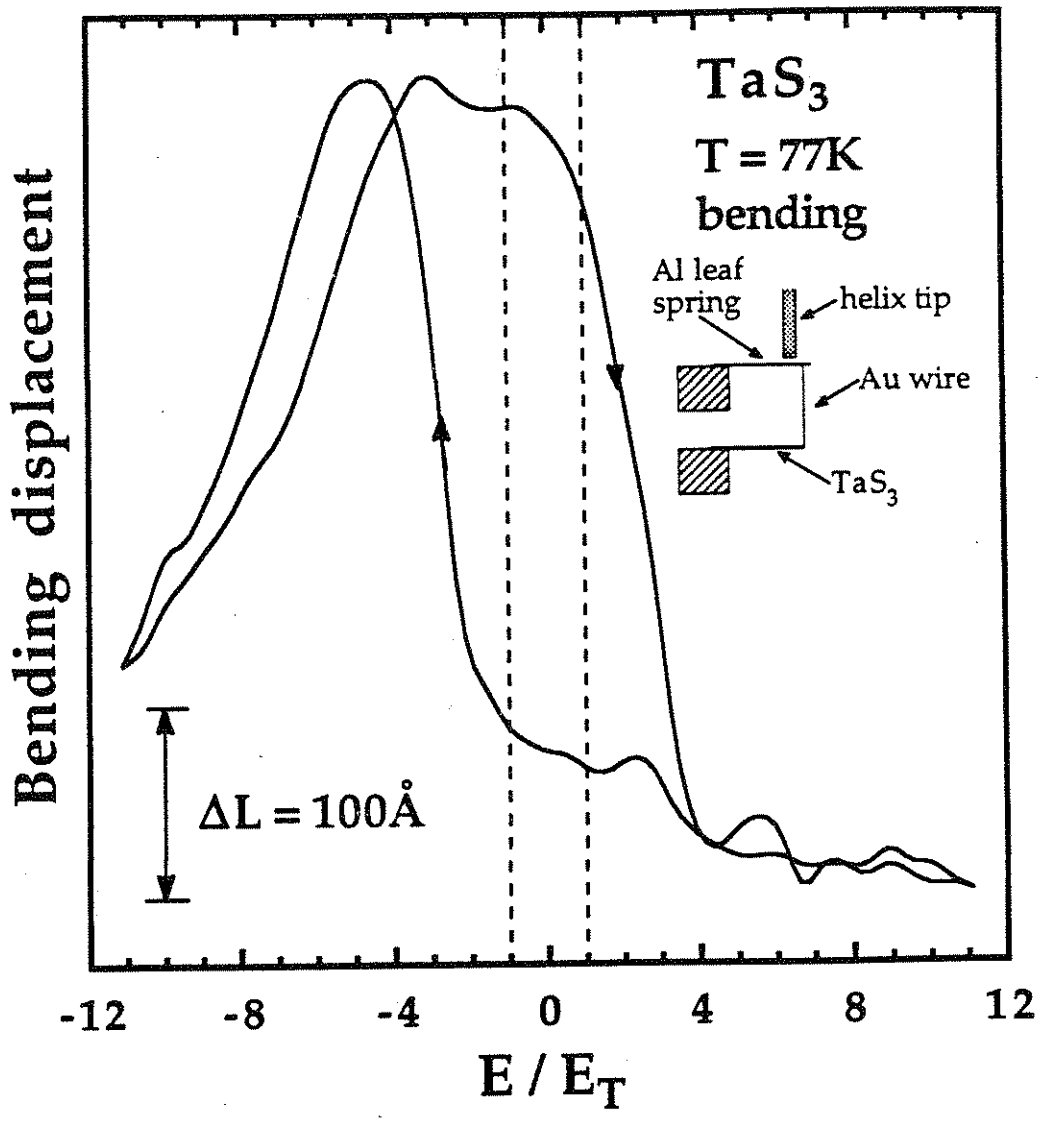


Fig. 7-4. Change in the bending displacement at the end of a 3mm $TaS_3$ crystal as a function of bias field. The inset depicts the experimental apparatus.

### 7.34 Time dependence of length changes

The metastable length states at E=0 appear to be extremely stable with no decay evident during 24 hours. Effects suggestive of glassy decays are seen in the time dependence of L for E≠0. For the four bias field values denoted by α, β, γ, and δ in Fig. 7-2, the sample length L is plotted as a function of time t in Fig. 7-5. As shown in the inset of Fig. 7-5, a bias field pulse of $-3E_T$ is first used to "initialize" the CDW system; at t = 0 we then apply a positive bias step E after which L(t) is monitored. Even for curves α and β, where $E<E_T$, significant evolution in ΔL occurs — a decrease in L for this sample. As E approaches $E_T$, two processes occur, a fast decrease in length followed by a slow increase. At intermediate times, we see a roughly logarithmic dependence, a signature of glassy dynamics, which appears to saturate for t > 60 sec.

### 7.35 Relation of CDW strain and normal carrier density

Changes in the sample length before depinning are more clearly seen for the sample depicted in Fig. 7-6. From experiments on the resistive hysteresis in $TaS_3$ and $NbSe_3$, it has been suggested that strains in the CDW alter the number of free carriers and $R_o$, the resistance at E=0.[10, 11] For semiconductors, such as Ge and Si, altering the number of free carriers can cause length changes because strain may lower the Gibbs energy of the carrier-lattice system.[21-23] If the free carrier density is changed, we also would expect to see commensurate changes in the differential resistance. However, the differential resistance in Fig. 7-6 surprisingly shows no dependence on E for $E<E_T$ even for E values for which the length has changed substantially. There must, therefore, be some CDW strains which do not couple to $R_o$, and it seems unlikely that length changes can be

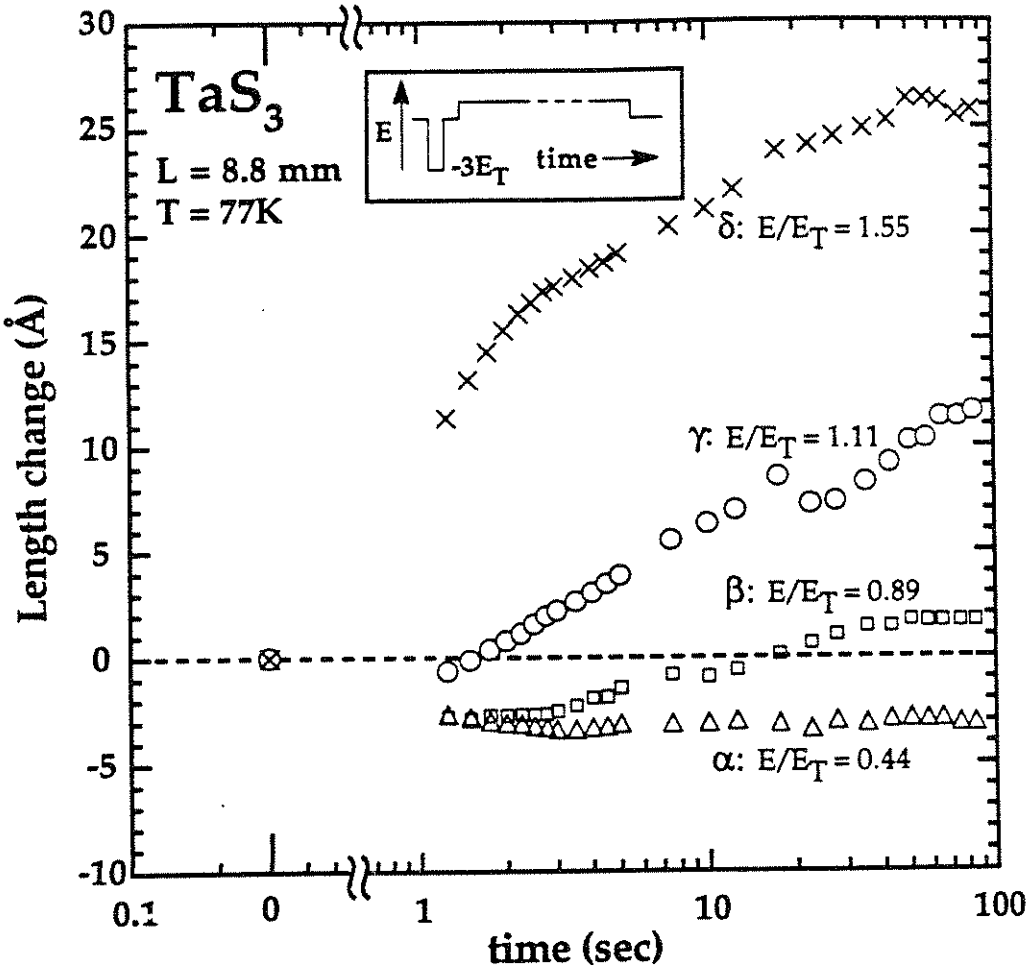


Fig. 7-5. Length change plotted as a function of time t for the fixed bias fields E denoted by α, β, γ, and δ in Fig. 7-1. The sample is first "initialized" with a bias pulse of $-3E_T$ as described in the inset. Length changes are measured relative to the length at t=0, the rising edge of the positive bias step.

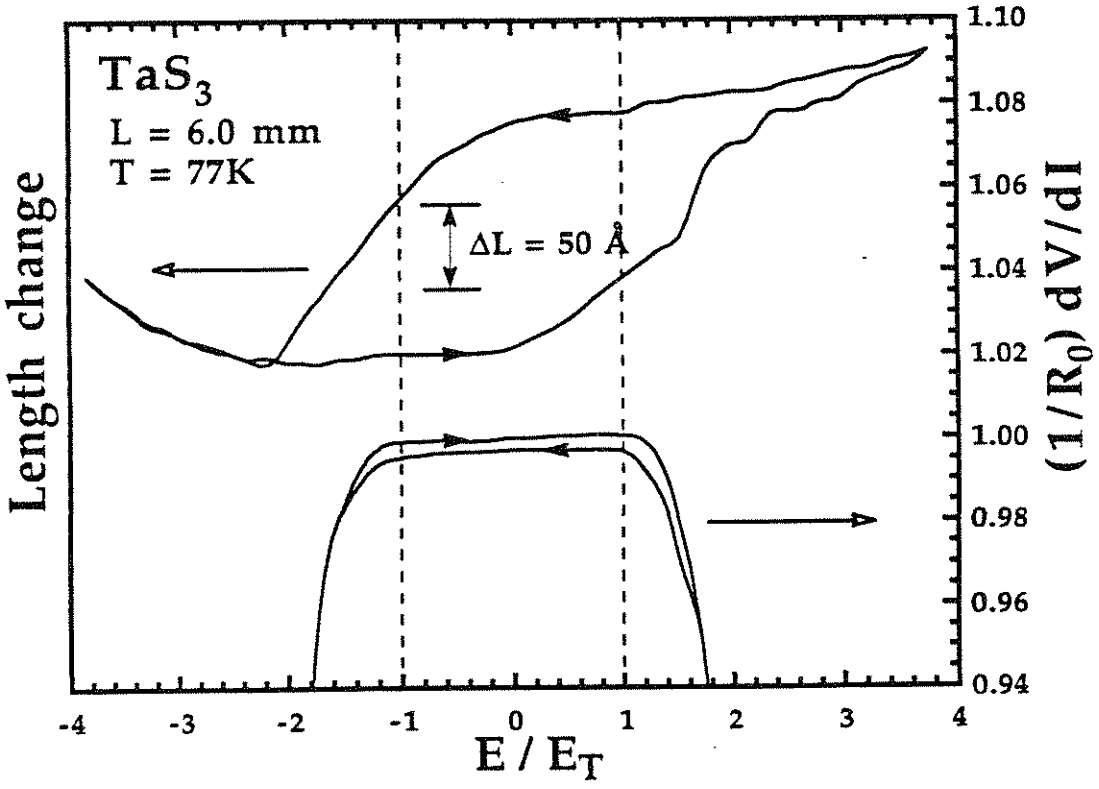


Fig. 7-6. Length change, $\Delta L$, and normalized differential resistance, $(1/R_o)(dV/dI)$, plotted as functions of the bias field E. $R_o$, the low field resistance, $\approx 77\ k\Omega$.

explained by some sort of carrier induced expansion. In all samples studied, there occurs a small hysteresis in dV/dI; the size of the hysteresis is found to scale roughly with the size of the ΔL hysteresis, the smaller L state having greater differential resistance, suggesting that some CDW strains do couple to $R_o$.

Janossy *et al.*[10] and Brown *et al.*[10] also find considerable polarization of the CDW along the sample length. They posit that the CDW is only strongly pinned at the contacts and is free to deform within most of the sample. After the sample is prepared by applying a pulsed bias field exceeding threshold, their results suggest that the CDW is under compression in one half of the sample and tension in the other. We have performed several experiments in which the Al leaf spring is coupled to the center of the sample. For this configuration, we find no anomalously large (>100Å) length changes, implying that CDW currents do not cause large polarizations of the CDW elastic strain. It is possible that the resistive experiments of Janossy *et al.* and Brown *et al.* induced additional phase slips but not CDW strains. Because the CDW wavefunction goes to zero at a phase slip, it may not cause large lattice strains.

### 7.4 Discussion of length changes within deformable CDW model

Many qualitative features of our experimental results can be explained by a simple model of a deformable CDW interacting with impurities fixed in a lattice. We adopt a one-dimensional model similar to the conventional one where the CDW is represented by a number of CDW domains (i.e. phase coherent volumes) interacting with each other via nearest neighbor coupling.[4, 6, 24, 25] Each phase coherent domain is

assumed to sit in a pinning potential which varies sinusoidally with the phase of the domain. The difference is that we have introduced the freedom for the host lattice to deform under the strain generated by the interaction between the CDW's and the host, mediated by the impurity interaction. The Hamiltonian we use for N domains is

$$H = \sum_i \frac{1}{2} a_{i,i-1} \left(\phi_{i,i-1} - \theta_{i,i-1}\right)^2 + \sum_i \frac{1}{2} b_{i,i-1} \left(x_{i,i-1} - l_{i,i-1}\right)^2 - \sum_i V_i \cos\left(\phi_i\right)$$

$$- E \sum_i \rho \left(\frac{l_{i+1,i} + l_{i,i-1}}{2}\right) \phi_i + g(x_1 - x_N) \qquad (7.1)$$

where $\{\phi_i\}$ are the CDW phases of the different domains, $\{x_i\}$ ($x_i > x_{i-1}$) are the locations of the impurity sites, $\{l_i\}$ are their positions at equilibrium (i.e. in the absence of CDW's), $\lambda$ is the CDW wavelength, $x_{i,i-1} = x_i - x_{i-1}$, $l_{i,i-1} = l_i - l_{i-1}$, $\theta_{i,i-1} = 2\pi x_{i,i-1}/\lambda$, $\phi_{i,i-1} = \phi_i - \phi_{i-1}$, $V_i$ is the strength of the impurity potential at $x_i$, E is the external electric field, $\rho$ is the CDW charge density, and g is the external tension. The spring constants for the CDW's and the lattice are dependent on $\{l_i\}$ so that $a_{i,i-1} = A/l_{i,i-1}$ and $b_{i,i-1} = B/l_{i,i-1}$, where A and B are the Young's moduli of the CDW and lattice, respectively. (In fact, because of the factor of $2\pi/\lambda$ which enters in the relation between $\phi$ and position, $Y_{CDW} = (2\pi/\lambda)^2 A$.)

This Hamiltonian can be schematically represented by the classical system of blocks and springs depicted in Fig. 7-7. Each of the large blocks represents an impurity fixed in the lattice; the lattice elasticity, shown as the larger set of springs, allows relative movements of the impurities. The balls attached by smaller springs represent the CDW, with the sinusoidal wells modeling the pinning potentials at the various impurity sites. In this model, a domain is considered as the region between two impurities. Moving the ball in the $i^{th}$ position from the center well into

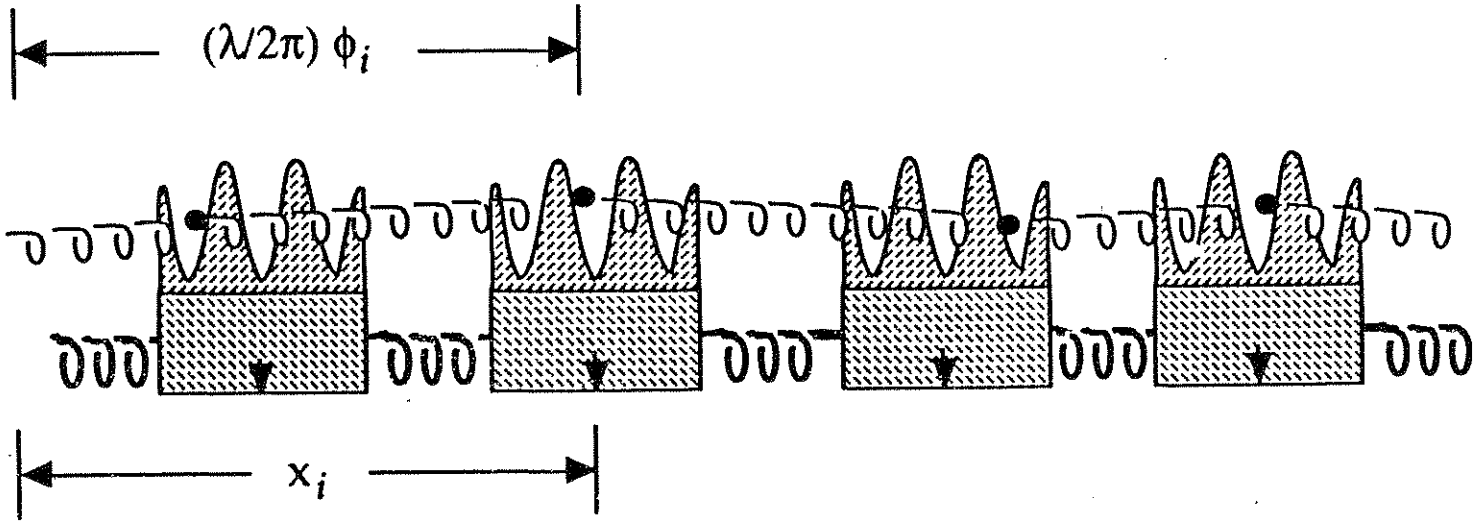


Fig. 7-7. Schematic representation of Equation 7-1. The elements represent the following: block ↔ impurity site; large spring ↔ lattice elasticity; sinusoidal wells ↔ pinning potential of CDW from the impurity; ball ↔ phase of CDW domain at a particular pinning site; and small spring ↔ CDW elasticity. $x_i$ is the position of the $i^{th}$ impurity site and $\phi_i$ is the phase of the $i^{th}$ CDW domain.

the left well (i.e. changing the phase of the $i^{th}$ domain by $-2\pi$) will stretch the CDW "spring" between the i and i+1 positions and induce a lattice contraction between the associated impurity "blocks." In our model, it is just such changes in the CDW metastable state which changes in the internal lattice strains.

The randomness, which is essential in reproducing the experiment, is introduced in $\{l_i\}$ and $\{V_i\}$. The equations of motion are obtained by assuming overdamped dynamics typical of CDW's:

$$\dot{\phi}_i = -\gamma_{\phi,i}\frac{\partial H}{\partial \phi_i}; \qquad \dot{x}_i = -\gamma_{x,i}\frac{\partial H}{\partial x_i}. \tag{7.2}$$

We assume that the domains of smaller size have higher relaxation rates and use the form $\gamma_{\phi,i} = 2\Gamma_\phi l_o/(l_{i+1,i} + l_{i,i-1})$ and $\gamma_{x,i} = 2\Gamma_x l_o/(l_{i+1,i} + l_{i,i-1})$ where $l_o$ is the average of $l_{i,i-1}$, and $\Gamma_\phi$ and $\Gamma_x$ are the average relaxation rates for the CDW and the lattice, respectively.

We have performed our simulation with 32 CDW domains and parameters which are roughly consistent with experimental results. ($Y_{CDW}/B \sim 0.02$ and $l_o \sim 0.7\mu m$.) The parameters have the following values: $A = 50$, $B = 10^5$, $g = 1/16000$, $\Gamma_\phi = \Gamma_x = 1$, $V_x = 0.6 \pm 0.2$, and $l_{i,i-1} = 500 \pm 25$ with all length scales measured in units of $\lambda$. From the energetics of the CDW,[4] the domain length ($l_o$), the pinning potential ($V_i$), and the CDW elasticity (A) are not independent quantities. Indeed, $V_i$ and A determine the domain length. Both the lattice and the CDW are given free boundary conditions. If fixed boundary conditions are used for the CDW, no length changes occur. This can be seen directly from Fig. 7-7. If the $\phi$ positions of the outer two balls are kept fixed relative to their respective impurity pinning potentials, then regardless of the positions of

the inner two balls, the relative x positions the outer impurities will remain fixed. More succinctly, fixing two points of the CDW "spring" completely determines the difference in force applied at those two points. This result holds for any linearly elastic CDW model. If phase slips were allowed to occur in the simulation then length changes could occur for fixed boundary conditions.

For the simulation we first "anneal" the model to find the lowest energy state for E=0. We then use a slow triangle wave signal for E and calculate the total sample length L for different E, similar to the experimental determination of L(E) at long time t. (Because of computational difficulties associated with bias field singularities, we have not studied the detailed time dependence of L(E,t) at fixed E.) Fig. 7-8a depicts the current (I), as determined by the steady state creation and destruction of CDW phase at the two boundaries, vs bias field for our simulation. The current drops sharply to zero when the CDW pins; however, some current is evident before the CDW completely depins. We believe this non-zero I for $E<E_T$ arises from difficulties in averaging I over long enough times. When the time scale of the bias field ramp is increased, we see no current for $E<E_T$.

The relative length change of our model for two cycles of E is shown in Fig. 7-8b. Many of the features seen in the experiment are reproduced: (a) we observe only two length states as the bias is swept toward zero; (b) changes in the internal state of the CDW below threshold ($|E|<E_T$) are clearly observed in the length; (c) the length for sliding states ($|E|>E_T$) depends on sample history; (d) the final hysteresis curve is insensitive to the initial sweep direction (positive or negative); and (e) our CDW state at

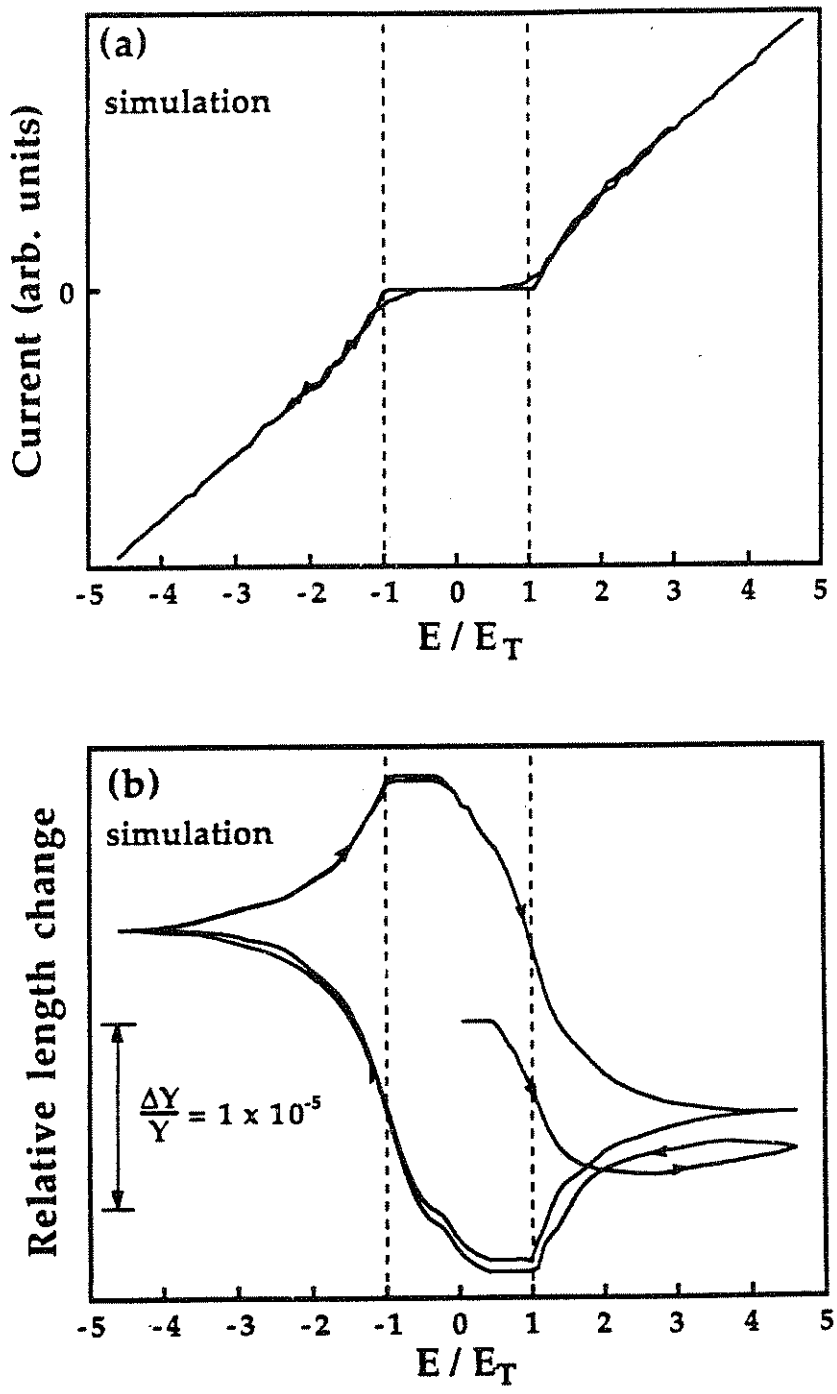


Fig. 7-8. (a) Current as a function of bias field E for a model CDW-lattice system (see text). (b) Relative length change of our simulated system of 32 CDW domains (Equation 7-1) as a function of bias field E. The dotted lines mark the threshold field as determined by the simulated current.

t = 0, which we initially generated by relaxing the CDW from "equilibrium," is never recovered once a bias field is applied. With these agreements, we believe that the model Hamiltonian, Eq. (7-1), captures much of the essential physics involved in the experiment.

Based on these results, we suggest that the measured length hysteresis in $TaS_3$ is the result of changing $\Delta\Phi$, the total CDW phase change between the two ends of the sample ($\phi_N - \phi_1$ in our simulation). Decreasing $\Delta\Phi$, by removing CDW wavelengths from the interior of the sample, expands the CDW which then exerts a compressive stress on the host lattice. Length changes can only occur if phase slip occurs either at the contacts or within the sample. For the observed length hysteresis to occur, the inversion symmetry of a perfect $TaS_3$ crystal must be broken. In our model, this occurs through randomly distributed impurities. In actual samples, it must arise from the randomly distributed impurities together with any significant applied stress distributions or contact perturbations.

In the simulation, length changes arise from fluctuations in the pinning potentials and the relative length changes, $\Delta L/L$, vary as $D^{-1/2}$ for fixed domain size where D is the number of domains. Scaling the results of the simulation ($\Delta L/L \sim 2 \times 10^{-5}$) to an actual sample of $10^8$ domains yields an expected $\Delta L/L \sim 10^{-9}$, much smaller than our measured $\Delta L/L \sim 10^{-6}$. Our sample volume is 0.88cm x 25μm x 25μm and we use a domain volume of 0.7 x 0.2 x 0.2 $\mu m^3$. (There are larger published values for $l_o$, the coherence length along the conduction axis;[11] however, if we increase $l_o$ at fixed sample length in our model, the $\Delta L/L$ is even smaller.) Though we expect the model to yield only approximate results for $\Delta L$, this large discrepancy is surprising. It suggests that there are coherent effects

between various domains; these effects are not accounted for by the existing theories of CDW elasticity.[17, 18]

One can also estimate the length hysteresis for a given sample simply from phenomenological arguments. In what follows we derive an estimate of the maximum strain difference between two metastable configurations. In the conventional model of the CDW,[4] the sample is divided into a number of CDW phase coherent volumes, $V_\phi$. $\Delta S_v$, the difference in lattice strain for two different CDW metastable states in a particular $V_\phi$, can be quite large. The maximum possible $\Delta S_v$ arises when the number of CDW wavelengths $\lambda$ is changed by 1 within a phase coherence length $L_\phi$; no greater change is allowed because of the $L_\phi$ definition. The CDW strain couples to the lattice through a term $Y_{CDW}/Y_{lattice}$, the ratio of the respective Young's moduli; thus, the difference in lattice strains is bounded by $\Delta S_v \sim (Y_{CDW}/Y_{lattice})(\lambda/L_\phi) \sim 10^{-4}$. Here we assume $Y_{CDW}/Y_{lattice} \sim 2\%$ from vibrating reed measurements;[3] $\lambda \sim 13$Å;[26] and as a lower bound we use $L_\phi \sim 0.3$ μm.[27] In a sample of volume 1cm x 10μm x 10μm there are many phase coherent volumes ( $\sim 10^8$, assuming $V_\phi = 0.3\mu m \times 200Å \times 200Å$ from x-ray studies[27]) which, if they add incoherently, implies that the net strain difference over the whole sample, $\Delta L/L$, for different metastable states is $10^{-9}$. Domains this size are not thermally stable at 77K (i.e. the energy present in one thermal degree of freedom is enough to overcome the depinning field of such a small volume). However, from the above analysis, $\Delta L/L \sim (1/L_\phi)L_\phi^{1/2} \sim L_\phi^{-1/2}$; thus, larger domain sizes along the crystal axis will decrease relative length changes. Using a more reasonable domain size ($5.0 \times 0.4 \times 0.4\ \mu m^3$),[11] yields a $\Delta L/L \sim 4 \times 10^{-9}$. Even with the assumption

of maximum phase difference between metastable states, it is necessary to include some coherence between the $V_\phi$ to explain the large size of the measured effect.

### 7.5 Future experiments

To further investigate the remarkable sensitivity of L to different CDW states, several experiments suggest themselves. The most straightforward experiment is the temperature dependence of the bending displacement. Because of the geometry, thermal expansion effects are canceled out and a precise determination of the effect of temperature can be made on both the size of the hysteresis and the glassy decays of the bending displacement for fixed bias field. In a second experiment, it may be possible to correlate the length changes to the amount of disorder by introducing imperfections or altering the sample length, and it may also be possible to observe the pulse duration memory effect as discussed by Coppersmith[28] in a length measurement. It would be interesting to examine other CDW systems, such as $NbSe_3$, $(TaSe_4)_2I$, or $K_{0.3}MoO_3$ (in $K_{0.3}MoO_3$, a material which exhibits no $\Delta Y$ at $E_T$, no changes in L to $\pm$ 1 ppm have been detected[29]). The effect of bending should also be investigated to determine whether it affected previous Y measurements. An additional experiment would be a search for broadband noise in the sample length or bending displacement. This would require smaller time constants for the detection apparatus and a lower noise floor, which the results of Xiang *et al.*[19] indicate is certainly possible. The easiest method may be to use the $TaS_3$ crystal directly to terminate the helix and to measure bending displacements of the crystal.

## 7.6 Conclusions

In summary, we have found the first results that the CDW metastable state directly affects the macroscopic length of samples of $TaS_3$. The following information has been shown about the CDW metastable state: significant changes in the metastable state occur for $E<E_T$ which are not detected in the low field resistance; the dynamics of the random CDW system are such that only two possible CDW states occur as $E \rightarrow 0$ from either above or below; and relative to the CDW elastic state no definite threshold field is evident. Many qualitative features of our experiment can be explained by a surprisingly simple model of a deformable CDW interacting with randomly located impurities; however, the size of the length changes is difficult to explain within existing theories of CDW elasticity. This effect is an important new tool for investigating the evolution of metastable states in CDW systems and in the study of random systems in general.

## References


1. P. Monceau, N. P. Ong, A. M. Portis, A. Meerscaut and J. Rouxel, Phys. Rev. Lett. **37**, 602 (1976).

2. R. M. Fleming and C. C. Grimes, Phys. Rev. Lett. **42**, 1423 (1979).

3. J. W. Brill and W. Roark, Phys. Rev. Lett. **53**, 846 (1984).

4. H. Fukuyama and P. A. Lee, Phys. Rev. **B17**, 535 (1978); P. A. Lee and H. Fukuyama, Phys. Rev. **B17**, 542 (1978); P. A. Lee, and T. M. Rice, Phys. Rev. **B19**, 3970 (1979).

5. G. Grüner, A. Zawadowski and P. M. Chaikin, Phys. Rev. Lett. **46**, 511 (1981).

6. P. B. Littlewood, Phys. Rev. **B42**, 6694 (1986).

7. M. Inui, R. P. Hall, S. Doniach and A. Zettl, Phys. Rev. **B38**, 13 (1988).

8. R.V. Chamberlin and D. N. Haines, Phys. Rev. Lett. **61**, 2197 (1990); V. Bayot, L. Piraux, J. P. Michenaud and J. P. Issi, Phys. Rev. Lett. **65**, 2579 (1990); .

9. R. M. Fleming and L. F. Schneemeyer, Phys. Rev. **B28**, 6996 (1983).

10. A. W. Higgs and J. C. Gill, Sol. State Comm. **47**, 737 (1983); A. Janossy, G. Mihaly and G. Kriza, Sol. State Comm. **51**, 63 (1984); S. E. Brown, L. Mihaly, and G. Grüner, Sol. State Comm. **58**, 231 (1986).

11. D. V. Borodin, S. V. Zaitsev-Zotov and F. Ya. Nad', JETP **66**, 793 (1987).

12. G. Mihaly and L. Mihaly, Phys. Rev. Lett. **52**, 149 (1984).

13. G. Mihaly, A. Janossy and G. Kriza, in *Charge-Density Waves in Solids*, G. Hutiray and J. Solyom ed., (Springer-Verlag, Berlin, 1985), p. 396.

14. Ronald L. Jacobsen and George Mozurkewich, Phys. Rev. **B42**, 2778 (1990).

15. J. W. Brill, W. Roark and G. Minton, Phys. Rev. **B33**, 6831 (1986).

16. S. Hoen, B. Burk, A. Zettl and M. Inui, submitted to Phys. Rev. B

17. George Mozurkewich, Phys. Rev. **B42**, 11 (1990).

18. K. Maki and A. Viroszytek, Phys. Rev. **B36**, 2910 (1987); A. Virosztek and K. Maki, Phys. Rev. **B41**, 7055 (1990); .

19. X.-D. Xiang, J. W. Brill and W. Fuqua, Rev. Sci. Instrum. **60**, 3035 (1989).

20. T. M. Tritt, M. J. Skove and A. C. Ehrlich, Phys. Rev. **B43**, 9972 (1991).

21. T. Figielski, Phys. Stat. Sol. **1**, 306 (1961).

22. R. W. Keyes, in *Solid State Physics*, D. Turnbull and H. Ehrenreich ed., (Academic Press, New York, 1967), p. 37.

23. John J. Hall, Phys. Rev. **161**, 756 (1967); Robert W. Keyes, Phys. Rev. Lett. **34**, 1334 (1975); .

24. Nobukazu Teranishi and Ryogo Kubo, J. Phys. Soc. Jpn **47**, 720 (1979).

25. L. Pietronero and S. Strässler, Phys. Rev. **B28**, 5863 (1983).

26. T. Sambongi, K. Tsutsumi, Y. Shiozaki, M. Yamamoto, K. Yamaya and Y. Abe, Sol. State Comm. **22**, 729 (1977).

27. C. H. Chen and R. M. Fleming, Sol. State Comm. **48**, 777 (1983).

28. S. N. Coppersmith and P. B. Littlewood, Phys. Rev. **B36**, 311 (1987).

29. Matt R. Hauser, Brendan B. Plapp and George Mozurkewich, Phys. Rev. **B43**, 8105 (1991).

# Chapter 8: Broadband Noise and Thermally-Induced Phase Slip Centers in $NbSe_3$

## 8.1 Introduction

The elastic model[1] of charge-density waves (CDW's) first proposed by Fukuyama, Lee, and Rice, has had remarkable success in explaining many of the unique properties of CDW materials. In particular, the existence of a threshold field ($E_T$) for CDW conduction, the presence[2] of narrow band noise (NBN) for bias fields (E) above $E_T$, and the softening of the Young's modulus[3] upon CDW depinning, each appear to arise from the finite elasticity associated with the CDW. The CDW phase degree of freedom is assumed to dominate the dynamics because the finite energy required to induce amplitude distortions (phase slip centers).[1] However, the elastic models[4] have failed to explain the existence of 1/f-like broadband noise (BBN) detected in all CDW materials for $E>E_T$.[5, 6] Indeed, because of this failure of the purely elastic models, researchers have surmised that phase slip must cause BBN.

Recently, substantial theoretical and experimental progress has been made in understanding BBN and its relation to other CDW properties. Bhattacharya *et al.*[7] find that resistive fluctuations explain much of the BBN detected in samples of $TaS_3$ and $NbSe_3$, indicating that BBN arises from local fluctuations of the threshold field. The frequency (f) dependence of the BBN has also come under closer scrutiny. At low f, the BBN noise voltage, $\delta V$, has a $f^{-\alpha}$ dependence[8] where $\alpha \sim 0.35$ and $\delta V$ shows a broad maximum at frequency near the NBN with a rapid rolloff above. This maximum coincides with a minimum in the real part of the

f-dependent conductivity.[9] Bhattacharya *et al.*[8] demonstrate that the BBN spectrum for the sliding CDW is striking correlated with the ac response in the pinned state and suggest that fluctuations in the sliding state are similar to those in the pinned state. Marley *et al.*[10] show that BBN fluctuations persist at frequencies lower than that of an applied ac field, implying that the CDW phase configuration is identical, rather than statistically similar, between states sliding to the left and to the right. Some of these threshold field fluctuations are sensitive to current polarity.

While these experiments significantly increase our understanding of BBN, the microscopic processes which produce BBN remain poorly understood. Maher *et al.*,[11, 12] using samples with different crystal morphologies, find that BBN is sharply reduced in crystals with simple (rectangular) cross section. They suggest that increased BBN occurs in more complicated morphologies because of phase slip which occurs at steps in the crystal thickness.

Several theories have been proposed to explain BBN in CDW materials. Tucker[13] calculates that isoelectronic impurities may pin the CDW strongly (i.e. determine the CDW phase uniquely at the impurity) because of the interaction between the CDW wavevector and the Friedel oscillations of the normal electrons. Thus, for the CDW to slide, there must be a phase slip center (PSC) at each impurity. Thermal fluctuations of the CDW phase on the impurity could cause BBN. Coppersmith[14-16] demonstrates that the purely elastic CDW model must fail for any macroscopic sample. Phase slip must occur in the sample bulk if there exist any variations of $E_T$. However, there are predicted to be few PSC's for samples without charged impurities.[16]

In general, these theories rely on the production of PSC's within the material and assume that fluctuations of the CDW threshold field occur in these regions. An interesting test of the role of PSC's is to measure the BBN while producing PSC's within the sample. The BBN associated with an individual PSC would be apparent as a stepwise increase in the BBN. This chapter describes an experiment[17] in which the BBN is measured in the presence of a temperature gradient. As depicted in Fig. 8-1, the lowest energy CDW velocity, $v_i$, is temperature dependent. Applying a temperature gradient to a moving CDW induces strains. At some critical gradient, it becomes energetically favorable to introduce a PSC, at which discontinuities in $v_i$ may occur. The PSC reduces the elastic strain of the CDW.[18] The temperature gradient allows continuous control of the number of macroscopic PSC's occurring within the sample volume.[19, 20] Since the NBN frequency is roughly proportional to $v_i$, the number of PSC's is determined from the number of NBN peaks. These, thermally-induced, PSC's are different from the phase slip which occurs at impurities or in small regions of the CDW because they are macroscopic objects having dimensions, $\xi_o$xA where $\xi_o$ is the amplitude coherence length and A is the sample cross-sectional area.

We find that thermally-induced PSC's are "soft" and do not generate appreciable BBN. The BBN shows some qualitative characteristics of a thermal average along the sample length, but many features also indicate interaction between the noise sources and the CDW metastable state. The remainder of this chapter is organized as follows: Sect. 8.2 describes the experimental method used to simultaneously measure BBN and NBN in

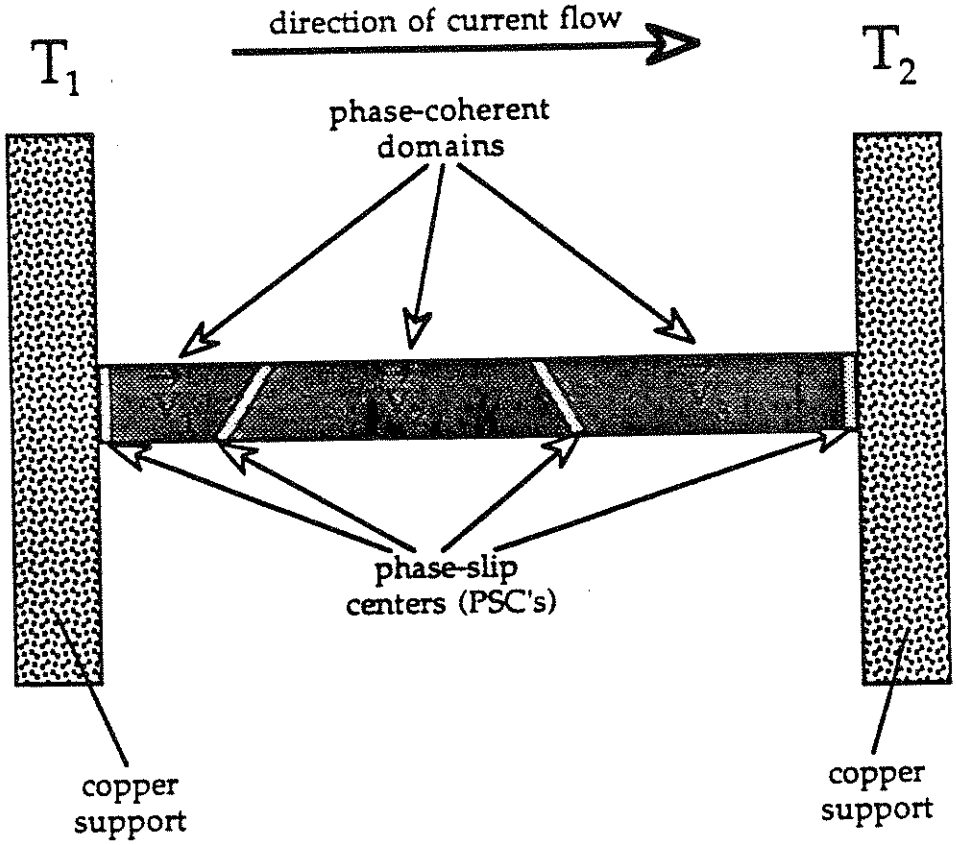


Fig. 8-1. Schematic of phase slip for a CDW material in a temperature gradient. The number of domains depends on the current and the temperature gradient applied across the sample ($T_2$ - $T_1$ ). This sample would show 3 NBN peaks.

small crystals of $NbSe_3$. Our results are presented in Sect. 8.3 and discussed in Sect. 8.4. Our conclusions follow in Sect. 8.5.

## 8.2 Experimental method

$NbSe_3$ crystals are grown from high purity starting compounds in quartz ampoules using vapor transport in a gradient oven. They show room temperature resistance ($R_{RT}$) to low temperature residual resistance ratios of approximately 220, and threshold fields at 48K of ~10mV/cm. In general, $NbSe_3$ crystals grow with stepped faces and variable cross section which cause diffuse NBN spectra.[11, 21] To achieve sharp NBN peaks and to expose clean surfaces for contacts, we delicately cleave the crystal, using the process described below:

(i) glue one end of a $NbSe_3$ crystal (~5-10mm long) on a quartz slide with Ag paint,

(ii) use the back of a scalpel blade to fray the free end of the crystal,

(iii) glue down the frayed end,

(iv) pull one section of the frayed end ~ 30μm away from the rest of the crystal,

(v) by gently moving this sub-crystal, "unzip" it from the rest of the crystal, being careful not to induce deformation in the larger crystal,

(vi) repeat this process until the desired crystal remains,

(vii) cut an appropriate section from the center of this crystal for use in the experiment.

Samples obtained in this way have typical dimensions, 20 $\mu m^2$ x 1 mm, and show clean NBN spectra with 10-20 harmonics of the fundamental peak. The BBN amplitude, $\delta V$, at 4 kHz and 50K is ~ $8nV/\sqrt{Hz}$ for $E=3E_T$, in good agreement with the noise amplitude from other pure $NbSe_3$ crystals with simple geometries.[11] The sample is then rigidly affixed with Ag paint to the temperature gradient apparatus shown schematically in Fig. 8-2a. A variety of methods were used to make contact with the sample (silver paint, gold paint, platinum ink, gold and indium sputtered contacts) The cleanest NBN and BBN spectra are found with Ag paint which, unfortunately, causes substantial contact degradation within several hours at room temperature. The copper supports on which the sample sits are thermally isolated from the underlying Cu probe with balsa wood spacers. The sample is held in a $10^{-5}$ torr He environment, and heaters on each support provide temperature gradients of as much as 20K.

Fig. 8-2b shows the electrical configuration for simultaneous measurement of NBN, BBN, and dc voltage. The sample is current biased in a two probe configuration. Because of the small size of the BBN for these crystals, care must be taken in minimizing crosstalk and additional noise sources. 1:1 buffers in front of each section of the detection circuity substantial reduce crosstalk and ensure that the signals are appropriately impedance matched. We use an HP8558B to detect the NBN peaks and an HP3582A to measure the BBN over a wide spectral range. A Stanford Research SR510 provides accurate noise measurements in a small frequency window (10Hz bandwidth). The temperature of each support is determined relative to a nearby temperature diode with two differential

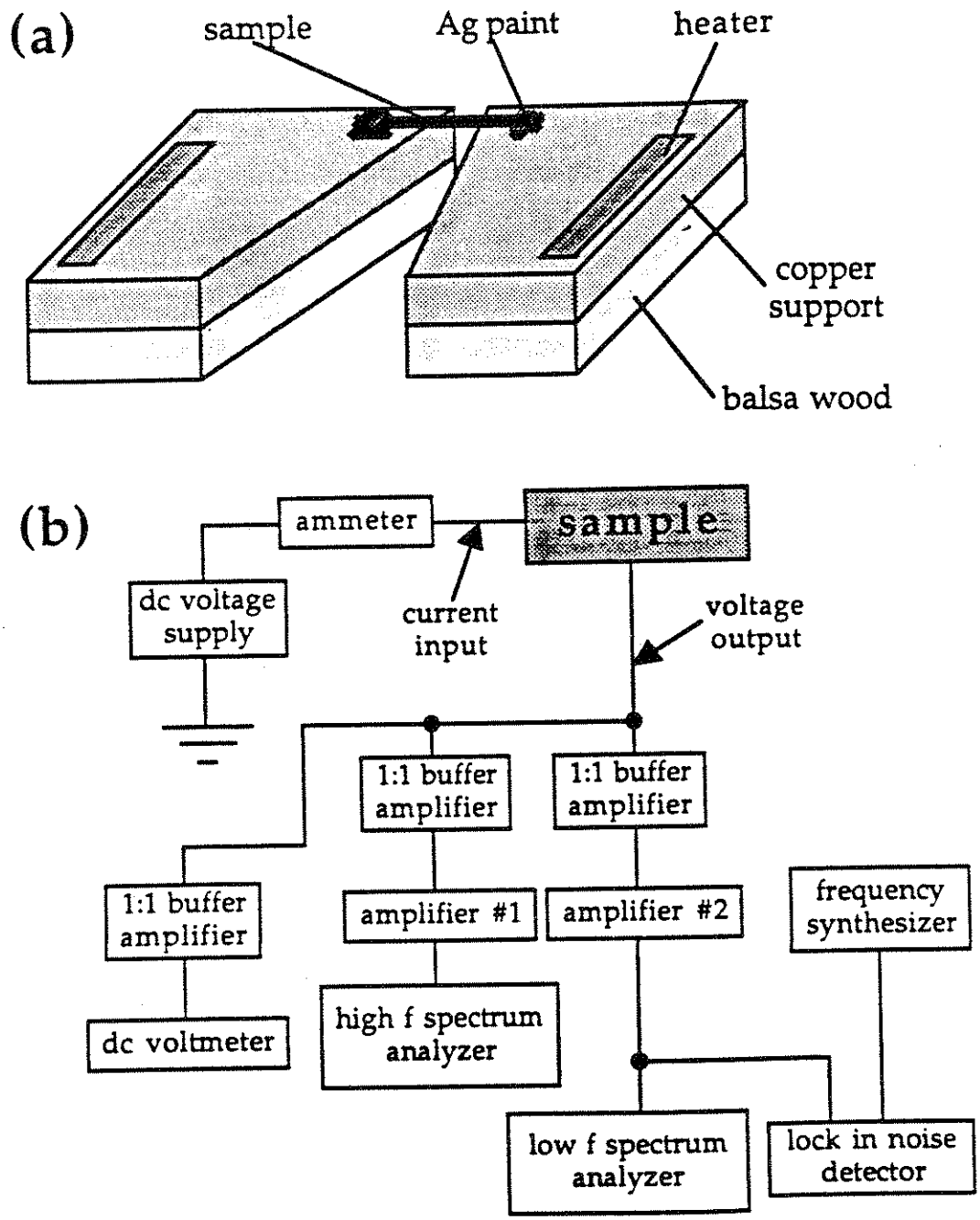


Fig. 8-2. (a) Schematic of temperature gradient apparatus. (b) Electrical schematic for simultaneous measurement of NBN, BBN, and dc voltage. The devices are as follows: dc voltage supply ↔ HP 6114A; ammeter ↔ Keithley 177; 1:1 buffer amplifier ↔ Burr-Brown 3553AM; amplifier #1 ↔ B&H AC3020LN; amplifier #2 ↔ PAR 113; frequency synthesizer ↔ HP 3325B; dc voltmeter ↔ Keithley 177; high f spectrum analyzer ↔ HP 8558B; low f spectrum analyzer ↔ HP3582A; lock in noise detector ↔ Stanford Research SR510.

chromel-alumel thermacouples. An additional thermacouple directly measures the temperature difference between the two supports.

### 8.3 Results

Fig. 8-3 shows the BBN as a function of bias current for six different temperatures. The curves have been offset as an aid to the eye. BBN provides a dramatic signature of the depinning transition, showing a sharp peak at the threshold current ($I_T$) for intermediate temperatures and a more rounded peak at lower T and near the Peierls transition ($T_2$). Though low frequency NBN can cause spurious BBN measurements near $I_T$, these BBN peaks have 1/f-like frequency dependence, and the measurement frequency (4kHz) is significantly removed from the NBN peak (~0.1-1.0 MHz). The temperature dependence of $I_T$ is clearly seen in the BBN peak position. For most samples studied, the initial increase in BBN is followed by decrease and then a slow increase at large I.

Several recent papers[7, 10] have investigated the relationship between BBN and threshold field fluctuations. For $TaS_3$, the region near $I_T$ shows anomalously large BBN, a result which was attributed to interference effects with the NBN. The large BBN peak at $I_T$ for our samples, however, can be directly attributed to $E_T$ fluctuations. As shown in Fig. 8-4a, the CDW transition is coincident with an abrupt drop in sample resistance, $R_S$. In contrast to $TaS_3$, the data for $NbSe_3$ (Fig. 8-4b) shows significant BBN structure with bias field. The noise arising from $E_T$ fluctuations can be directly related to $R_S$ as follows:[7]

$$\delta V = A(T,f)\, I \left| \frac{dR_S}{dE} \right| \qquad (8.1)$$

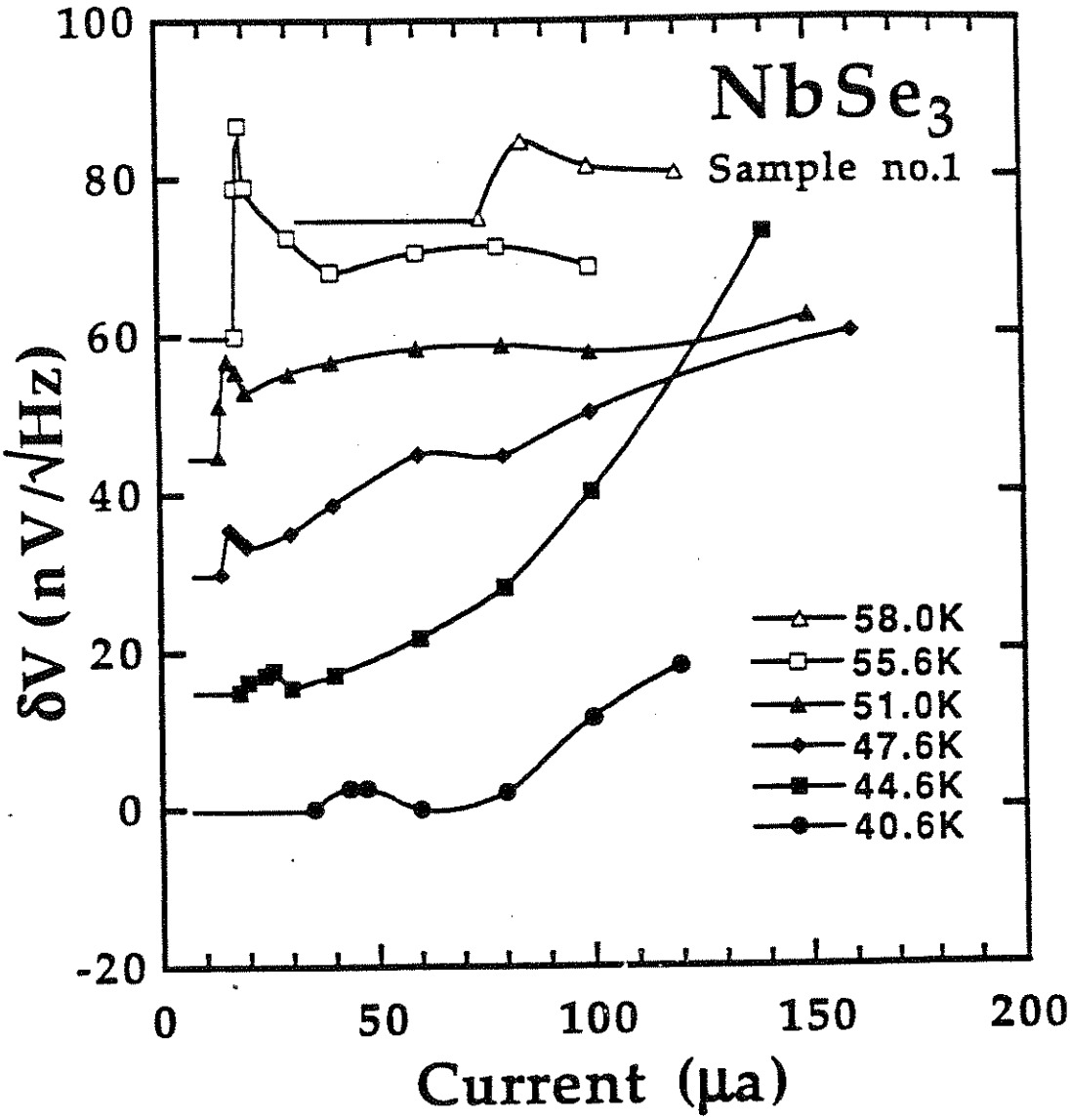


Fig. 8-3. Broadband noise voltage, δV, plotted as a function of bias current for six different temperatures. The curves represent best fits to the data and have been vertically offset as an aid to the eye.

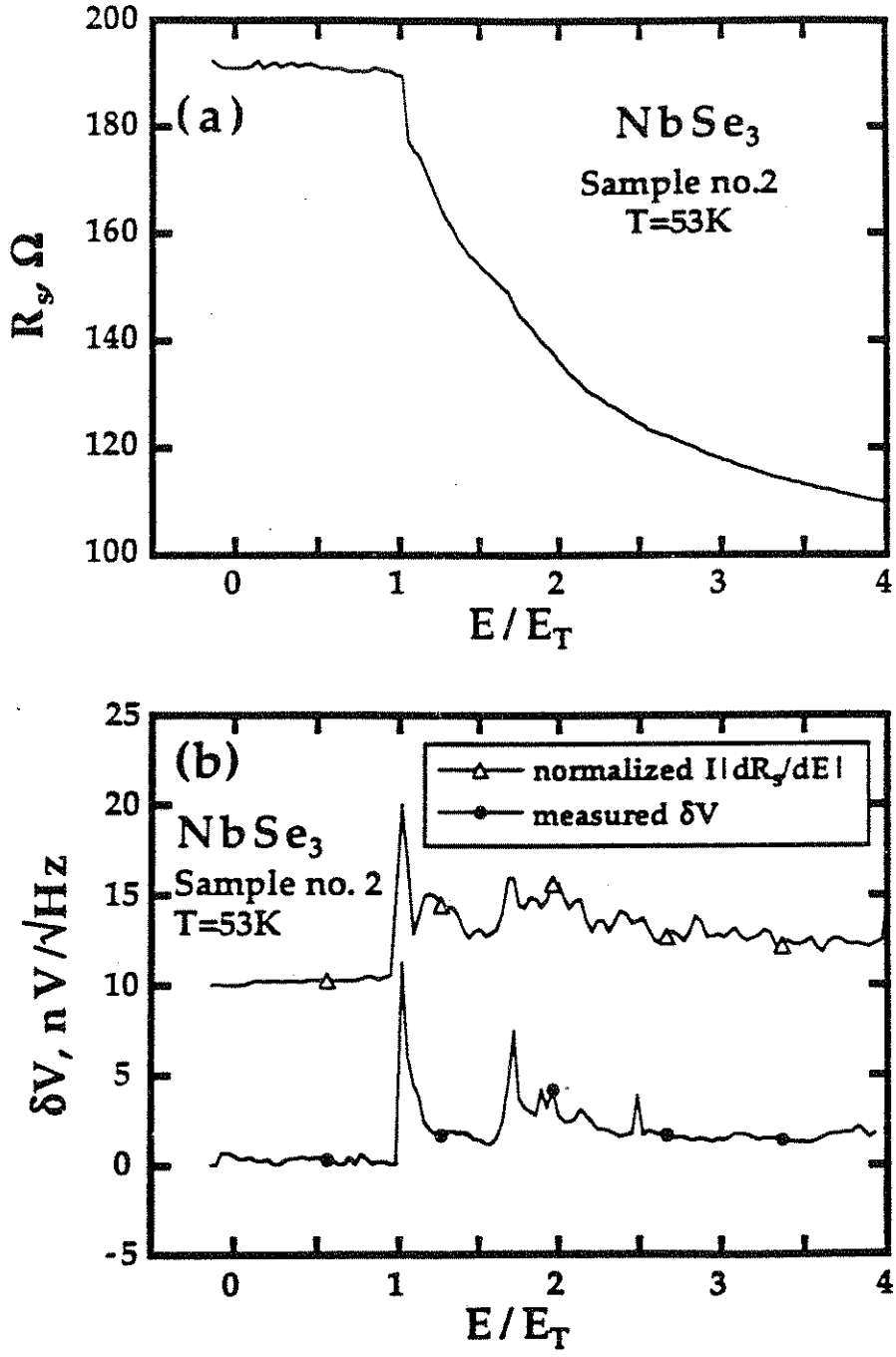


Fig. 8-4. (a) Sample resistance, $R_s$, plotted as a function of reduced bias field, $E/E_T$, for sample no.2. (b) Broadband noise voltage, $\delta V$, and normalized $I|dR_s/dE|$ plotted as functions of reduced bias field for the same sample. $I|dR_s/dE|$ is calculated using the data shown in Fig. 8-4(a) and normalized so the magnitude of the first peak equals that of the measured $\delta V$. The data for $I|dR_s/dE|$ have been vertically offset as an aid to the eye.

where $\delta V$ is the rms noise voltage, and A is a constant which depends only on T and f. Fig. 8-6b plots the measured BBN and $I\,|dR_S/dE|$ calculated from $R_S(E)$ shown in Fig. 8-4a and normalized to match the height of the first BBN peak. Interestingly, not only does equation 8.1 reproduce the sharp BBN peak at $E_T$, it fits many of the secondary peaks as well. At large E, both curves reach similar limiting values. Thus, BBN for $NbSe_3$ seems well explained by models which assume variations of the local $E_T$ or effective pinning force. Phase slip processes, such as those suggested by Coppersmith[14-16] and Tucker,[13] would certainly produce such fluctuations of the threshold field.

To determine the relation the relationship of thermally induced phase slip and BBN, we first characterize the sample at uniform temperature. Fig. 8-5 shows $\delta V$ measured at 4kHz and the position of the NBN fundamental frequency ($f_0$) as functions of temperature for sample no. 1. $\delta V$ and $f_0$ both have maxima near 54K.

As a temperature gradient, $\Delta T$, is applied, the preferred CDW velocity changes along the sample length and phase slips may be induced. Fig. 8-6 depicts the position of $f_0$ and any split off NBN peaks as a function of $\Delta T$. The sign of $\Delta T$ is chosen so that $\Delta T>0 \Rightarrow$ the current flows in the direction of increasing temperature. The temperature of the coldest end of the sample is fixed at 51K. As expected from Fig. 8-5, increasing $\Delta T$ from zero causes $f_0$ to climb and at $\Delta T$=3.1K, the NBN peak splits. In this same region, $\delta V$ first decreases and then begins to increase. No stepwise increase in the BBN occurs when the NBN splits. The additional, thermally-induced, PSC does not produce significant noise. Indeed, the four splittings on the right in Fig. 8-6 appear to be associated with small

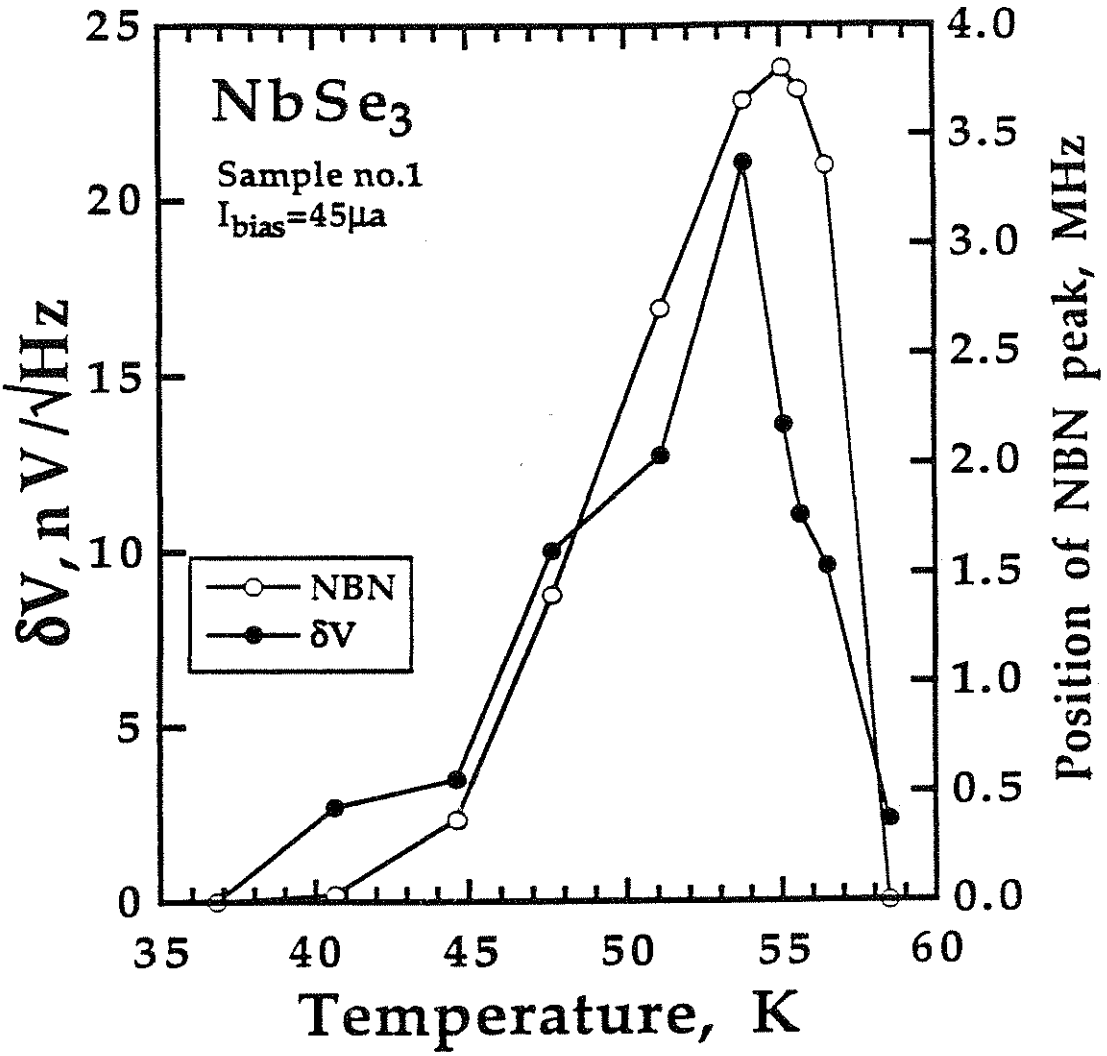


Fig. 8-5. Broadband noise voltage, δV, and narrow band noise peak position plotted as functions of temperature for sample no.1.

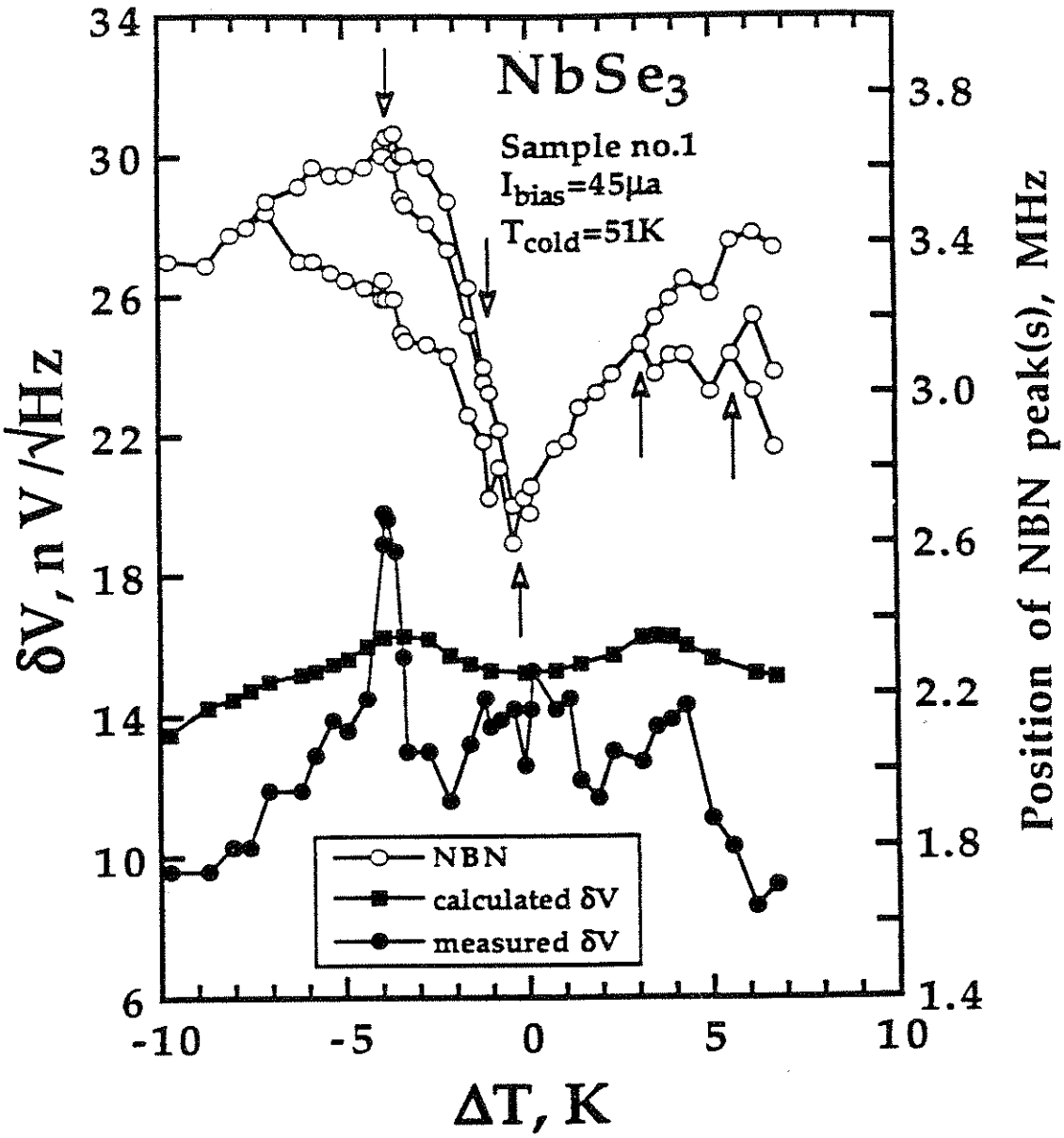


Fig. 8-6. Position of narrow band noise peak position, measured broadband noise voltage, δV, and calculated δV plotted as functions of the temperature difference, ΔT, between the two ends of the sample. The sign of ΔT is chosen such that ΔT>0 implies that current flows in the direction of increasing temperature. Each splitting of the narrow band noise peak is marked by an open arrow and is a signature of PSC formation. We determine the calculated δV by using an average noise per sample length at a particular temperature estimated from Fig. 8-5.

reductions in the noise. However, the splitting at $\Delta T$ = -3.9K occurs with a huge BBN increase. At this splitting, the NBN peaks broaden substantially and considerable fluctuations are evident in the peak position. The BBN increase is presumably caused by fiuctuations of the NBN frequencies as the PSC forms. Similar effects are seen with partial mode locking of the CDW.[22] Numerical studies[23] have shown that substantial BBN can occur at PSC formation because of chaotic behavior of the non-linear system. Previous reports[18] have distinguished two types of NBN splittings, one in which the peaks break apart continuously and one in which a single peak splits into two peaks separated by a finite frequency difference. In the latter case, substantial instability occurs and the NBN peaks broaden due to fluctuations at time scales smaller than the sample time of the spectrum analyzer.

Also plotted in Fig. 8-6 is the $\delta V$ calculated from Fig. 8-5 assuming that BBN arises from a distribution of temperature dependent sources. This thermal average reproduces the BBN maximum at $|\Delta T| \approx 4K$ and the monotonic BBN decrease for $|\Delta T| > 4K$. It does not, however, reproduce the peaks and other structure evident in Fig. 8-6. For $\Delta T < -8K$, the warm end of the sample is above the Peierls transition (59K). The data show no sharp decrease in this range, implying that CDW conversion at the silver paint contacts is not an appreciable noise source.

Fig. 8-7 presents an additional study of the effect of PSC formation on BBN. For this sample, $T_{cold}$ is fixed at 45K. The large number of NBN splittings evident in Fig. 8-7b are expected from the large difference between $f_o(T_{cold})$ and the maximum $f_o$, 2.5MHz. As for sample no.1, no

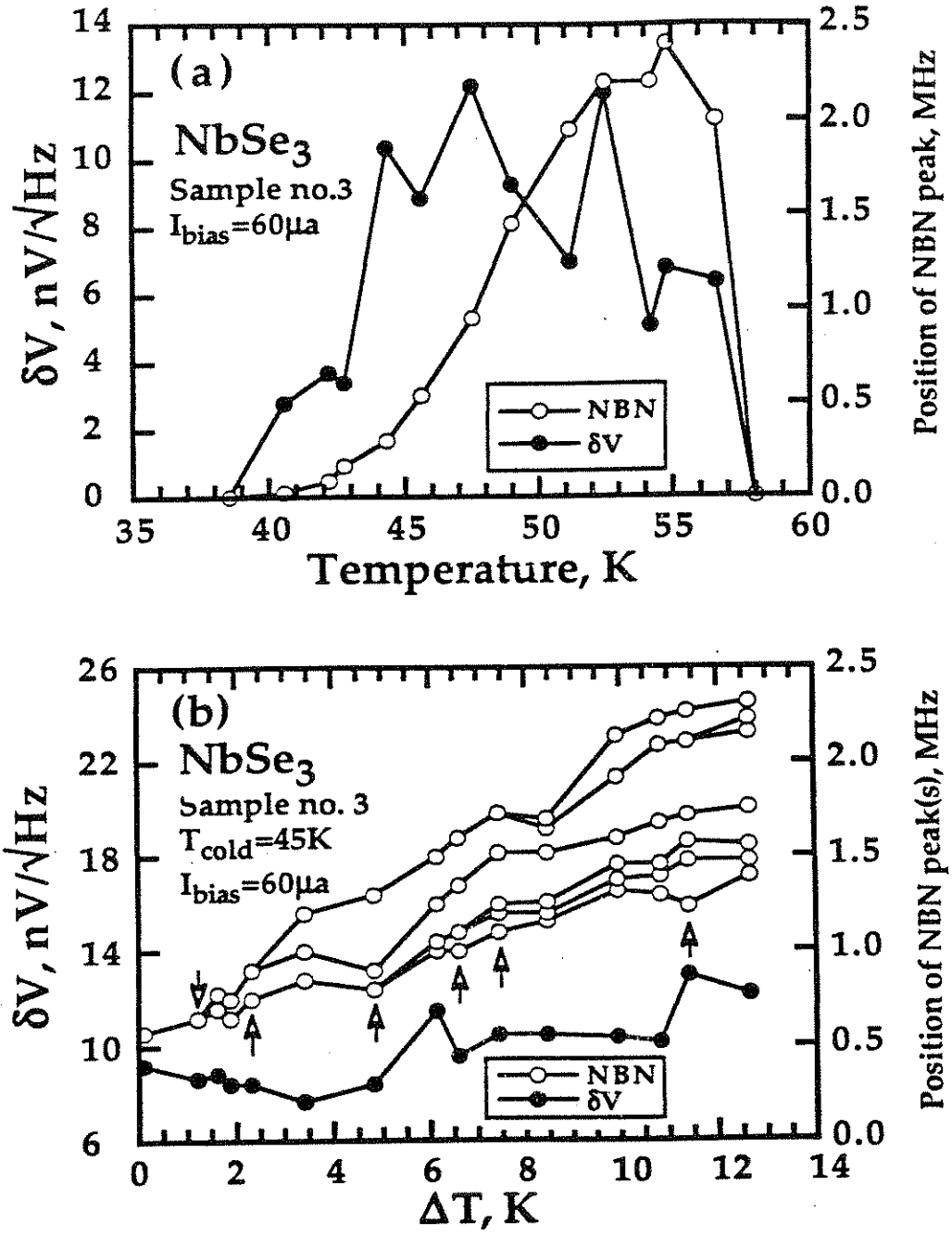


Fig. 8-7. (a) Broadband noise voltage, δV, and narrow band noise peak position plotted as functions of temperature for sample no.3. (b) Position of narrow band noise peak position, and measured broadband noise voltage, δV, plotted as functions of the temperature difference, ΔT, between the two ends of the sample. The sign of ΔT is chosen such that ΔT>0 implies that current flows in the direction of increasing temperature. Each splitting of the narrow band noise peak position is marked by an open arrow and is a signature of PSC formation.

stepwise increase in $\delta V$ occurs as the number of PSC's increases. In fact, for none of the splittings is any BBN signature evident.

The data of Figs. 8-6 and 8-7 suggest that thermally induced phase slip centers do not produce appreciable BBN. Though the $\delta V$ peak on the left of Fig. 8-6 certainly is associated with the formation of a velocity sub-domain, the data is well explained assuming fluctuations of the CDW metastable state that are not endemic to PSC's.[23] We bound, $\delta V_{PSC}$, the noise produced by a macroscopic PSC using the data of Fig. 8-7; $\delta V_{PSC} < 2nV/\sqrt{Hz}$ at 4kHz. The small decrease in $\delta V$ apparent at some splittings may arise from the relaxation of CDW strain in the two neighboring domains.

### 8.4 Discussion

Presently, our understanding of the origin of BBN in CDW materials is limited. Though Bhattacharya *et al.*[7] have demonstrated convincing evidence that threshold field fluctuations cause BBN, the role that phase slip has in producing these fluctuations remains poorly understood. Indeed, it is unclear whether thermal fluctuations[13] or chaotic effects,[23] arising from the strong non-linearity in CDW transport, cause BBN. If BBN is due to phase slip within the sample, it is surprising that the formation of such large scale PSC's does not affect $\delta V$. One possibility is that thermally induced phase slips respond coherently over their volume. Because the effective volume of the induced PSC is much larger than the micro-tears[14] suggested by Coppersmith or the impurity pinned regions[13] suggested by Tucker, thermal fluctuations should be smaller. However, it is unclear how fluctuations of this macroscopic region affect the local

threshold field. In terms of noise from non-linear CDW transport, the effect of a PSC in a one-dimensional model has recently been investigated.[23] No studies have been performed on macroscopic three-dimensional PSC's.

The success of thermal averaging in explaining the qualitative shape of the BBN curve (Fig. 8-6) confirms a distribution of noise sources along the sample length and indicates that there is some independence between these sources. This independence arises naturally from models[13] in which thermal fluctuations at spatially distributed impurities cause local $E_T$ variations. However, the structure and large peaks apparent in Figs. 8-6 and 8-7 indicate that the CDW metastable state also plays an important role. A theory to properly describe BBN in these materials must explain both "thermal averaging" and the role of the CDW metastable state.

### 8.5 Conclusions

We find that thermally-induced PSC's are "soft" and do not produce appreciable BBN. Thermal averaging of noise sources along the sample length reproduces many of the qualitative features of the data, but fails to account for the measured structure. We suggest that this structure arises in part from chaotic noise developed as velocity domains divide and from additional effects of the CDW metastable state. Since recent reports[11] indicate that CDW shear produces substantial BBN, an experiment with a temperature gradient transverse to current flow would further probe the relationship between BBN and PSC's.

References


1. H. Fukuyama and P. A. Lee, Phys. Rev. **B17**, 535 (1978); P. A. Lee and H. Fukuyama, Phys. Rev. **B17**, 542 (1978); P. A. Lee and T. M. Rice, Phys. Rev. **B19**, 3970 (1979).

2. P. Monceau, N. P. Ong, A. M. Portis, A. Meerscaut and J. Rouxel, Phys. Rev. Lett. **37**, 602 (1976).

3. J. W. Brill and W. Roark, Phys. Rev. Lett. **53**, 846 (1984).

4. P. B. Littlewood, Phys. Rev. **B42**, 6694 (1986).

5. R. M. Fleming and C. C. Grimes, Phys. Rev. Lett. **42**, 1423 (1979).

6. Measurements have been performed by another group on one crystal with a spectral Q of 30,000. For this crystal, no broadband noise was detected. See R. E. Thorne, J. S. Hubacek, W. G. Lyons, J. W. Lyding, and J. R. Tucker, Phys. Rev. **B37**, 10055 (1988); R. E. Thorne *et al., ibid.* **B35**, 6348; **B35**, 6360 (1987).

7. S. Bhattacharya, J. P. Stokes, Mark O. Robbins and R. A. Klemm, Phys. Rev. Lett. **54**, 2453 (1985).

8. S. Bhattacharya, J. P. Stokes, M. J. Higgins and M. O. Robbins, Phys. Rev. **B40**, 5826 (1989).

9. S. Bhattacharya, J. P. Stokes, M. J. Higgins and Mark O. Robbins, Phys. Rev. **B43**, 1385 (1991).

10. A. C. Marley, M. B. Weissman, R. L. Jacobsen and George Mozurkewich, Phys. Rev. Lett. **44**, 8353 (1991).

11. M. P. Maher, T. L. Adelman, J. McCarten, D. A. DiCarlo and R. E. Thorne, Phys. Rev. **B43**, 9968 (1991).

12. J. R. Tucker, Phys. Rev. Lett. **65**, 270 (1990); J. C. Gill, Phys. Rev. Lett. **65**, 271 (1990); R. E. Thorne and J. McCarten, Phys. Rev. Lett. **65**, 272 (1990).

13. J. R. Tucker, Phys. Rev. **B40**, 5447 (1989).

14. S. N. Coppersmith, Phys. Rev. Lett. **65**, 1044 (1990).

15. S. N. Coppersmith and A. J. Millis, Phys. Rev. **B44**, 7799 (1991).

16. S. N. Coppersmith, Phys. Rev. **B44**, 2887 (1991).

17. S. Hoen and A. Zettl, presented at the *American Physical Society March Meeting* (Cincinatti, 1991).

18. P. Parilla, Ph.D. Thesis, University of California, Berkeley (1989).

19. N. P. Ong, G. Verma and K. Maki, Phys. Rev. Lett. **52**, 663 (1984); G. Verma and N. P. Ong, Phys. Rev. **B30**, 2928 (1984); X. J. Zhang and N. P. Ong, Phys. Rev. **B30**, 7343 (1984).

20. S. E. Brown, A. Janossy and G. Grüner, Phys. Rev. **B31**, 6869 (1985); M. F. Hundley and A. Zettl, Phys. Rev. **B33**, 2883 (1986); R. P. Hall,M. F. Hundley and A. Zettl, Phys. Rev. **B38**, 13002 (1988).

21. R. E. Thorne, Phys. Rev. **B45**, 5804 (1992).

22. S. Bhattacharya, J. P. Stokes, M. J. Higgins and R. A. Klemm, Phys. Rev. Lett. **59**, 1849 (1987).

23. D. Jelcic and A. Bjelis, Phys. Rev. **B43**, 1735 (1991).